INFORMATION TO USERS

This manuscript has been reproduced from the microfilm master. UMI films the text directly from the original or copy submitted. Thus, some thesis and dissertation copies are in typewriter face, while others may be from any type of computer printer.

The quality of this reproduction is dependent upon the quality of the copy submitted. Broken or indistinct print, colored or poor quality illustrations and photographs, print bleedthrough, substandard margins, and improper alignment can adversely affect reproduction.

In the unlikely event that the author did not send UMI a complete manuscript and there are missing pages, these will be noted. Also, if unauthorized copyright material had to be removed, a note will indicate the deletion.

Oversize materials (e.g., maps, drawings, charts) are reproduced by sectioning the original, beginning at the upper left-hand corner and continuing from left to right in equal sections with small overlaps. Each original is also photographed in one exposure and is included in reduced form at the back of the book.

Photographs included in the original manuscript have been reproduced xerographically in this copy. Higher quality 6" x 9" black and white photographic prints are available for any photographs or illustrations appearing in this copy for an additional charge. Contact UMI directly to order.

UMI

A Bell & Howell Information Company
300 North Zeeb Road, Ann Arbor MI 48106-1346 USA
313/761-4700 800/521-0600

ESTIMATION OF FRICTION VELOCITY AND DIRECTION AT THE OCEAN SURFACE FROM PHYSICAL MODELS AND SPACE-BORNE RADAR SCATTEROMETER MEASUREMENTS

by

Ellen Elisabeth Lettvin

A dissertation submitted in partial fulfillment
of the requirements for the degree of
Doctor of Philosophy
(Electrical Engineering and
Atmospheric, Oceanic and Space Sciences)
in The University of Michigan
1998

Doctoral Committee:

Professor John F. Vesecky, chair
Professor Owen M. Phillips
Dr. David R. Lyzenga
Professor Fawwaz T. Ulaby
Associate Professor Guy A. Meadows

To Peter, Alexander, Joan, Theodore and Irene.

ACKNOWLEDGMENTS

Many people have helped me to do this work. It would be impossible to name them all. Some individuals, however, have helped me immensely. Professor John Vesecky was a helpful and supportive advisor. Professor Owen Phillips was kind enough both to host me as a visiting student at the Johns Hopkins University for three years, and also to provide me with valuable advice throughout that time. In addition, Dr. David Lyzenga was a consistent source of advice in many areas relevant to my research. Professor Jong-Shi Pang at the Johns Hopkins University also took time on several occasions to help me with some of the important problems regarding the optimization work. Many of my Professors and colleagues at the University of Michigan and at the Johns Hopkins provided me with day-to-day advice and help with all the pitfalls of trying to do research.

I would like to thank the Office of Naval Research for funding me throughout my time in graduate school. Carl Nelson and colleagues at APL-JHU were kind enough to let me use their wave spar buoy measurements, and Will Drennan, Mark Donelan and Hans Graber at the University of Miami also also made their wave measurements available to me to use in this research. Finally, Mike Freilich and the JPL PO-DAAC made the ERS-1 scatterometer available to me for use.

TABLE OF CONTENTS

LIST OF FIGURES

LIST OF TABLES

CHAPTER I: INTRODUCTION

The wind at the surface of the earth is one of nature's forces with which we are most immediately familiar. The winds are driven by unequal heating of the earth's atmosphere by the sun, the resulting density and pressure gradients and by the rotation of the earth. Measurement stations are present to varying extent across all continents, providing characterization of the wind field over land. Over the oceans, however, at relatively short distances away from land, comparatively little is known about the wind field. Historically, measurements of the near-surface winds over the oceans have been available only from buoys or ships, so coverage has been limited to coastlines and along shipping routes. Knowledge of the winds at the ocean surface impacts such diverse areas as routing of ships and sailing; weather forecasting; global climate modeling; and modeling and forecasting of ocean waves, where the wind constitutes both the greatest source of model uncertainty as well as the most important model input. Recently, with the advent of satellite-borne remote sensing, great progress has been made towards using microwave measurements as a basis for inferring the wind speed and direction on the open ocean.

Within the last decade several satellites that serve in this capacity have been launched, such as, the European Remote Sensing Satellite (ERS-1 and-2) operated by the European Space Agency (ESA), and NSCAT, a NASA-built radar scatterometer that was flown for a few months in 1997 on the Japanese ADEOS platform. Using measurements obtained by these systems it is now possible to obtain daily wind field maps and forecasts over many parts of the world's oceans. An example of such data that are readily available over the Internet is provided in Figure 1.1. The NSCAT instrument acquired the data presented in this figure over the Pacific Ocean on September 21, 1996. In this figure, the

background color indicates the wind speed and the white arrows show the wind direction. Major features, such as the Trade Winds and the Inter-Tropical Convergence Zone can be resolved, as well as the presence of two typhoons in the western Pacific. This image was taken from the Internet web site: http://winds.jpl.nasa.gov/nscat_data/index.html. These maps of the wind field at the ocean surface constitute a great improvement over the previous lack of data on the open ocean, but there are many conditions under which these wind estimates differ significantly from the true winds. One of the main reasons for these wind field estimation errors is that radar measurements of the ocean surface provide only an *indirect* means for inferring the oceanic wind vector. Ocean surface winds roughen the surface and radar backscatter is largely governed by this roughness. Thus, ocean surface roughness is the link between the surface winds and the radar echoes.

A scatterometer is an active microwave measurement device which transmits radar waves at a given 'target', such as the earth, and then measures the energy scattered back towards the transmitter, or backscatter. The radar backscatter characterizes the surface roughness at a particular scale in the area of the radar 'footprint' on the ocean. Backscatter is a function of radar system characteristics such as frequency and polarization, of surface properties, such as roughness and dielectric constant, and also of the measurement geometry. Figure 1.2 provides an example of a typical scatterometer measurement scenario and illustrates some of the important geometrical quantities: the measurement altitude is denoted by h; the angle between the vertical and the radar viewing angle, known as the incidence angle, is denoted by θ_{IA}; the angle between a reference direction, such as North, and the direction towards which the antenna is pointing is known as the look angle, and is denoted ϕ_{LOOK}. The relative angle between the wind direction and the look direction is known as the azimuth angle.

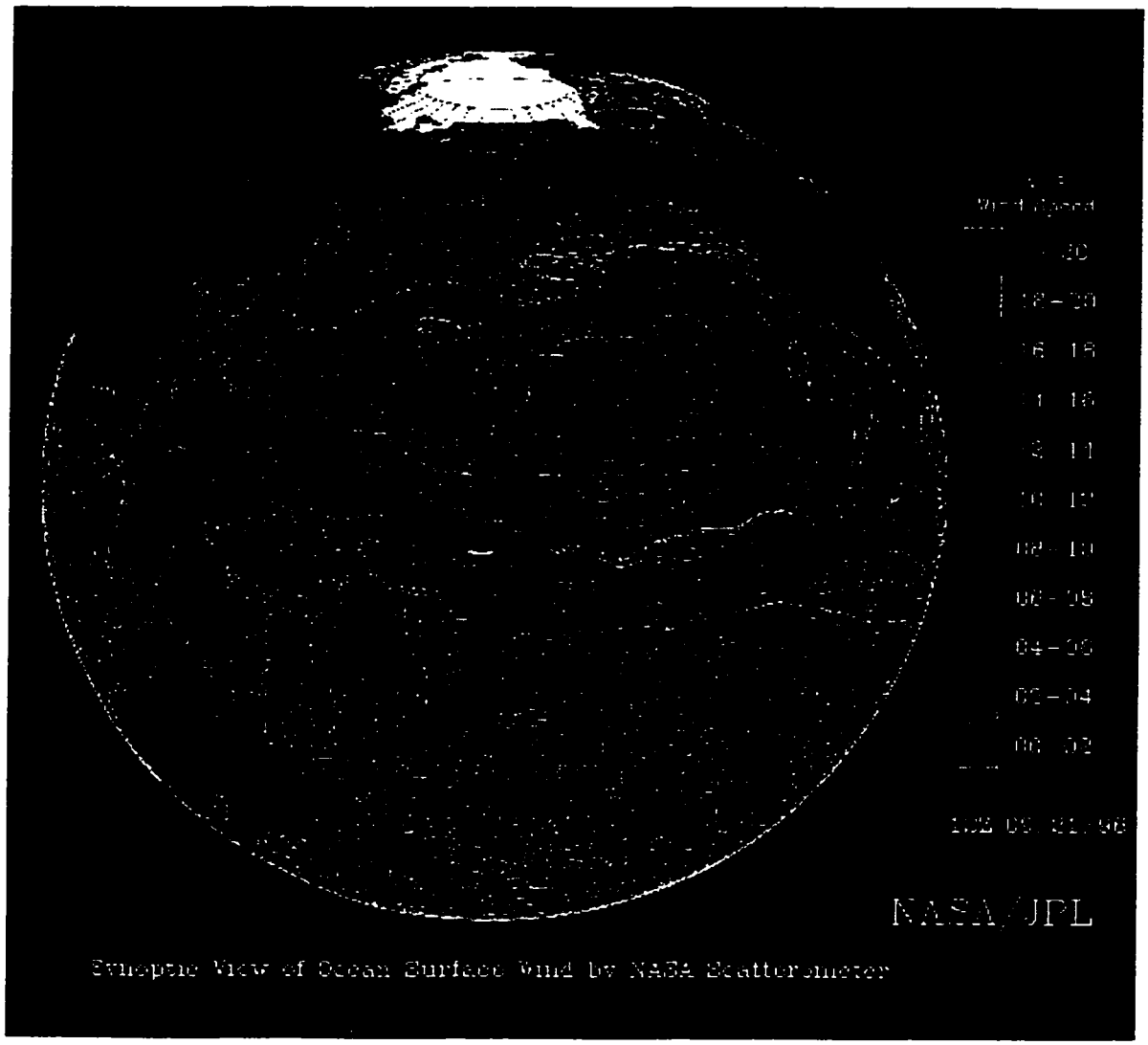

Figure 1.1: Synoptic View of Ocean Surface Wind Derived from Measurements obtained by the NASA NSCAT Scatterometer.

The idea that radar measurements could be used to study the ocean surface originated several decades ago with military studies of so-called 'sea clutter'. These preliminary studies spurred several research efforts, notably Moore and Pierson (1967), who investigated radar scattering from the sea surface as a function of environmental conditions, particularly forcing from the winds at the ocean surface. Evidence that radar

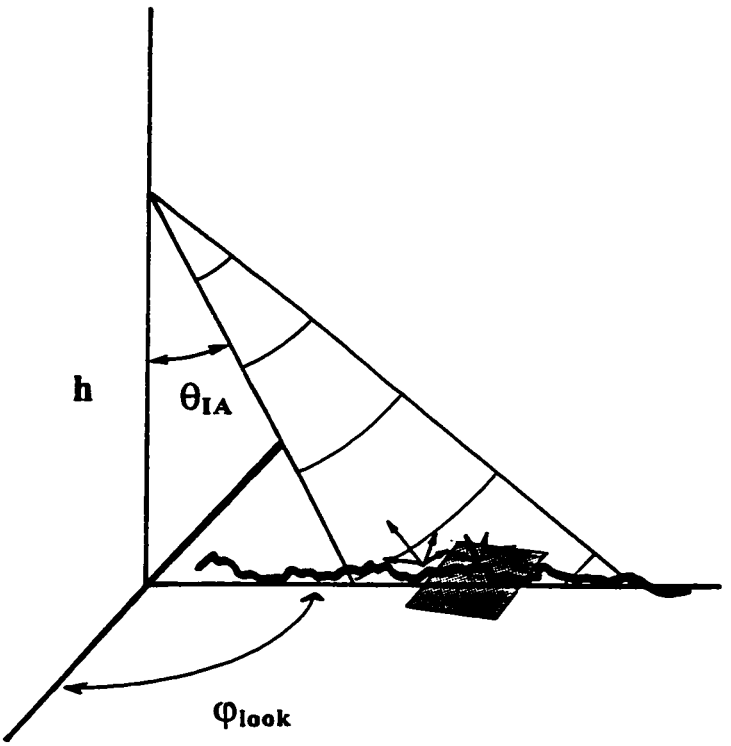

Figure 1.2: Typical Scatterometer Measurement Scenario Illustrating Primary Geometric Quantities

measurements could serve as the basis for inferring the wind field at the ocean surface led to acquisition of the first space-borne radar measurements of the sea from Skylab in the early 1970s, and the subsequent deployment of the Seasat satellite in 1978. Seasat was equipped with a suite of sensors, one of which was designed specifically for measuring the winds at the ocean surface. Although Seasat was functional for less than four months, it obtained data of significant importance to several areas of meteorological and oceanographic research. The data obtained during the Seasat mission were the focus of over a decade of analysis efforts and served as the impetus to subsequent radar remote measurement programs.

Under most conditions encountered in satellite-based scatterometry, a primary mechanism responsible for the observed backscatter is the so-called Bragg scattering,

which occurs when there is a resonance between the electromagnetic and the ocean waves. This resonance condition is generally met by ocean waves of wavelengths on the order of less than one meter, depending on the radar wavelength and incidence angle. The ocean waves that act as Bragg scatterers respond nearly instantaneously to the wind; they are the roughness elements whose alignment relative to the wind direction, and whose density serve as the linkage between the wind stress imposed on the ocean surface and the observed backscattering cross-section. Using a single scatterometer measurement, it is possible to obtain an estimate of the wind stress or the wind speed.

In order to infer the direction of the wind or the wind stress, however, it is necessary to consider the directional dependence of backscatter. For a given wind speed, radar backscatter varies as a function of azimuth angle, as illustrated in Figure 1.3. As shown in this plot, the radar backscatter achieves its maxima when the wind and the radar look are aligned and its minima when the radar look direction and the wind are orthogonal. The upwind direction (ϕ_{az}=0°) has slightly stronger backscatter than the downwind direction (ϕ_{az}=180°). In principle, given two backscatter measurements for the same area of the sea, viewed from orthogonal directions, it is possible to deduce the wind direction. Scatterometer systems are equipped with multiple beams to exploit this azimuthal dependence of backscatter.

For instance, the Seasat scatterometer was equipped with two pairs of orthogonally-looking beams directed at each side of the satellite track. Only one pair of beams was operational at a given time. The NSCAT scatterometer employed a similar beam configuration, but both pairs of beams operated simultaneously. The ERS-1 and ERS-2 systems (AMI) employ three beams looking to one side of the satellite; the fore and mid beams are separated by 45°; the fore and aft beams are separated by 90°. The ERS beam configuration results in the collection of three near-simultaneous snap-shots of the ocean surface, two of which are orthogonal. Figure 1.4 provides an illustration of the ERS-1

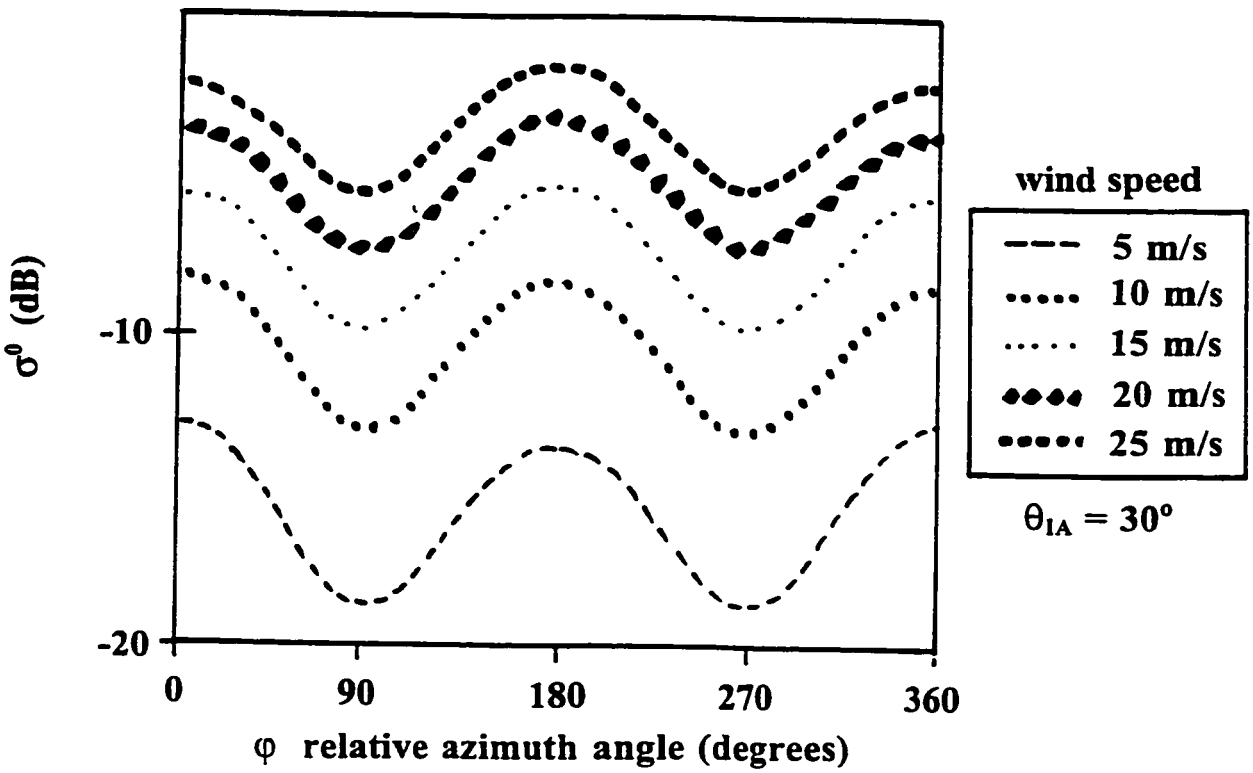

Figure 1.3: Illustration of the Variability of Radar Backscatter with Wind Speed and Azimuth Angle. Figure derived from Seasat model function, SASS, Robinson (1985)

system indicating the positions of the three beams as well as the satellite altitude, swath size and resolution.

The relationship between radar backscatter and ocean surface winds includes several complicated physical interactions that are quite difficult to model, such as the response of the ocean surface to forcing by the wind and the interaction between the electromagnetic and the ocean waves. Models of these physical phenomena tend to have many sources of uncertainty and are typically associated with great computational requirements. As a result, operational wind retrieval efforts have been primarily empirical, depending on a series of experiments that were conducted under a limited range of environmental circumstances.

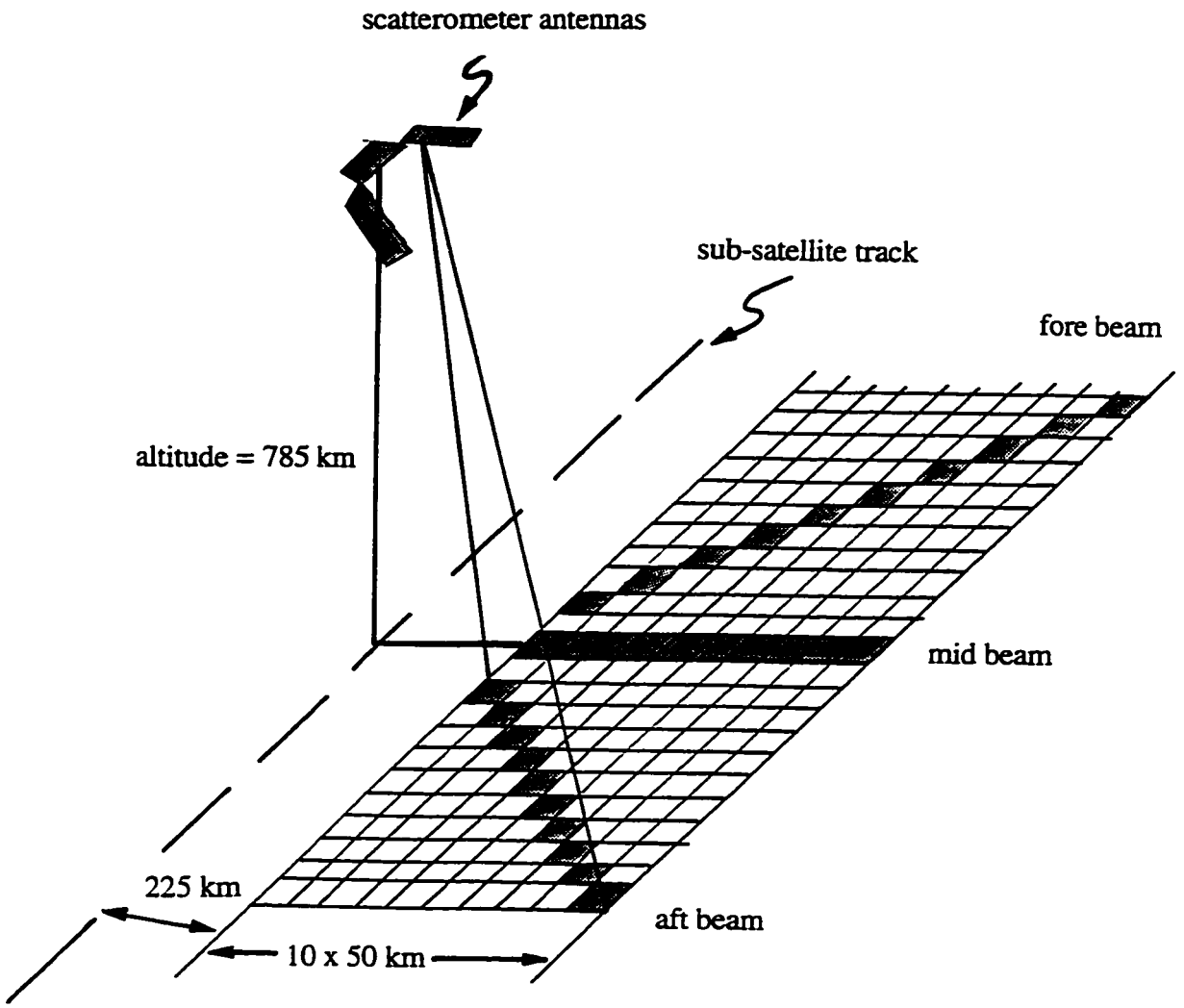

Figure 1.4: Description of the ERS-1 System Geometry and Primary Parameters.

An empirical model function relating the Seasat scatterometer measurements to the radar collection parameters (antenna polarization and frequency, incidence and azimuth angle) and the wind speed and direction at the ocean surface was known as the SASS model function. The SASS model function established a relationship between the model parameters and the observations, which is often referred to as a forward model. In many problems in remote sensing, a forward model is developed from data sets collected in extensive field campaigns. Subsequent, operational applications require inversion of the forward model to obtain predictions of the underlying physical conditions that gave rise to the observations. In the case of the SASS model function, data from the Gulf of Alaska (GOASEX) and the Joint Air-Sea Interaction (JASIN) experiments were used to develop the model function.

The model currently used to retrieve the wind field from ERS-1 or ERS-2 scatterometer data is known as CMOD-4. This model was developed at the European Center for Medium Range Weather Forecasting (ECMWF), based on data acquired during several pre-launch field campaigns (Stoffelen and Anderson, 1993). CMOD-4 is a power law model that relates radar cross section to the wind speed and direction at 10 m above the ocean surface in a neutrally stratified boundary layer. Under a broad range of conditions, this model provides reasonably accurate wind retrievals (see, for example Graber et al., 1996). However, CMOD-4 is basically a 'curve fit' obtained from a suite of measurements, and as such, it does not help us to gain a better understanding of the underlying physical processes that gave rise to the measurements.

Freilich and Dunbar (1993) developed another empirical model that has also been used for ERS-1 wind retrieval. This retrieval method makes use of surface wind predictions obtained by operational Numerical Weather Prediction (NWP) forecasts. These forecasts have been interpolated so that they are co-located with the ERS-1 measurement cells. As with CMOD-4, this model has enjoyed acceptable performance under many environmental conditions (Graber et al., 1996), but as it makes use of NWP winds in its

retrieval process, any weaknesses or errors in the NWP winds will be reflected in the resulting retrievals.

For both CMOD-4 and the SASS model function, the forward model expressed radar backscatter from the ocean surface, normalized by area, as a power law function of wind speed modulated by a cosinusoidal dependence on wind direction. The exact form of the model required many empirically derived coefficients specified in lengthy look-up tables, which were of limited physical significance. For more details regarding the SASS model function, the reader is referred to Bracalente et al. (1980). The forward model used for the Seasat wind retrievals was seriously flawed (Woiceshyn et al. (1986), Pierson (1990)). For example, this model function did not include a dependence on any parameters describing the sea surface or the air-sea interface, such as temperature, viscosity, surface tension, sea state, or the atmospheric boundary layer stratification. It is recognized by many authors, such as Plant (1986), that many of these environmental factors do modify the radar return from the ocean surface; it is also believed that a power law model, such as the SASS model function and CMOD-4, provides an inadequate representation for the forward model.

The wind retrieval approach taken by the SASS model function and CMOD-4 assumed that the primary relationship of interest was that between the wind vector and radar backscatter. This approach was taken because wind speed measurements of reasonable accuracy were readily available for model verification at buoy or ship locations and direct measurements of wind stress were difficult to obtain. It is widely recognized, by authors such as Pierson (1990), however, that friction velocity rather than wind speed is more closely coupled to surface roughness.

Wind stress is generally characterized using the notation

$$\tau = \rho C_D |U| U, \tag{1.1}$$

where ρ is the air density, C_D is the drag coefficient and U is the wind, assumed to be measured at 10 m above the ocean surface. Often, the wind stress is expressed in terms of the friction velocity, u*, which is defined as $u^*=(\tau/\rho)^{1/2}$. Friction velocity is used to characterize the stress imposed on the ocean surface by a wind of a given magnitude. Unlike wind speed, friction velocity varies as a function of several environmental parameters, which govern momentum transfer from the wind into the ocean surface, such as atmospheric stability and sea state. In the wind retrieval scheme implemented in this research effort, we seek to estimate friction velocity and direction, not wind speed and direction at the ocean surface. Given a measurement of u*, the wind velocity at a particular height above the ocean surface can be estimated using a boundary layer model. Two popular boundary layer models are due to Paulson (1970) and Dyer (1974).

A suite of backscatter measurements associated with a patch of ocean surface must be inverted to yield an estimate of the wind (or stress) field presumed to have given rise to the observations. Typically, this requires minimizing an error metric between the backscatter observations and the model predictions of radar backscatter, which vary as a function of wind speed and direction as well as other environmental parameters. Due to the sinusoidal dependence in the model function and to various noise contributions, such as described in Chi and Li (1988), this inversion process is not straightforward. Typically, several possible combinations of wind speed and direction could have given rise to a given backscatter observation. Multiple observations of a given patch of ocean are usually obtained to help resolve this ambiguity.

In the mid-to late 1980s several innovative studies were made of the radar response of the ocean surface. These efforts consisted of two primary components: a model for predicting the waves at the ocean surface for a given wind speed, and a model for predicting the electromagnetic energy scattered from that realization of the sea surface, for a particular radar system configuration. The best known of these were Donelan and Pierson

(1987), Durden and Vesecky (1986) and Plant (1986). The primary differences between these three models were in the choice of ocean spectral model and how the modulation of the short waves by the underlying long waves was modeled. Within the past few years, Apel (1994) proposed a similar approach to radar cross section prediction that made use of the recently developed spectral models of Banner (1990) and Klinke and Jahne (1992). Within the last year, two additional research efforts along these same lines have been presented: Romeiser et al. (1997), which describes a modified form for the composite scattering model, and Janssen et al. (1998), which describes a new ocean spectral model. We will discuss these recent contributions in later sections.

It should be noted that in addition to using radar scatterometry as the basis for obtaining estimates of the oceanic wind field, a considerable amount of work has been devoted to obtaining estimates of the wind field at the ocean surface from microwave radiometer measurements. This approach is believed to be quite promising. Notably, Busalacchi et al. (1993), Wentz (1991), Wentz and Mattox (1986) and Wilheit and Fowler (1977) have demonstrated that microwave radiometry can serve as a viable basis for obtaining accurate predictions of the wind speed and direction at the ocean surface. A future extension of some of the work pursued in this thesis could be to apply the ocean wave model developed here, in conjunction with an appropriate model for microwave emissions from the ocean surface, to obtain wind retrievals from passive microwave measurements.

The primary goal of this research was to develop a technique for retrieving the friction velocity and direction at the ocean surface that combined radar scatterometer measurements with a physically-based ocean spectral model and a physically-based electromagnetic scattering model. We hoped that such an approach, in addition to producing viable wind field predictions, would also yield additional physical insight about some of the processes taking place at the air-sea interface, that influence the observed radar signature. In particular, we hoped to gain a better understanding of the ocean surface and

its response to the wind at scales in the vicinity ERS-1 Bragg scatterers, namely, for ocean waves of wavelengths between 3 and 9 cm.

As a step towards this objective we have developed the friction velocity retrieval scheme depicted in Figure 1.5, which we will briefly summarize here. For a particular region of the ocean where ERS-1 measurements are available, we will specify a set of hypothetical wind stresses. Typically, these hypothetical stresses will span a broad range of allowable values for u* as well as all possible directions. Associated with each of these candidate forcings will be a realization of the ocean wave number spectrum, describing the distribution of roughness elements on the ocean surface for the region in question. For a set of radar viewing parameters, the electromagnetic scattering code will obtain a radar backscatter prediction for each of these spectra. Therefore, for each resolution cell in a given region, there will be a set of backscatter predictions obtained from the models, as well as one backscatter measurement. An error metric or cost function combines these backscatter predictions with the ERS-1 measurements. A procedure seeking the minimal discrepancy between the measurements and the predictions serves as the basis for identifying the presumed forcing for each resolution cell. Finally, we verify the accuracy of these retrievals of the wind stress using National Data Buoy Center (NDBC) measurements that are co-located with the ERS-1 resolution cells.

A description of the spectral model used to characterize the ocean surface is presented in Chapter 2. This model is comprised of two components: in situ measurements of the directional wave spectrum and the equilibrium spectral model of Phillips (1985). Particular focus is given to the function used to describe the directional spreading of the ocean waves relative to the wind direction. The model used to characterize the electromagnetic scattering at microwave frequencies for a given realization of the ocean surface is provided in Chapter 3. In addition, we present an example wherein we obtain radar cross section predictions using this particular choice of ocean spectrum and scattering model. We also investigate the impact of long waves on radar scattering in this section.

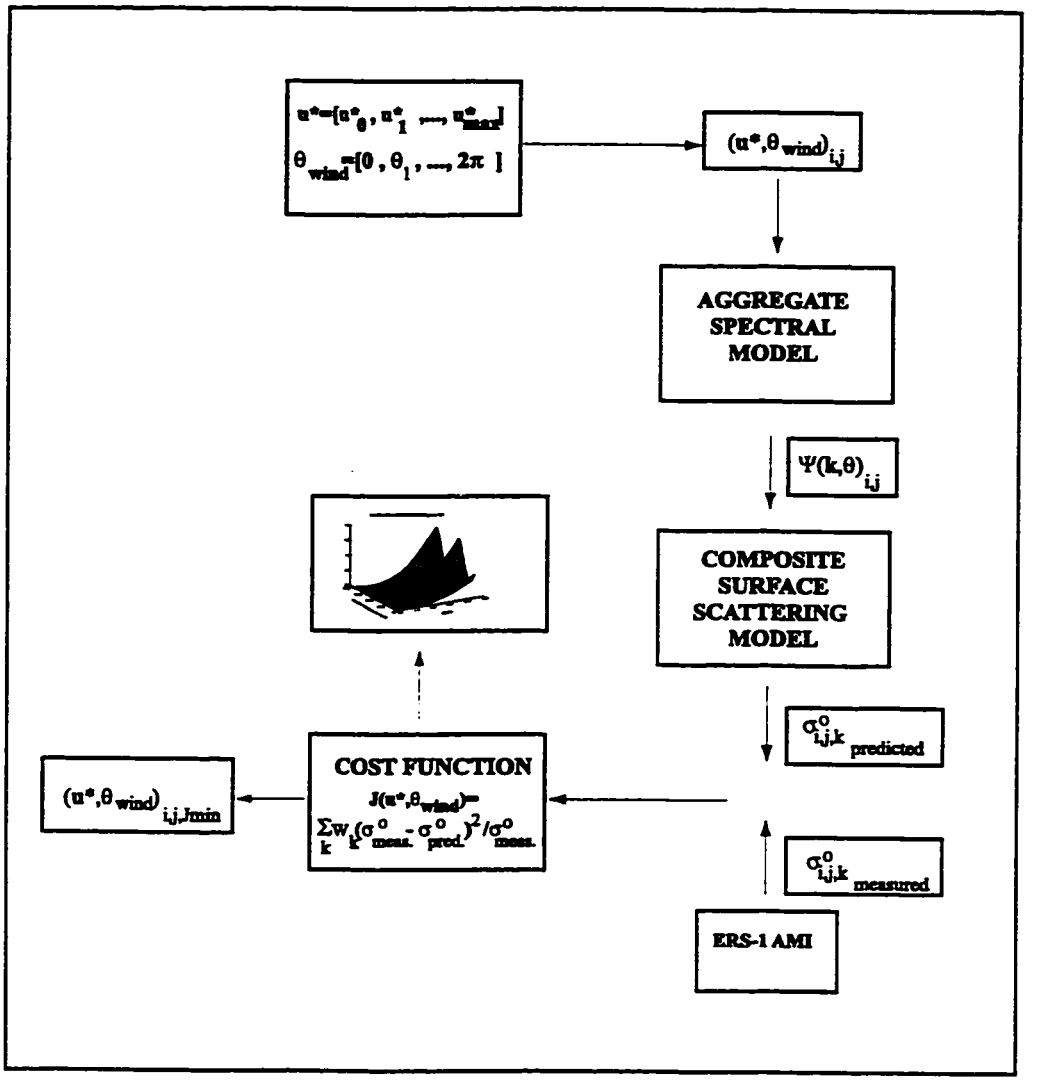

Figure 1.5: Overview of the friction velocity retrieval scheme implemented in this effort. A matrix of model inputs, u* and θ_{wind}, are indicated at the top of the diagram. An ocean wave number spectrum, indicated by $\Psi(k,\theta_{wind})$, is associated with each model input. For each set of ERS-1 viewing geometry parameters (incidence and azimuth angles) and each ocean wave number spectrum there is a prediction of the normalized radar cross section, $\sigma^0_{predict}$. For each prediction, there is a backscatter measurement obtained by the ERS-1 system, $\sigma^0_{meas.}$. These two quantities are combined in a cost function, $J(u^*,\theta_{wind})$, which is minimized. The cost function minimum is compared with spatially and temporally coincident measurements of the friction velocity and direction obtained by a NDBC buoy.

The basis for how the model results and the scatterometer measurements are combined is described in Chapter 4, which provides an overview of cost functions in general, as well as a discussion of the particular cost functions that we employed in this effort. In addition, we examine the impact of varying the spectral model parameters on the resultant friction velocity retrievals. Finally, we compare our friction velocity retrievals based on this technique with in situ measurements. The conclusions we have drawn from this work and areas for future research are discussed in Chapter 5.

CHAPTER 2: AGGREGATE SPECTRAL MODEL

2.1 INTRODUCTION

The retrieval of wind stress estimates from scatterometer data that is implemented in this research requires three components as depicted in Figure 1.5: a description of the ocean surface attributable to a given forcing by the wind, a means for predicting the radar backscatter from that surface and a framework for combining these predictions with backscatter observations. This chapter's focus will be on the first of these three components: the two-dimensional ocean wave number spectral model used to characterize the distribution of roughness elements at the ocean surface that are observed by the radar. We will start this chapter with a brief discussion of wind stress or friction velocity, as it is the primary input to our spectral model, as well as the quantity that we seek to retrieve from scatterometer measurements.

In Chapter 1 we mentioned that friction velocity is the geophysical parameter most closely related to scatterometer measurements of the sea surface. It is therefore worthwhile to provide a closer look at this measure of wind stress and its relationship to wind speed. Geernaert (1988) is an excellent reference on this topic and was very helpful in the preparation of this section.

The geostrophic balance between the Coriolis force and the pressure gradient can, to first order, describe the synoptic dynamics of the atmosphere above the planetary boundary layer. In the atmospheric boundary layer, it is necessary to consider the effects of friction, which is generally described in terms of momentum fluxes or stresses. When

the wind blows over water it produces a vertical wind shear as friction slows the wind at the water surface. This shear generates a downward flux of momentum known as wind drag or wind stress. At the air-sea interface, momentum transfer results in wave instabilities, turbulence, and the generation of drift currents. The wind stress vector, τ, is defined as:

$$\frac{\tau}{\rho} = -\langle u'w' \rangle \mathbf{i} - \langle v'w' \rangle \mathbf{j} \tag{2.1}$$

where u',v' and w' are velocity fluctuations relative to the mean in the longitudinal, lateral and vertical directions; ρ is the density of air, and the averaging time is such that the mean vertical velocity, w, is zero; **i** and **j** are unit vectors in the longitudinal and lateral directions, respectively. From this relationship it is possible to define the angle, γ, of the stress vector relative to the wind vector:

$$\gamma = \tan^{-1} \frac{\langle v'w' \rangle}{\langle u'w' \rangle}. \tag{2.2}$$

It is important to recognize that the wind direction and the stress direction are not necessarily aligned. Several recent studies, notably those by Reider and Smith (1998), Reider and Smith (1994) and Geernaert (1993) address the effects of waves and boundary layer stratification on the orientation of the stress vector.

Initially, let us consider a neutrally stratified, well-mixed boundary layer, and assume that the scale of turbulent mixing is proportional to the height, z, above the boundary layer. In this case, it is possible to specify the profile of the mean wind speed above the ocean surface as

$$U_z - U_0 = \left| \frac{\tau}{\rho} \right|^{1/2} \frac{1}{\kappa} \ln\{(z + z_0)/z_0\} \ . \tag{2.3}$$

Here, U_0 is the projected surface current speed, which in some investigations is neglected. U_z is the wind speed at height z, κ is the Von Karman constant of approximately 0.4, and z_0 is the roughness length that characterizes the average roughness of the ocean surface. If we assume that $z >> z_0$, then it is possible to rewrite Equation 2.3 in terms of the friction velocity, u*:

$$U_z - U_0 = \frac{u^*}{\kappa}\ln(z/z_0). \tag{2.4a}$$

Typically, the boundary layer is not neutrally stratified; in which case the above expression must be modified to include an empirical correction factor, ψ:

$$U_z - U_0 = \frac{u^*}{\kappa}\{\ln(z/z_0) - \psi\}. \tag{2.4b}$$

Several forms have been suggested for the stability factor, ψ. We use an expression developed by Dyer (1974) and Paulson (1970):

$$\psi(z/L) = -5(z/L) \qquad \text{if } (z/L) > 0, \tag{2.5a}$$

$$= 2\ln\left[\frac{1+X}{2}\right] + \ln\left[\frac{1+X^2}{2}\right] - 2\tan^{-1}X + \frac{\pi}{2} \text{ if } (z/L) < 0 \tag{2.5b}$$

and

$$X = (1 - 16(z/L))^{1/4}. \tag{2.5c}$$

In the above expression, L is the Monin-Obukhov length scale; it is the ratio of the momentum flux to the buoyancy flux, scaled by the Von Karman constant, and considered at referenced height z. When the boundary layer is stable, $z/L > 0$, when it is unstable, $z/L < 0$. It is expressed as

$$z/L = -g\kappa z\langle w'T_v'\rangle / \langle T_v u^{*3}\rangle, \tag{2.6}$$

where g, u* and κ are as defined above. T_v is the virtual temperature, which is defined as the temperature that dry air would need to have at a given pressure in order to have the same density as moist air, assuming ideal gas behavior (Gill, 1982).

To obtain an estimate for the friction velocity, Equation 2.4 can be rearranged in the following manner

$$u^{*2} = c_D(U_z - U_0)^2, \tag{2.7}$$

where the drag coefficient, c_D, depends on the measurement height of U above the surface, the sea state (or surface roughness), and the stability of the atmospheric boundary layer, and is defined as

$$c_D = [\kappa / \ln(z/z_0) - \psi]^2. \tag{2.8a}$$

We use a parameterization for C_D that is due to Smith (1980):

$$C_D = 1 \qquad \text{if } U_{10} < 5 \text{ ms}^{-1}$$

$$C_D = 0.879 + 0.075U_{10} \qquad \text{if } U_{10} > 5 \text{ ms}^{-1} \tag{2.8b}$$

To determine U_z, we assume U_0=0 and iteratively solve Equation (2.4b), where the stability correction is ignored for the first iteration. The friction velocity u* is determined in the course of estimating U_z.

2.2 BACKGROUND

There are several mathematical and statistical tools used to describe the behavior of waves at the ocean surface. Many excellent references address this subject. Phillips (1977) and Komen et al. (1994) were especially helpful in the preparation of this section.

To mathematically describe wave motion in a Newtonian fluid it is necessary to consider two fundamental fluid properties: conservation of mass and momentum. Conservation of mass requires that the rate of mass inflow or outflow through the

boundary of a fixed volume be equal to the rate at which mass changes within the boundary:

$$\frac{\partial \rho}{\partial t} + \nabla \cdot (\rho \mathbf{u}) = 0 \tag{2.9}$$

Here ρ denotes density, t denotes time, and u is the velocity of the fluid. Conservation of momentum is a restatement of Newton's law relating acceleration within a fluid to forces imposed on it. Assuming that the fluid of interest is incompressible, i.e. that density does not change with pressure, $\nabla \cdot \mathbf{u} = 0$, and neglecting the effects of the earth's rotation and viscosity, this relationship can be expressed as:

$$\rho \frac{D\mathbf{u}}{Dt} = -\nabla p + \rho g \,. \tag{2.10}$$

Here D/Dt denotes the total derivative, defined as $D/Dt = \partial/\partial t + \mathbf{u}\cdot\nabla$, p is pressure, and the other variables are as defined above.

If we restrict our consideration to the simple case of motion in the x-z plane, and assume that the fluid is irrotational, it is possible to express the preceding two equations in terms of a velocity potential φ(x,z,t), where $\mathbf{u}=\nabla\phi$. Under these conditions, the velocity potential satisfies the Laplace equation $\nabla^2\phi = 0$.

To obtain a solution to the above equations, it is necessary to impose a set of boundary conditions. For freely propagating gravity waves at the free surface z=ζ, where we can neglect the effects of surface tension, we require that the atmospheric pressure above the wave be constant and also negligible since the density of air is approximately one thousand times less than that of water. This is known as the 'dynamic boundary condition':

$$gz + \frac{\partial \phi}{\partial t} + \frac{1}{2}(\nabla \phi)^2 = 0. \tag{2.11}$$

At the free surface $z=\zeta$, we also require that the 'kinematic boundary condition' be satisfied. This states that water at the upper boundary must remain there, which is appropriate for non-violent conditions:

$$\frac{\partial \zeta}{\partial t} + \nabla \zeta \cdot \nabla \phi = \frac{\partial \phi}{\partial \zeta}. \tag{2.12}$$

In water of finite depth, h, an additional boundary condition is provided by prohibiting downward vertical flow at the bottom boundary, z=-h, i.e.

$$\frac{\partial \phi}{\partial z} = 0. \tag{2.13}$$

Finally, if we assume that the vertical scale of the surface disturbance is small relative to the scale of its length, these equations can be linearized to yield the following expression for the velocity potential:

$$\phi = -\frac{ag\cosh k(z+h)}{\sigma \cosh kh}\cos(kx - \sigma t + \varepsilon) \tag{2.14}$$

and for the vertical displacement of the ocean surface from its mean level:

$$\zeta(\mathbf{x},t) = a\sin(kx - \sigma t + \varepsilon). \tag{2.15}$$

Here t denotes time, a amplitude, k denotes wave number and is 2π times the inverse of wavelength, σ denotes the radian frequency and it is the inverse of the wave period, T; and ε denotes phase angle, which is arbitrary. The spatial and temporal properties of a wave given by (2.15) are coupled via a dispersion relationship

$$\sigma^2 = gk[\tanh(kh)], \tag{2.16}$$

which relates wave number and frequency for a wave in water of finite depth h. For deep water, kh>>1, and (2.16) simplifies to $\sigma^2=gk$. From the dispersion relationship it is possible to derive an expression for the phase speed c_p, where $c_p^{1/2}=\sigma/k$, and the group velocity c_g, which is given by $c_g = \frac{\partial\sigma}{\partial k} = \frac{\sigma}{2k}$.

While the above approximations are useful for describing the dynamics of a given wave, it is necessary to employ statistical techniques to characterize the dynamics of the ocean surface. That is, we consider the sea surface to be comprised of the linear superposition of a large number of dynamically independent sinusoidal waves, each component having a particular frequency, amplitude, direction and phase (Ewing (1983)). Within this statistical framework, the probability of a given surface displacement ζ_i, for a given time, t_i, and location, $\mathbf{x}_i$, can be given as $p(\zeta_i)$. Similarly, a joint probability function $p(\zeta_1, \zeta_2, ..., \zeta_n)$ specifies a particular configuration of the ocean surface as the realization of this set of n random variables.

Strictly speaking, the $p(\zeta_i)$ are not independent. However, each ζ_i is, in fact, a sum of many wave components, which can be assumed to be independent because they arose in different places before propagating to the point in question. Therefore, for a sufficiently large number of components, the Central Limit Theorem lets us treat the $p(\zeta_i)$ as Gaussian random variables. If we assume that the $p(\zeta_i)$ are invariant to either spatial or temporal shifts, i.e. $p(\zeta(x,t))= p(\zeta(x+x',t+t'))$, then the wave field is both stationary and homogeneous. Finally, if we also assume that the sea surface is ergodic, i.e. if ensemble

averages equal appropriate spatial or temporal averages, we can employ several powerful results from time series analysis.

For example, using the notation that "< >" denotes a process of averaging, we can express the covariance function for a pair of surface displacements as

$$C(\mathbf{x}',t') = < \zeta(\mathbf{x},t)\zeta(\mathbf{x}+\mathbf{x}',t+t')>. \tag{2.17}$$

This is a succinct tool for characterizing the ocean surface owing to the fact that the covariance function of a mean zero Gaussian process is the Fourier transform of the power spectral density of the process. That is, if σ denotes radian frequency and k denotes wave number, then

$$C(\mathbf{x},t) = \iint_{k,\sigma} E(\mathbf{k},\sigma)\exp(-i(\mathbf{k}\cdot\mathbf{x}-\sigma t)d\mathbf{k}d\sigma, \tag{2.18}$$

where

$$E(\mathbf{k},\sigma) = \frac{1}{(2\pi)^3}\iint_{\mathbf{x},t} C(\mathbf{x},t)\exp(-i(\mathbf{k}\cdot\mathbf{x}-\sigma t))d\mathbf{x}dt\,. \tag{2.19}$$

$E(\mathbf{k},\sigma)$ is referred to as the frequency-wave number spectrum of the ocean surface. For a detailed description of these derivations and theorems, refer to Papoulis (1987)

Since it is extremely difficult to measure the full frequency-wave number spectrum, spectral quantities obtained from integrating (2.19) such as the frequency spectrum

$$S(\sigma)=\iint E(\mathbf{k},\sigma)d\mathbf{k} \tag{2.20}$$

and the wave number spectrum

$$\Psi(\mathbf{k})=\iint E(\mathbf{k},\sigma)d\sigma \tag{2.21}$$

are used to characterize the power spectral density of waves at the ocean surface.

Realistically, the ocean surface is evolving both spatially and temporally, and the assumption of stationarity would require us to exclude many important dynamical properties of the sea surface. In addition, due to the effects of currents, it is necessary to abandon the requirement of homogeneity. Therefore it is useful to find a means of expressing some of the dynamical properties of the wave field under general conditions, provided that the temporal and spatial scales of changes to the wave spectrum are slow with respect to wave periods and wavelengths on the ocean. The wave action spectral density enables us to describe the ocean dynamics under these less restrictive conditions, and it is defined as

$$N(\mathbf{k}) = \frac{g}{\sigma}\Psi(\mathbf{k}), \tag{2.22}$$

where g denotes gravity, σ denotes frequency, and $\Psi(\mathbf{k})$ is the wave number power spectral density. The form for the above expression assumes that the density of water, ρ_w, has been divided throughout, so that the density of air is expressed as ρ_a/ρ_w (Phillips, 1985). Under slowly varying conditions, in the absence of sources, sinks or fluxes of action, the action spectral density is conserved. In general, however,

$$\frac{dN}{dt} = \frac{\partial N}{\partial t} + (c_g + \mathbf{u}) \cdot \nabla N = S_{in} + S_{ds} + S_{nl} = \mathrm{S}, \tag{2.23}$$

where c_g represents the group velocity of a slowly-varying wave packet, $\mathbf{u}$ denotes a surface current if one is present, and the right hand side specifies the means by which the action is changed: S_{in} represents the action input from the wind, S_{nl}, represents wave-wave nonlinear interactions, and S_{ds} represents action dissipation by wave breaking and viscosity.

For several decades, gaining an improved understanding of the three components of S, the so-called source terms, has remained an active area of oceanographic research.

Although there is a fair amount of agreement regarding certain attributes of S_{in}, S_{ds} and S_{nl}, there is still considerable uncertainty regarding which processes should be included and how the processes should be modeled.

There have been many ocean spectral models presented in the oceanographic and ocean remote sensing literature. In the following paragraphs, we introduce four ocean wave spectra that have particular relevance to this research, three of which are models and one that is derived from remote measurements of the ocean surface. These spectra are discussed both for their historical relevance and because of their possible utility in an operational application of the ASM that is discussed later in this chapter.

One of the first realistic and accurate ocean spectral models was an empirical model developed by Pierson and Moskowitz (1964), based on analysis of *in situ* measurements of waves at the ocean surface. This model is given by the expression

$$Z(\sigma) = \frac{\alpha g^2}{2\sigma^5}\exp(-0.74(\sigma_c/\sigma)^4), \tag{2.24}$$

where Z (σ) denotes the power spectral density associated with a given radian frequency σ; g denotes gravity, $U_{19.5}$ is the wind speed measured at 19.5 m above the ocean surface in a neutrally stratified boundary layer, $\sigma_c=g/U_{19.5}$, and $\alpha=0.008$, a parameter used to establish the level of the spectral tail. This model is only valid, however, for a fully developed sea, i.e. an infinite fetch and duration. Although it is recognized as being overly simplistic and applicable under a limited range of conditions, this model is nonetheless very useful as a cursory standard for comparison with spectral measurements and models, and as such, this model is still referred to regularly, nearly 35 years after its development.

A few years later, an intensive experimental effort was undertaken in the North Sea, the primary goal of which was to investigate 'the structure of the source function governing the energy balance of the wave spectrum, with particular emphasis on wave growth under

stationary offshore wind conditions...' (Hasselmann et al.,1973). One of several important results that arose from this project was a fetch dependent frequency spectrum known as the JONSWAP (Joint North Sea Wave Project) Spectrum. This model obtains predictions of the power spectral density, S(f), associated with a given linear frequency f (given in Hz: $f = \sigma/2\pi$, where σ is angular frequency). The JONSWAP Spectrum is given by (Hasselmann et al.,1973):

$$S(f) = \alpha_j g^2 (2\pi)^4 f^{-5} \exp\left\{-\frac{5}{4}\left(\frac{f}{f_p}\right)^4\right\}\gamma_j^{\Gamma}, \tag{2.25}$$

where

$$\Gamma = \exp\left\{-(f - f_p)^2 / 2\sigma_j^2 f_p^2\right\}$$

with

$$\alpha_j = 0.076\left(\frac{Xg}{U_{10}^2}\right)^{-0.22}, \ \gamma_j = 3.3, \ \sigma_{ja} = 0.07, \text{ and } \sigma_{ja} = 0.09.$$

This spectral formulation is determined by five variables. Two parameters characterize the forcing: wind speed U (measured at 10 m above the ocean surface) and fetch X_j; three parameters characterize the spectral shape: the height (γ) and the width (σ_a and σ_b) of the spectral peak.

Unlike subsequent, more sophisticated models, the JONSWAP spectrum only requires the specification of a few parameters; unlike the Pierson-Moskowitz spectrum, it is capable of modeling spectral dependence on fetch. In addition, the findings from the JONSWAP experiment significantly advanced our ideas on the dynamical balance in a wind sea and opened the way to more sophisticated wave prediction modeling (Donelan and Hui, 1990). It is still widely used in many applications.

For many years, ocean wave models have been evolving, driven by increased

understanding in the physics of the source terms and by improved computational capabilities. In the so-called first generation models, only S_{in} exhibited realistic physical properties. The dissipation term S_{ds} was modeled in such a way as to prohibit the spectrum from exceeding a saturation level, and the nonlinear interaction term was parameterized in a simple manner. Due to this treatment of the nonlinear interaction, each spectral component evolved essentially independently of all other spectral components. In second generation models such as JONSWAP, coupling between wave components was introduced by use of a parameterized version of the wave-wave interaction processes and so wave components ceased to evolve independently.

A third generation wave model that is enjoying widespread use is known as the WAM (for WAve Model). This model represents many years of research by several international groups and has been extensively documented. For detailed descriptions about this model and its capabilities, the reader is referred to Komen et al. (1994). The WAM model is capable of modeling the growth and evolution of waves under many different types of conditions; for example it is capable of modeling wave-current interactions and the effects of bottom topography. There is a price, however, for all these options and flexibility: it is somewhat complicated to run the WAM model, and it requires the initialization and specification of numerous input parameters, many of which are not known on the open ocean. In addition, the WAM is primarily intended for application to wave prediction at the regional and global scales, scales that are comparatively large relative the regime of interest for radar scatterometry.

The final ocean spectrum mentioned here is based on remote measurements rather than a model. For several years, it has been possible to extract estimates of ocean wave spectra from Synthetic Aperture Radar (SAR) measurements of the sea surface. One procedure for doing so is described in Komen et al. (1994). Factors, such as system calibration and measurement errors, govern the how readily these spectra can be applied

operationally. Nonetheless, under appropriate conditions, these spectra can represent a viable alternative to model-based spectra.

2.3 OVERVIEW OF THE AGGREGATE SPECTRAL MODEL

As suggested in the preceding section, there are several spectral models already in existence that are potentially applicable to this work. Recently, Jensen (1996) provided a compilation of published ocean wave spectra that includes 29 different models. With so many models available from which to choose why consider another spectral form? Essentially, this was because we did not find any existing spectral models that met the following requirements that we hoped, whenever possible, to satisfy:

1 Use models that are physically-based, so that a model result has a corresponding physical interpretation.

2 Use models based on data acquired on the open ocean and not from wave tanks. "Because of the much smaller scales it is not clear whether the characteristics of the wave number spectra obtained in laboratory experiments can be extrapolated to field conditions as found on the open ocean ", (Klinke and Jahne, 1992).

To date, however, there have been no *in situ* measurements of the wave number spectrum obtained directly on the open ocean at high wave numbers. Banner et al. (1989) obtained measurements of the wave number spectrum for waves between 0.2 m and 1.6 m on the open ocean, but this falls short by nearly an order of magnitude of the ERS-1 Bragg waves on the ocean surface. Jahne and colleagues obtained measurements extending to much higher wave numbers, but only in wave tanks.

In order to be used in conjunction with a composite surface, or two-scale scattering

model, it is necessary to have an accurate ocean wave spectral model that applies to waves of vastly different scales. The Bragg scatterers for this investigation are on the order of a few centimeters, but these waves are tilted and modulated by the underlying wave field, which encompasses waves on the order of tens to hundreds of meters.

Typically, the spectral models that we encountered applied to a limited regime of ocean waves; no one applied over all the scales relevant to predicting ocean backscatter. Also, models of the highest wave number regime were either based on remote measurements, data collected in wave tanks, or both. Models of the lowest wave number regime faced considerable difficulties with modeling the effects of swell. To address the above-mentioned requirements, we developed a spectral form based on partitioning the ocean wave number spectrum into different regimes; each treated with a different approach. For this reason, we call the resulting spectrum the 'Aggregate Spectral Model' (ASM). In the following sections, we present a closer look at each of the components of the ASM.

2.4 NDBC BUOY DATA

One of our earliest decisions in developing the ASM was to employ buoy measurements to characterize the low wave number portion of the spectrum. At first glance this seems ill advised: if ultimately the goal is to characterize the wind field on the open ocean where buoys are absent, why develop an ocean wave model that requires the use of buoy measurements? At the present time, it is recognized that there are often considerable errors in the low wave number spectra predicted by the WAM Model (Komen et al. (1994), JONSWAP (Hasselmann et al. (1973) and SAR-derived spectra (Komen et al. (1994). By using *in situ*, buoy-measured spectra during development of the ASM, rather than one of the above low-wave number spectra, the errors arising from this regime would be minimal. This would, therefore, enable us to concentrate our modeling efforts on the primary region

of interest, the high wave number Bragg scatterers, with a minimum contribution of errors from the other regimes. In addition, as will be discussed in Chapter 3, by taking this approach we were able to investigate the impact on radar scatterometer measurements of effects due to the modulation and tilting by the long waves. Future realizations of this model can easily incorporate one of the low wave number spectra mentioned in Section 2.2 so that buoy data will not be required and application of the ASM on the open ocean will be practical.

An additional reason for confining model development efforts to be located in the vicinity of the NDBC buoys was the need to verify the stress retrievals obtained from the scatterometer measurements. It would be necessary to know the 'true' friction velocity and direction at a given location, to use as a basis for comparison with the model-based estimates.

The NDBC network of buoys for the southeastern region of the United States is illustrated in Figure 2.1a; the network for the southwestern region is illustrated in Figure 2.1b. These buoys obtain hourly measurements of the following atmospheric and oceanic properties: significant wave height, mean wave period, dominant wave period, mean wave direction, dominant wave direction, air temperature, dew point, barometric pressure, wind speed (average), wind direction (average), sea surface temperature and salinity. These data are available to the public via the Internet (www.seaboard.ndbc.noaa.gov) and also on CD-ROM. Table 2.1 provides a summary of relevant statistics describing the NDBC buoys. Only a limited number of the NDBC buoys are capable of measuring the directional wave frequency spectrum. Typically, these measurements are obtained between the frequencies of 0.03 and 0.35 Hz, which corresponds to wave numbers between $k=0.0036\ m^{-1}$ and $k=0.49\ m^{-1}$. Longuet-Higgins, Cartwright and Smith (1963) were the first to address the problem of reconstructing the directional spectrum from measurements of the pitch, roll and vertical displacement of the buoy over time. An overview of their approach is presented below, based on an excellent review by Benoit (1992).

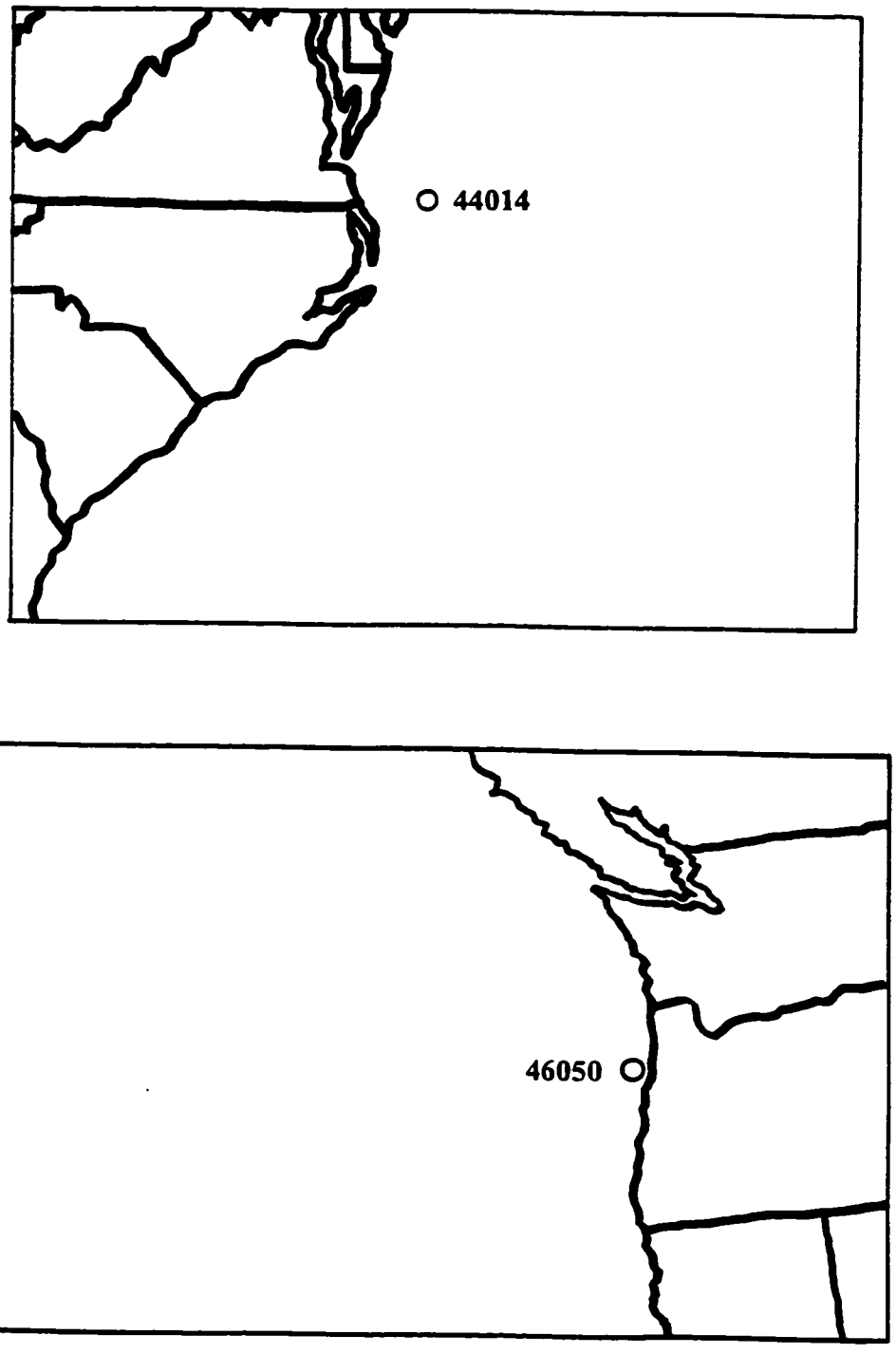

Figure 2.1: Map indicating the location of the two NDBC buoys used in this research: Figure (2.1a) indicates the location of buoy 44014, off the coast of Norfolk Virginia. Figure (2.1b) indicates the location of buoy 46050, in Yaquina Bay, Oregon.

Parameter	Range	Frequency	Avg. Period	Resolution	Accuracy
Wind Dir.	0 - 355	1.28 Hz	8 min	10 degrees	-10 degrees
Wind Speed	0 - 61.8 m/s	1.28 Hz	8 min	1 m/s	+/- 1 m/s (or 10%)
Wind Gust	0 - 82.4 m/s	1.28 Hz	5 sec	1 m/s	+/- 1 m/s (or 10%)
Air Temp.	-40 - 50 C	1.28 Hz	8 min	0.1 C	(+/- 1C)
Pressure	800 - 1100hPa	1.28 Hz	8 min	0.1 hPa	+/- 1 hPa
Water Temp.	-5 - 40 C	1.28 Hz	8 min	0.1 C	(+/- 1C)
Wave Height	0 - 35 m	2.56 Hz	20 min	0.1 m	+/- 0.2 m (or 5 %)
Wave Period	0 - 30 sec	2.56 Hz	20 min	1 sec	+/- 1 sec
Wave Spectra	0 - 999 m^2/Hz 0.01 - 0.4 Hz	2.56 Hz	20 min	0.01 Hz	--
Rel. Humidity	0 - 100 %	1 Hz	1 min	0.10%	+/- 6%
Solar Rad'n	0 - 2.50 w/m^2	1 Hz	8 min	0.5 w/m^2	+/- 5 %
Precipitation	0 - 999 mm	continuous	6 hr	1.0 mm	5.0 mm

Table 2.1: Summary of NDBC Buoy Measurement Accuracies, Sampling Rates and Relevant Statistics.

First, we assume that the two-dimensional spectrum can be decomposed into a function of frequency and a function of direction, i.e.

$$S(f,\theta)=E(f)D(f,\theta), \tag{2.26}$$

where E(f) is the one dimensional power spectral density that can be estimated from a single record of sea surface elevation. It is related to the directional spectrum via

$$E(f) = \int_0^{2\pi} S(f,\theta)d\theta . \tag{2.27}$$

The directional spreading function, D(f,θ), is given by

$$D(f,\theta)= \int_0^{2\pi} D(f,\theta)d\theta = 1 \text{ , where } D(f,\theta)\geq 0 \text{ over } [0,2\pi]. \tag{2.28}$$

Given the above relationships, it is possible to reconstruct the directional spectrum from the quantities measured by the buoys. If we denote the vertical displacement of the buoy by $\zeta(x,y,t)= X_1(t)$, and the pitch and roll of the buoy (i.e. the slope of the sea surface in two orthogonal directions) by

$$\frac{\partial \zeta}{\partial x}(t) = X_2(t) \text{ and } \frac{\partial \zeta}{\partial y}(t) = X_3(t) , \tag{2.29}$$

then we can define the cross spectrum $G_{ij}(f)$ for each pair of these three quantities as

$$G_{ij}(f)=2. \int_{-\infty}^{\infty} R_{ij}(\tau)e^{-i2\pi f\tau}d\tau , \tag{2.30}$$

where

$$R_{ij}(\tau)=(\lim T \to \infty)\frac{1}{T}\int_0^T X_i(t)\cdot X_j(t+\tau)dt . \tag{2.31}$$

The $G_{ij}(f)$ can be written using complex notation as $G_{ij}(f)= C_{ij}(f)-iQ_{ij}(f)$, where $C_{ij}(f)$ is the co-spectrum and $Q_{ij}(f)$ is the quad-spectrum. Using this notation, the cross-correlation coefficients for the buoy motions can be estimated by:

$$C_{11}(f)=\int_0^{2\pi} S(f,\theta)d\theta = E(f) \tag{2.32a}$$

$$C_{22}(f)=E(f)k^2\int_0^{2\pi} D(f,\theta)\cos^2\theta d\theta \tag{2.32b}$$

$$C_{33}(f)=E(f)k^2\int_0^{2\pi} D(f,\theta)\sin^2\theta d\theta \tag{2.32c}$$

$$C_{23}(f)=E(f)k^2\int_0^{2\pi} D(f,\theta)\cos\theta\sin\theta d\theta \tag{2.32d}$$

$$Q_{12}(f)=E(f)k\int_0^{2\pi} D(f,\theta)\cos\theta d\theta \tag{2.32e}$$

$$Q_{13}(f)=E(f)k\int_0^{2\pi} D(f,\theta)\sin\theta d\theta \tag{2.32f}$$

$$Q_{11}(f)=Q_{22}(f)=Q_{33}(f)=Q_{23}(f)=0 \tag{2.32g}$$

$$C_{12}(f)=C_{13}(f)=0. \tag{2.32h}$$

In addition, we have the relationship $C_{22}(f)+C_{33}(f)=k^2C_{11}(f)$, which enables us to calculate the wave number, k . Therefore, for a given frequency, there are only four independent coefficients available for computing the directional spreading function subject to the requirement of continuity over $[0,2\pi]$. Several approaches have been developed for reconstructing the directional spreading function from these parameters, twelve of which were evaluated and compared by Benoit (1992). We will only discuss two of these here: the original work in this subject by Longuet-Higgins et al. (1963), and a more recent effort due to Oltman-Shay and Guza (1984). Longuet-Higgins et al. expressed the directional spreading function $D(f,\theta)$ as a weighted, truncated Fourier series using the cross-correlation coefficients, above:

$$D(f,\theta)= \frac{1}{2}a_0 + \frac{2}{3}(a_1\cos\phi + b_1\sin\phi) + \frac{1}{6}(a_2\cos 2\phi + b_2\sin 2\phi)\,, \qquad (2.33a)$$

where

$$a_0=\frac{1}{\pi}C_{11} \qquad a_1=\frac{1}{\pi k}Q_{12} \qquad a_2=\frac{1}{\pi k^2}(C_{22}-C_{33}) \qquad (2.33b)$$

$$b_1=\frac{1}{\pi k}Q_{13} \qquad b_2=\frac{1}{\pi k^2}C_{23}$$

This method for spectral reconstruction, in principle, should never assume negative values. Under some conditions, however, this does occur. In addition, this representation results in considerable directional broadening of ocean wave energy. Consequently, we sought an alternative expression for $D(f,\theta)$. Analyses by Benoit (1992) and Earle (1993) suggest that the method of Maximum Likelihood developed by Oltman-Shay and Guza (1984) does not encounter the problem of occasionally predicting negative energy, has superior directional resolution compared to the approach of Longuet-Higgins et al., is straight-forward to implement and is also computationally efficient. The method of Maximum Likelihood estimates the spreading function as a linear combination of the cross spectra. That is,

$$D(f,\theta)=\sum_{i=1}^{3}\sum_{j=1}^{3} w_n^*(\theta)w_m(\theta)\cdot G_{ij}(f)\,, \qquad (2.34)$$

where the weighting coefficients, w_n, are calculated with the condition of unity gain of the estimator in the absence of noise. The big advantage of the maximum likelihood technique is that it takes advantage of the side condition that the spectrum must be non-negative, and in this way is able to obtain improved resolution (Lawson and Long, 1983).

The primary waves of interest in scatterometer-based wind retrieval are those that are locally generated. Therefore, at least initially, we restricted our analyses to cases where a minimum of swell was present. In order to accomplish this, our preliminary analyses only employed buoys located along the East Coast of North America and also only

considered cases where the wind was directed offshore. For the purposes of developing and validating this approach, imposing these restrictive conditions helped to simplify some of the analyses. Subsequent efforts demonstrated the viability of this wind retrieval technique under a broader range of conditions.

Much of the work presented in this thesis is based on measurements made by NDBC buoys 44014 and 46050. Buoy 44014 has been used extensively in several measurement campaigns such as the SWADE experiment of 1991 and the ARSLOE experiment of 1980 and so its characteristics are well known. It is a 3-meter Pitch-Roll Discus Buoy, located approximately 83 km off the coast of Norfolk, Virginia (36° 34' 59" N, 74° 50' 1" W) in water of about 48 meters depth. The effect of finite depth at this location has been shown (Wang and Friese, 1997) to be significant only for waves with frequencies less than 0.08 Hz; in general these waves have been excluded from this study. Examples of spectra measured by this buoy are depicted in Figures 2.2a and 2.2b. Buoy 46050 is also a 3-meter discus buoy; it is located in Yaquina Bay, Oregon (44° 36' 44" N, 124° 30' 46" W), in water of about 130 meters depth.

All of the NDBC buoys are equipped for measuring the one-dimensional frequency spectra of ocean waves, which for this range of frequencies can be readily converted to wave number spectra using the dispersion relationship for linear gravity waves. The two above-mentioned buoys are also equipped for making measurements of the two-dimensional, directional frequency spectrum of ocean waves.

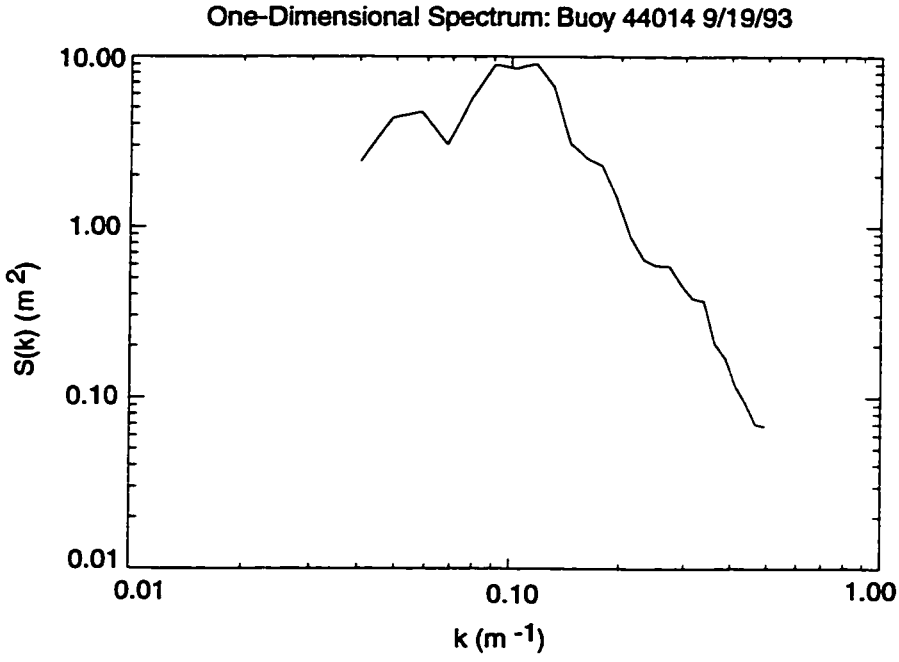

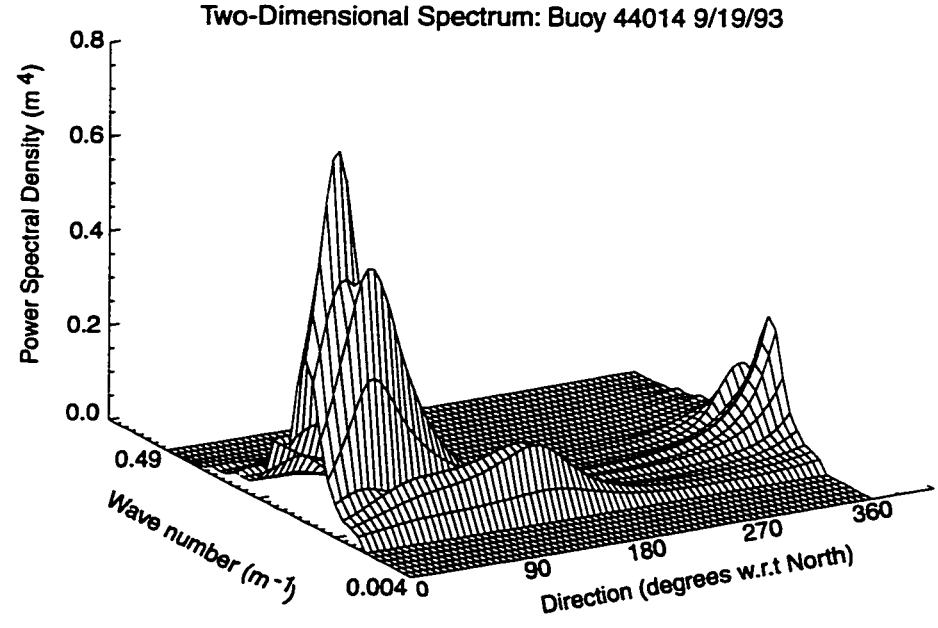

Figure 2.2: Examples of one- and two-dimensional spectra measured by NDBC buoy 44014 from 9/19/93.

2.5 EQUILIBRIUM SPECTRAL MODELING

The concept of statistical equilibrium has been used for over half a century as a means of simplifying the study of complicated phenomena, such as turbulence. If one restricts consideration to particular temporal or spatial scales, a state of equilibrium can be envisioned among the various components of a dynamical system. For example, such a condition exists in modeling ocean wave spectra when the three source terms of the balance of action spectral density, introduced in Equation 2.23, satisfy the following:

$$S_{in} + S_{ds} + S_{nl} = 0. \tag{2.35}$$

Here, S_{in} represents the action input from the wind, S_{nl} represents wave-wave nonlinear interactions, and S_{ds} represents action dissipation by wave breaking. Several authors, notably Phillips (1985), Kitaigorodskii (1983), Komen et al. (1984) and Banner et al. (1989) have investigated this balance. In this section we will focus on the models of Phillips (1985) and of Banner et al. (1989). It is interesting to note that both Phillips (1985) and Kitaigorodskii (1983) arrived at similar expressions for the equilibrium spectrum, beginning from quite a different set of assumptions.

In Phillips' model for wind-generated gravity waves, such a state of statistical equilibrium exists among those waves where the time scales of wave growth is much larger than the time scales of energy input, dissipation or exchange; far from the influence of the spectral peak. Under these conditions it is possible to obtain expressions for each of the source terms. These are described in the following paragraphs.

The source term that characterizes the action input due to the wind, S_{in}, is believed to be the best understood of the source terms. Plant (1982) suggested a form for this term

$$S_{in}(\mathbf{k}) = m\cos\theta\sigma\left(\frac{u^*}{c_p}\right)^2 N(\mathbf{k}), \tag{2.36}$$

where m is approximately 0.04, c_p is the phase velocity for the wave component of frequency σ, u* is the friction velocity, N(**k**) is the action spectral density, and θ is the angle between the wind vector and the wave propagation direction. Phillips (1985) provided a dynamical basis for this expression. S_w can also be expressed in terms of the degree of saturation B(**k**), where $B(\mathbf{k})=k^4\Psi(\mathbf{k})$, if one assumes a different form for the directional spreading of wave energy:

$$S_{in} = m\cos^{2p}\theta g k^{-4}\left(\frac{u^*}{c_p}\right)^2 B(\mathbf{k}). \tag{2.37}$$

S_{nl} is the source term for specifying the transfer of wave action through interactions between waves and the value for the parameter p is to be deduced from observational data (Phillips, 1985).

Phillips (1960) first obtained the resonant condition for gravity waves on deep water. Subsequently, Hasselmann (1962, 1963) developed an expression for this transfer of energy due to resonant interactions between four wave components

$$S_{nl}(\mathbf{k}) = \sigma\iiint d\mathbf{k}_1 d\mathbf{k}_2 d\mathbf{k}_3 Q^2(\mathbf{k}_1,\mathbf{k}_2,\mathbf{k}_3,\mathbf{k}) \times \delta(\mathbf{k}_1+\mathbf{k}_2-\mathbf{k}_3-\mathbf{k})\delta(\sigma_1+\sigma_2-\sigma_3-\sigma)$$
$$\times[N_1N_2(N_3+N)-N_3N(N_1+N_2]$$

(2.38)

In this expression, the Dirac delta, δ, selects those wave number components that obey the resonance conditions for interaction between gravity waves:

$$\mathbf{k}+\mathbf{k}_1=\mathbf{k}_2+\mathbf{k}_3, \text{ and } \sigma+\sigma_1=\sigma_2+\sigma_3, \tag{2.39}$$

where the N_i specify the action spectral density for each selected component and Q is a cubic coefficient describing the coupling between these components. In the equilibrium range of the spectrum, waves from the same neighborhood of wave number space dominate these interactions, suggesting that here, the flux of action density will scale as $N(\mathbf{k})$ itself. This then suggests a form for the net spectral flux divergence of the form

$$S_{nl} \propto Q^2 N^3(\mathbf{k}) k^4 / \sigma \propto g^{-1/2} k^{19/2} N^3(k) \tag{2.40}$$

which, in terms of the degree of saturation $B(\mathbf{k})$, can be written

$$S_{nl} \propto g k^{-4} B^3(\mathbf{k}). \tag{2.41}$$

The source term with which the greatest uncertainty is associated is S_{ds}. This is reflected in the many different models that have been suggested for the dissipation source term, e.g. Hasselmann (1973), Donelan and Pierson (1987), Plant (1986) and Phillips (1985). While the primary mechanisms responsible for energy dissipation are recognized: wave breaking, viscous damping and generation of parasitic capillary waves (Donelan and Hui, 1990), the extent to which each mechanism contributes to dissipation in a given wave regime and how it should be modeled is still not clear.

It is worth mentioning that Equation (2.35) requires that all three source terms sum to zero for all wave numbers. However, if two of these terms are specified mechanistically, then the third term must be the negative of the sum of the other two. If each term is modeled separately, then, generally, they will not sum to zero.

An expression for the dissipation source term in this regime was suggested by Phillips on the basis that statistical equilibrium be achieved by a balance between *all three* source terms:

$$gk^{-4}B^3(\mathbf{k}) \propto gk^{-4}f(B(\mathbf{k})) \propto m\cos^{2p}\theta gk^{-4}\left(\frac{u^*}{c_p}\right)^2 B(\mathbf{k}) \tag{2.42}$$

Here, the input and interaction terms are expressed as functions of the degree of saturation $B(\mathbf{k})$; the dissipation term is expressed as $f(B(\mathbf{k}))$. If we equate the terms representing nonlinear interaction and the input from the wind, it is possible to rewrite the degree of saturation as

$$B(\mathbf{k}) = \beta\cos^p\theta\left(\frac{u^*}{c_p}\right), \tag{2.43}$$

where β is a constant, which implies that

$$f(B(\mathbf{k}))=\gamma B^3(\mathbf{k}), \tag{2.44}$$

where γ is a constant.

If we rewrite the original definition for $B(\mathbf{k})$ in terms of Equation (2.13), it is possible to write

$$\Psi(\mathbf{k}) = \beta\cos^p\theta\left(\frac{u^*}{c_p}\right)k^{-4}=\beta(\cos\theta)^p u^* g^{-1/2}k^{-7/2} \tag{2.45}$$

which is Phillips' definition for the wave number spectrum in the equilibrium range. The corresponding frequency spectrum is given by

$$S(\sigma)=\alpha u^* g\sigma^{-4}. \qquad (2.46)$$

This model is in general agreement with several experimental data sets e.g. Forristall (1981), Kawai et al. (1977) and Kondo et al. (1973). The more recent, high-wave number measurements obtained in wave tanks by Jahne and Riemer (1990) and Klinke and Jahne (1992) are also consistent with this model. Experimental wave measurements made on the open ocean by researchers at the Johns Hopkins University Applied Physics Laboratory, that are presented in Section 2.6, also support an ocean wave spectrum of this form.

Banner et al. (1989) conducted an experimental measurement program in 1984 and 1986 that obtained stereophotographs of gravity waves between 0.2 and 1.6 m. On the basis of these spatial observations, they proposed the following one-dimensional wave number spectrum for the equilibrium range:

$$\varphi(k) \sim \left(\frac{u^{*2} k}{g}\right)^{\gamma} k^{-3} . \qquad (2.47)$$

Here k denotes wave number, g denotes gravity, u* is friction velocity, and $\gamma = 0.09 \pm 0.09$. This expression is consistent with a two-dimensional wave number spectrum of the form $\psi(\mathbf{k})\sim Ak^{-4}$, which, although based on an entirely different approach, is similar to an earlier spectral form suggested by Phillips (1958). The spectral form of Banner et al. is also in general agreement with several experimental data sets, e.g. Donelan et al. (1985) and Kahma (1981).

Either the spectral form of Banner et al. or Phillips' model could potentially be used to characterize the mid-range of wave numbers for the ASM. We decided to use the equilibrium spectral model of Phillips in the ASM because it is based on physical and dimensional arguments. Data sets from the late 1970s and early 1980s that were used to validate this model on the open ocean, encompassed wavelengths on the order of several, to tens of meters, all of which fell short of the Bragg regime for ERS-1 by at least an order

of magnitude. It was necessary, therefore, for us to determine whether or not this model was appropriate for characterizing the centimeter-scale Bragg waves for the ERS-1 system. To address this issue, we looked at data sets that had been acquired at scales closer to that of the ERS-1 Bragg waves on the open ocean, to determine whether or not this model was appropriate for ocean waves with wavelengths on the order of a few centimeters.

2.6 HIGH WAVE NUMBER REGIME

Few measurements of centimeter-scale waves have been collected on the open ocean, especially in wave number space. There have been several successful measurements made at this scale in wave tanks, e.g. Klinke and Jahne (1992) and Jahne and Riemer (1990), but it is unclear how applicable these data are to the conditions on the open ocean. Late in the spring of 1990, researchers from the Johns Hopkins Applied Physics Laboratory made a suite of high frequency wave measurements off Andros Island in the Caribbean Sea (Nelson, 1990). This data collection effort was known as the 'Standard Leopard' (SL) experiment and we were fortunately given access to these data. The environmental conditions that prevailed during the days on which the experiment was conducted are summarized in Table 2.2. Friction velocity measurements were not obtained during the SL experiment, but we were able to obtain estimates of u* for each data collection interval using the technique outlined at the beginning of this chapter. The *exact* wind speed during each measurement period was not known, but the maximum and minimum wind speeds for each interval were provided. Therefore, for each data set we obtained two estimates for u*: one based on the maximum wind speed and one based on the minimum.

Several research vessels participated in the SL experiment and collected a suite of atmospheric and oceanic measurements. Two buoys were also deployed for measuring ocean wave power spectral densities. The first was a 13-m long, 400 kg spar buoy equipped with a high-resolution, high-frequency capacitive wave gauge system capable of measuring frequencies between 0.06 and 6.0 Hz. This buoy is illustrated in Figure 2.3. The wave gauge on this buoy employed a tantalum wire (diameter 0.63 mm, length 3.0 m) mounted at the water line. The details regarding the filtering, averaging and processing of these data are provided in Nelson (1990). An example of measurements obtained by the spar buoy from two different days during the experiment is provided in Figure 2.4 a and b.

	5/31/90	6/3/90	6/4/90	6/5/90	6/7/90	6/9/90
Wind Speed (m/s)	3.0 - 4.0	6.0 - 8.0	3.0 - 5.0	4.0 - 5.0	6.0 - 9.0	8.0 - 10.0
Air Temp (deg. C)	27.2	26.5	27.5	27.3	27.5	27.4
Sea Temp. (deg. C)	26.9	26.8	27.7	27.3	27.5	27.5
Humidity (%)	94	81	81	81	85	75
Wind Dir. (deg. Wrt N)	150	80 - 115	105 - 145	150 - 160	105 - 120	110 - 115
Sig. Wv. Ht. (m)	0.12	0.44	0.16	0.1	0.87	0.92
Wave Slope	0.061	0.092	0.102	0.098	0.102	0.118
u^* (m/s)	0.08 - 0.11	0.20 - 0.29	0.09 - 0.12	0.12 - 0.15	0.21 - 0.33	0.29 - 0.38

Table 2.2: Summary of measurement conditions during the Standard Leopard Experiment conducted in the late Spring of 1990 in the Caribbean Sea

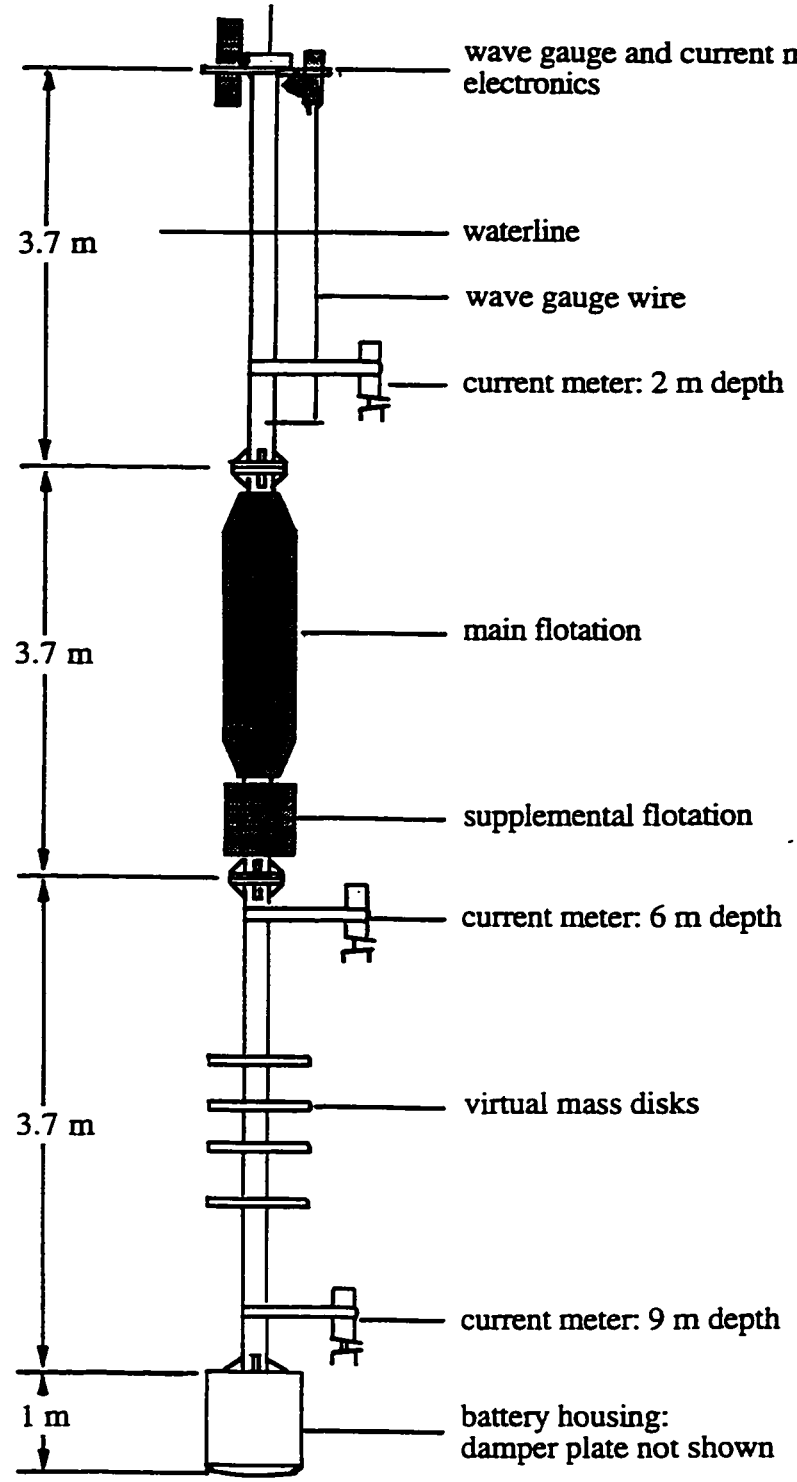

Figure 2.3: Wave spar buoy used in the Standard Leopard Experiment, from Nelson (1990).

In addition to the spar buoy, a 0.8-m diameter, 200-kg wave riding buoy (manufactured by ENDECO) was deployed in the experiment. This buoy's instrumentation included an accelerometer on a pendulum in the base of the buoy's tail section that measured the buoy's vertical accelerations. When integrated twice, the accelerometer measurements provided estimates of wave height. In response to wave orbital forces, the wave-riding buoy tilted forward at wave crests and back at a trough; these tilt measurements made it possible to determine the dominant wave direction. Both buoys were deployed from a boat and allowed to drift freely within a designated area. Each buoy obtained measurements over a different range of frequencies, but there was a range of overlap where measurements were obtained by both buoys. In this region of overlap, the two spectra were compared to verify the spar buoy's performance. An example of one such comparison is provided in Figure 2.5.

The SL data provided us with measurements of high frequency gravity waves made on the open ocean. Our primary interest in these data was to obtain estimates of the wave number spectrum and to determine whether or not they behaved in accordance with the equilibrium spectral model given by Equation (2.45). We used these spectral measurements, obtained on the open ocean, to help us determine the appropriate spectral form to use in modeling the smallest gravity waves, which would in turn serve as the basis for our radar backscatter predictions. The SL spectra were obtained in frequency space, however, and composite surface scattering codes require ocean wave number spectra for input. Before embarking on analysis of the wave number spectra associated with these frequency measurements, we made some cursory comparisons between these data and Phillips' equilibrium spectral model as specified in frequency space (Equation (2.46)).

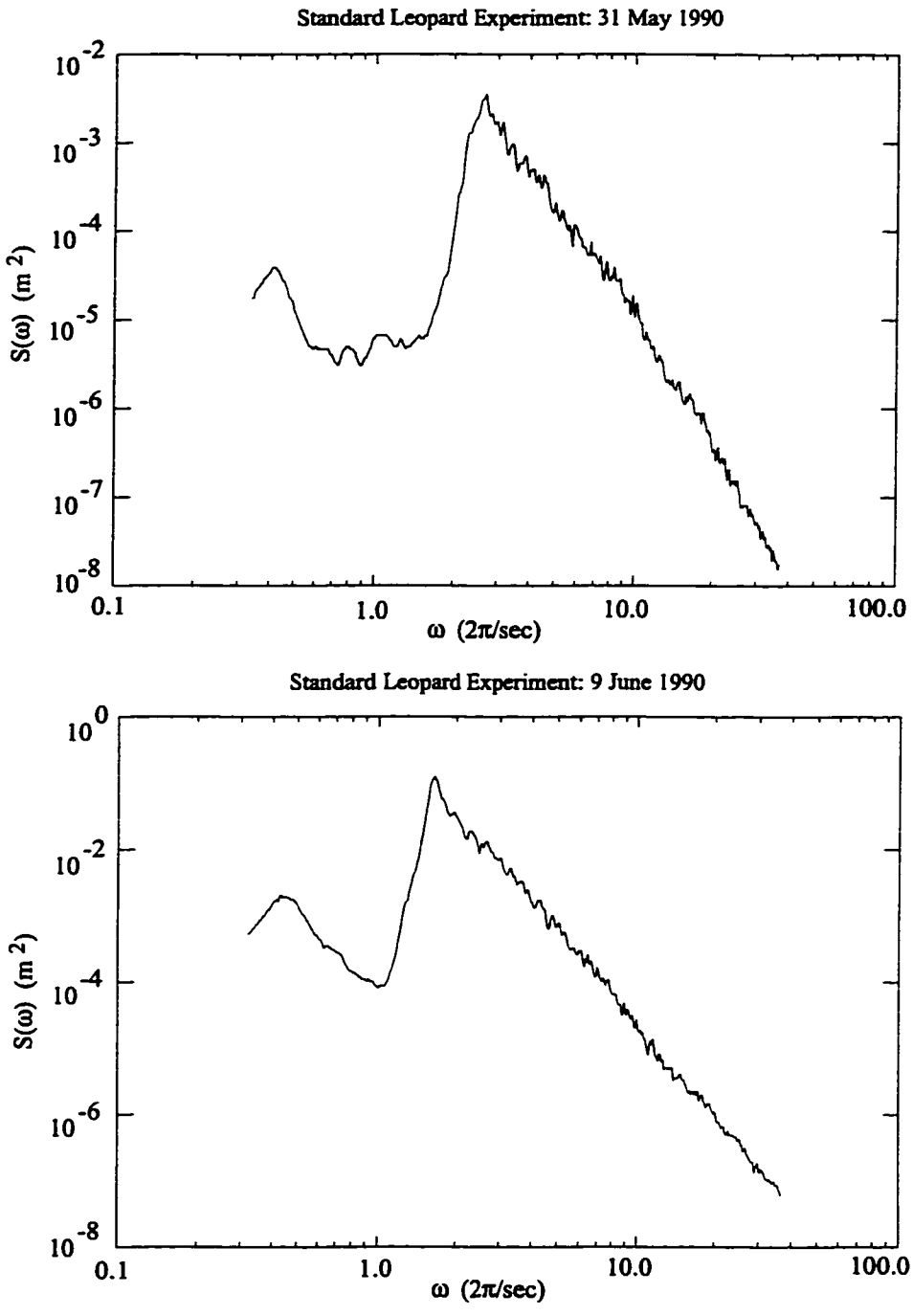

Figure 2.4: Example of two Standard Leopard frequency spectra illustrating regime in which the measurements were obtained. Note that in the upper panel, u* ~ 0.1; in the lower panel, u*~ 0.3

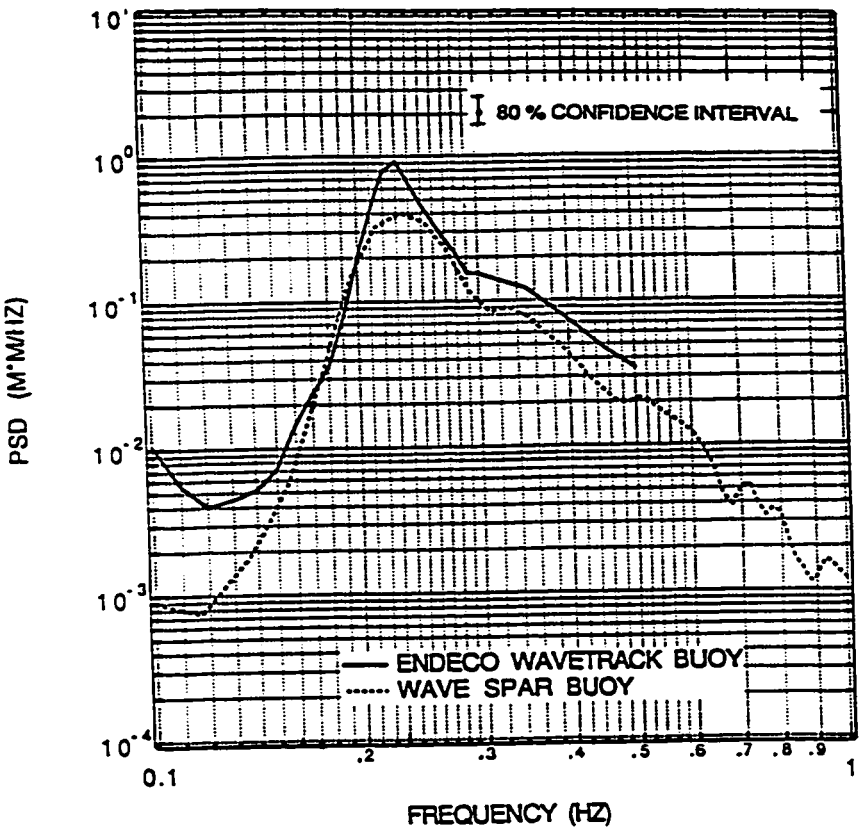

Figure 2.5: Comparison of measurements obtained by ENDECO buoy and spar buoy during the Standard Leopard Experiment, 1990. This figure illustrates the different sensitivities of the two buoys, from Nelson (1990).

For example, Figure 2.6 depicts one such comparison between the SL frequency spectra and Phillips' model. This figure is plotted using units suggested in Figure 3 of Phillips (1985). For the ERS-1 radar data, a typical Bragg resonant wave frequency corresponds roughly to ω=38; which, for a typical u* of 0.2, would lead to a value of $\omega u^*/g$=0.77. In this plot, if we use the maximum u* for the data collection interval, we obtain the curve characterized by the heavy dotted line; if we assume the minimum u*, we obtain the heavy solid line. In the equilibrium spectral model, the parameter α sets the overall level of the spectrum. Phillips (1985) provided a summary of α values from

several different field experiments and they fall within the range (0.06 -0.11). In Figure 2.6, the lower, light gray line illustrates Phillips' model assuming α=0.06; the upper, dark gray line assumes α=0.11. To first order, the data appear to be somewhat consistent with the model.

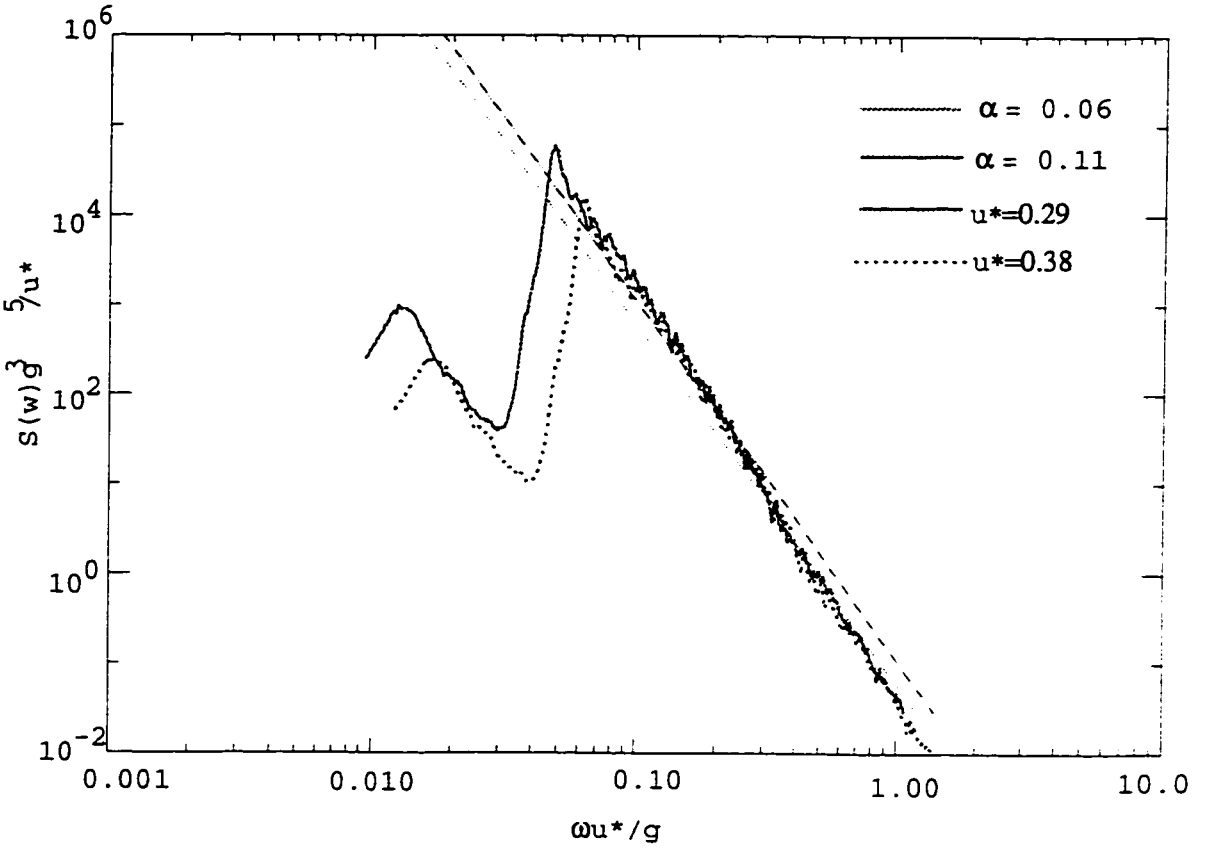

Figure 2.6: Comparison of Standard Leopard Frequency Spectra with Phillips' Equilibrium Theory in non-dimensional units. In the above plot, the heavy solid curve corresponds to the SL measured frequency spectrum if we assume the minimum friction velocity (u*=0.29); the heavy dashed curve corresponds to the SL measured frequency spectrum if we assume the maximum friction velocity (u*=0.38) during the measurement interval. This plot corresponds to SL measurements obtained on 9 June 1990.

On closer examination, however, an appreciable portion of each spectrum falls outside of the region defined by the extreme values of α. This prompted us to investigate possible sources for this disagreement between the model and the data. First, by definition, Phillips' equilibrium spectral model assumes that α is essentially constant throughout the equilibrium range. There have been efforts suggesting that there are conditions under which this relationship does not hold. For example, Toba et al. (1988) found that under circumstances of rising winds α tends to fluctuate. Also, as the high-frequency SL measurements were made at the upper limit of the equilibrium range, we were uncertain whether or not it was appropriate to treat α as a constant at high frequencies. To this end, we obtained plots of α for all of the SL data sets, where

$$\alpha = \frac{S_{measured}(\sigma)}{u^* g \sigma^{-4}}, \tag{2.57}$$

using the extreme values of u* for each SL data set.

If the theory held exactly, one would expect the data to adhere, roughly, to a horizontal line at a given level. Figure 2.7a provides a depiction of α for the SL measured frequency data obtained from a day of comparatively low friction velocities, u*~(0.082,0.112). In this particular plot, we have assumed the higher of the two friction velocities. For the lower range of frequencies included in the plot, α appears to be somewhat constant; at higher frequencies, α steadily decreases. Figure 2.7b is similar to Figure 2.7a, except it was obtained from a day of comparatively high friction velocities, u*~(0.288,0.375). Once again, we have assumed the higher friction velocity for the

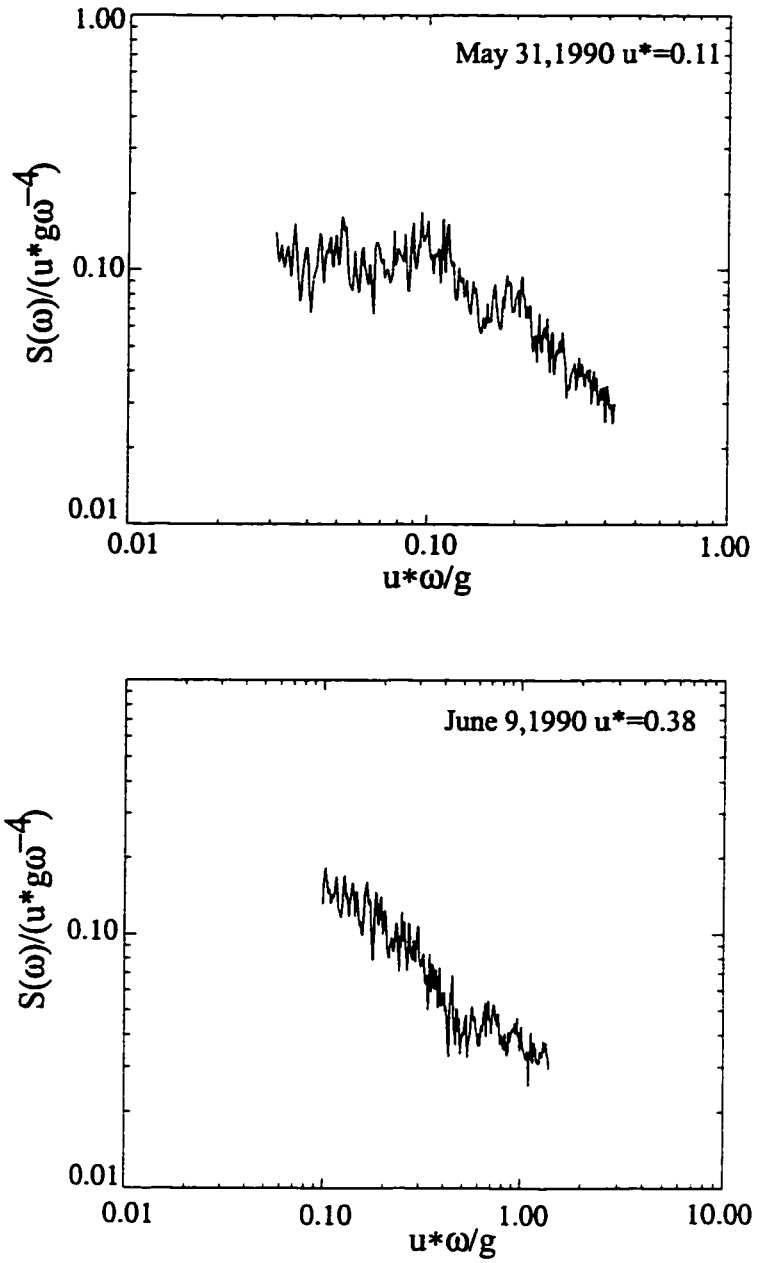

Figure 2.7: α Parameter for Standard Leopard Measurements; the upper panel depicts α for 31 May 1990. In this instance, we have assumed u*~0.11. The lower panel depicts α for 9 June 1990. In this instance, we have assumed u*~0.38. Both plots clearly indicate that the α parameter is not a constant.

measurement interval. In this case, it appears that α is consistently decreasing; first with a fairly steep slope and then more gradually at the higher frequencies. All of the SL data exhibited behavior similar to that depicted in these two figures. From these plots we concluded that, in fact, α is *not* constant over the range of frequencies measured in the SL experiment. We will encounter this conclusion again in the context of the u* retrievals presented in Chapter 4.

For a freely propagating gravity wave at the ocean surface, if the directionality is known, it is straight-forward to convert a measurement in frequency space to the corresponding quantity in the spatial domain, and vice versa, via the dispersion relationship. This relationship is only valid for gravity waves of low and intermediate frequencies in the absence of surface currents. Because they are *not* propagating on an undisturbed surface, high frequency gravity waves on the ocean surface experience a smearing out, or Doppler shifting, of their intrinsic frequencies due to the motion of the underlying waves on which they are riding. It was conceivable that the variability we observed in α was due to Doppler shifting effects.

For this reason, and also in order to obtain estimated wave number spectra from the measured SL frequency spectra, we wished to obtain a rough estimate of the magnitude of the Doppler shifting effects imparted to the high frequency waves from the underlying wave field. To do so, we used an approach suggested by Kitaigorodskii et al. (1975), which is summarized below. This served as the basis for a correction factor, which we applied to the high frequency spectra. Although effects such as wave blocking due to wave-current interactions could not be compensated for by this technique, it could nonetheless provide us with the basis for obtaining an estimate of SL frequency spectra from which the majority of Doppler shifting effects had been hopefully removed. We could then apply the dispersion relationship to these Doppler shift-corrected frequency spectra to obtain an estimate of the corresponding wave number spectrum.

A brief sketch of the approach of Kitaigorodskii et al. is provided here. For linear gravity waves in deep water where a current is present, it is necessary to modify the dispersion relation given in Equation 2.16 in the following fashion:

$$\sigma = \sigma(\mathbf{k}) = [(g + \bar{a})k]^{1/2} + \mathbf{k} \cdot \bar{\mathbf{v}}. \tag{2.48}$$

Here $\bar{a} = \frac{\partial^2 \bar{\zeta}}{\partial t^2}$ is the vertical acceleration of the large-scale waves of surface displacement $\bar{\zeta}$ and $\bar{\mathbf{v}}$ is the horizontal drift velocity of these long waves, all of which are slowly varying. Although $\bar{a}$ and $\bar{\mathbf{v}}$ are random variables, they are not independent because they are related through expressions for the large scale wave components, i.e. $\bar{a} = \bar{a}(\bar{\zeta})$ and $\bar{\mathbf{v}} = \bar{\mathbf{v}}(\bar{\zeta})$. If, however, we assume that the large scale waves have a narrow spectral width, we can express $\bar{a}$ and $\bar{\mathbf{v}}$ as:

$$\bar{a}(\bar{\zeta}) = -(\sigma^d)^2 \bar{\zeta} \tag{2.49a}$$

and

$$\bar{\mathbf{v}}(\bar{\zeta}) = \sigma^d \frac{\mathbf{k}^d}{k^d} \bar{\zeta}. \tag{2.49b}$$

where σ^d corresponds to the frequency of the slowly varying disturbance and k^d is the corresponding wave number, obtained via the usual dispersion relation. If we apply the expression for $\bar{\mathbf{v}}(\bar{\zeta})$ into (2.48) we can obtain a new dispersion relationship,

$$\sigma = \sigma(k, \nu) = [(g + \bar{a})k]^{1/2} + k\bar{W}\cos(\nu - \gamma^d) \tag{2.50}$$

where γ^d is the fixed angle between the propagation direction of the long-wave component of the surface waves and that of the mean wind, and $W=\sigma^d\bar{\zeta}$. Using a dispersion relationship of the form (2.50) requires a more general expression for the frequency-wave number transformation, namely,

$$S(\sigma)=\int_{-\pi}^{\pi}\left[\Psi(k,\nu)\frac{k}{G(k,\nu)}\right]_{k=k(\sigma,\nu)}d\nu. \qquad (2.51)$$

This provides the frequency spectrum $S(\sigma) = S(\sigma,\bar{a},\bar{v})$ corresponding to a fixed spatial spectrum, at fixed values of the random parameters $\bar{a}$ and $\bar{v}$. This is the appropriate type of spectral transformation to apply to short waves propagating on the surface of long waves. If we assume a spectral form for $S(\sigma)$ such as (2.46), it is possible to obtain an expression for the frequency spectrum that is consistent with (2.51), that will explicitly include the effects of Doppler shifting by the underlying waves. This expression is given by

$$S(\sigma) = \alpha u^* g\sigma^{-4}B(\sigma,\gamma^d), \qquad (2.52)$$

where $B(\sigma,\gamma^d)$ encompasses the effects of Doppler shifting by the long waves. One possible expression for $B(\sigma,\gamma^d)$ is given by

$$B(\sigma,\gamma^d)=1+\left\{1-3\tilde{p}\left(\frac{\sigma}{\sigma_d}\right)+\tilde{q}\left(\frac{\sigma}{\sigma_d}\right)^2\right\}\frac{(A^dk^d)^2}{2}, \qquad (2.53)$$

where A^dK^d is the long wave slope, estimated from the power spectral density for the long waves; σ is the nominal frequency and σ_d is the frequency associated with the spectral peak. The coefficients $\tilde{p}$ and $\tilde{q}$ depend on the directional distribution assumed for the long waves, which we have assumed is given by

$$\varphi(\upsilon) = (2/\pi)\cos^2\upsilon \qquad \text{for } |\upsilon| \in [0,\pi/2]. \qquad (2.54)$$

The associated coefficients are

$$\tilde{p} = 8/3\pi(\cos\gamma^d) \qquad (2.55a)$$

and

$$\tilde{q} = 1/2\cos^2\gamma^d + 1/4. \qquad (2.55b)$$

A detailed development of the term $B(\sigma,\gamma^d)$ from Equation (2.53) is provided in Kitaigorodskii et al. (1975).

We will assume that Equation (2.52) can be used to characterize the *measured* frequency spectrum, $S_{meas}(\sigma)$, which includes the effects of Doppler shifting by the underlying wave field. Using this expression, we can obtain an estimate for the frequency spectrum that compensates for the effects of Doppler shifting, namely

$$S_{corr}(\sigma)=S_{meas}(\sigma)\{1/B(\sigma,\gamma^d)\}. \qquad (2.56)$$

For each of the spectra measured in the SL experiment, we used Equation (2.56) to estimate the underlying, inherent frequency spectrum, $S_{corr}(\sigma)$. We subsequently transformed $S_{corr}(\sigma)$ to the appropriate wave number spectrum by the usual dispersion relationship.

In our analysis of Figures 2.7 a and b, we speculated that Doppler shifting of the high frequency waves was the source of the observed variability in α and that these effects had caused the spectrum not to conform to the theoretical behavior. Therefore, in Figure 2.8 a and b we examine plots of α for frequency spectra to which the Doppler shift correction described above had been applied. In this plot, the measured, uncorrected data are depicted with solid lines and the shift-compensated data are depicted with gray dashed lines. This plot suggests that only a slight amount of the observed variability in α appeared attributable to the Doppler shifting effects predicted by the approach of Kitaigorodskii et al.

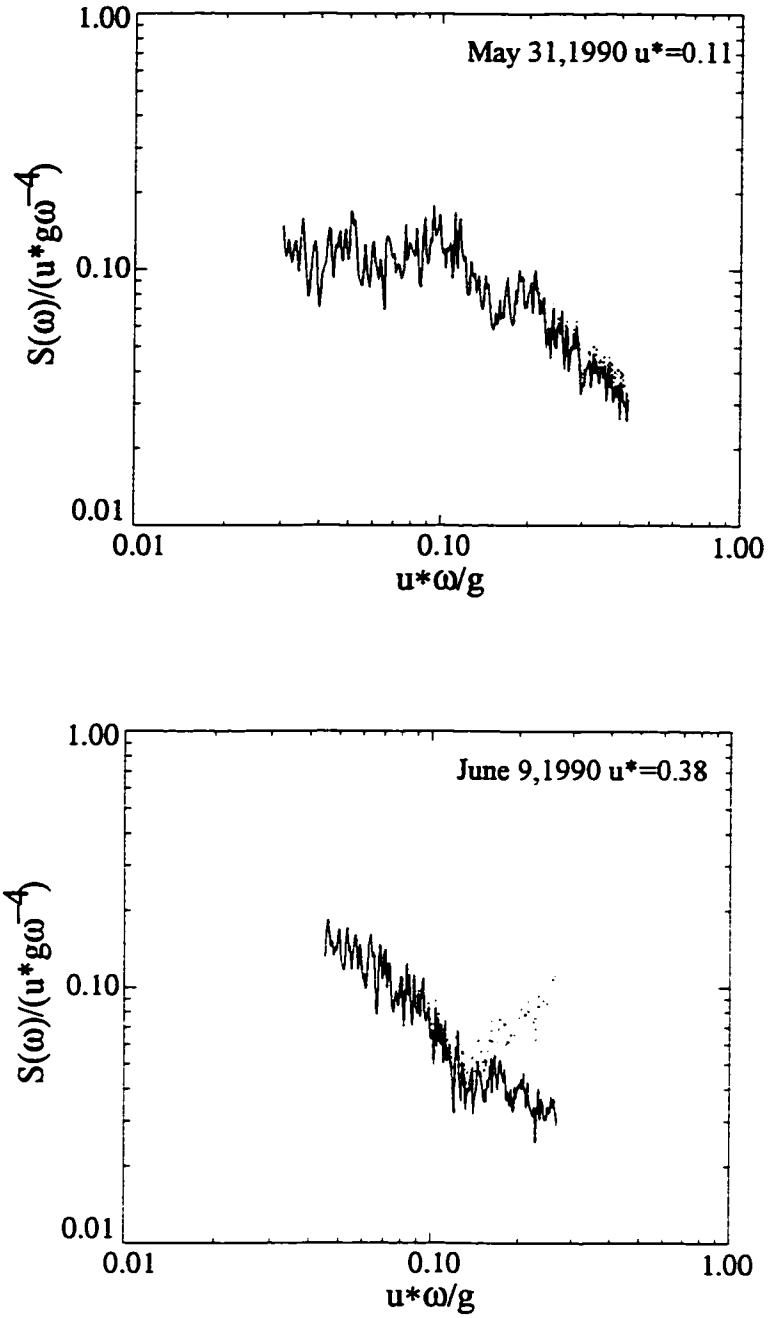

Figure 2.8: The α parameter is once again depicted for the Standard Leopard Measurements, as on the preceding page. Here, the dashed gray lines indicate the change in a resulting from the application of the Doppler shift correction described in Kitaigorodskii et al. (1975). The impact of the Doppler shift correction is appreciably greater for the high u* data.

Although this Doppler shift compensation factor would only compensate for some of the shifting effects experienced by the high frequency waves, this approach nonetheless presented the only means by which we hoped to have wave number spectra for the regime of interest. Therefore, the approach that we pursued was to obtain an estimate for the 'Doppler shift compensation' factor associated with each of the SL frequency spectra. Using this factor, we obtained corrected frequency spectra, which were, in turn, converted to wave number spectra using the standard dispersion relationship.

We compared the wave number spectra obtained from the 'shift compensated' frequency spectra with those obtained directly from the measured frequency spectra. The results of this comparison are presented in Figure 2.9 for two different SL data sets. These plots are consistent with a similar analysis presented by Banner et al. (1989) that examined the impact of Doppler shifting effects on spectral slopes. The solid line corresponds to the wave number spectrum obtained by applying the dispersion relation directly to a measured frequency spectrum. The dotted line corresponds to the wave number spectrum obtained by applying the dispersion relation to a frequency spectrum that had already been corrected for the effects of Doppler shifting. We observed the greatest difference between the two when u* was greatest.

We used the approach described above to obtain an estimate of the wave number spectrum corresponding to each of the SL frequency spectra. There is a linear relationship between the logarithm of the power spectral density and the logarithm of wave number in the equilibrium range. This relationship enabled us to obtain linear regressions between the suitably transformed variables, and to compare these results with Phillips' model. The results of these linear regression analyses are summarized in Table 2.3.

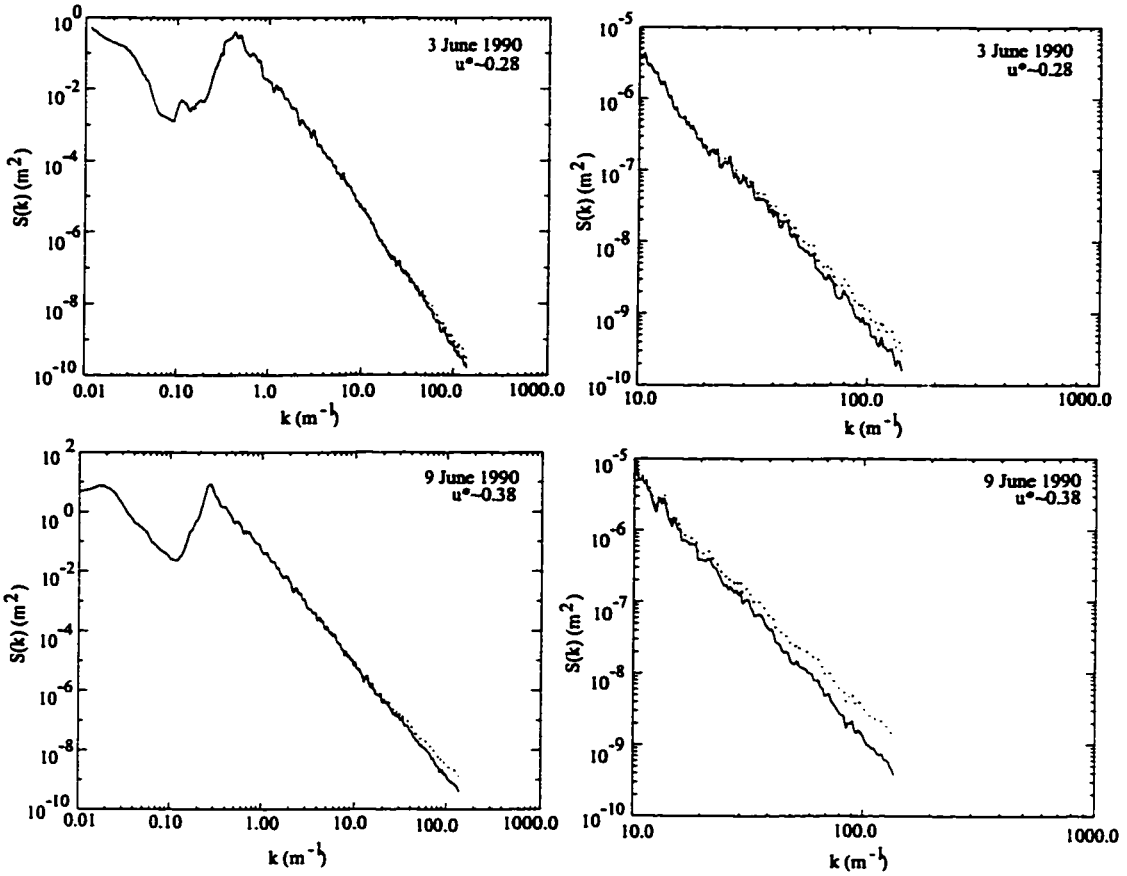

Figure 2.9: Comparison of wave number spectra that have been 'Doppler shift corrected' (dashed lines) with those that have not (solid lines) for two of the Standard Leopard data sets.

In this table it can be seen that the slope varied between –3.45 and –3.72. This suggests that the slope of the SL spectra fell between that consistent with the equilibrium model ($k^{-3.5}$) identified by Phillips (1985) and Kitaigorodskii (1983), and the saturation model (k^{-4}) predicted by Phillips' (1958) model as well as by Banner et al.(1989). We analyzed the data in Table 2.3 to determine whether or not the spectral slope exhibited any dependence on the environmental conditions, such as the friction velocity. In particular, we attempted to determine from these data, whether the spectral slope varied linearly with

friction velocity by fitting a linear model between the two variables. In fact, these analyses suggested the SL measured spectra were statistically consistent with the equilibrium spectral form. That is, the slope was not significantly different from –3.5 for these data, consistent with Phillips' equilibrium spectral model. This result, obtained on the open ocean, is in agreement with the results obtained in wave tanks of Jahne and Riemer (1990) and Klinke and Jahne (1992), which both observed the wave number spectrum to behave in accordance with Phillips' $k^{-3.5}$ spectral form, for waves between 3 and 24 cm.

Although the Doppler shift correction discussed above compensates for some of the effects imparted to the small-scale waves by the underlying wave field, it does not compensate for all such effects. This is because the Doppler shift compensation technique requires that we make several simplifying assumptions. In addition, it does not take into account several important effects, such as wave-current interactions. Nonetheless, the SL spectra serve as corroborating evidence that it is, indeed, appropriate to use the Phillips equilibrium spectral model for the ocean waves that serve as ERS-1 Bragg scatterers.

Date	u *	constant	std dev	slope	std dev
31-May	0.08 - 0.11	-4.19	0.028	-3.72	0.01
3-Jun	0.20 - 0.29	-3.95	0.03	-3.67	0.01
3-Jun	0.20 - 0.29	-3.81	0.029	-3.68	0.011
4-Jun	0.09 - 0.12	-4.22	0.032	-3.45	0.012
5-Jun	0.12 - 0.15	-4.05	0.031	-3.57	0.011
7-Jun	0.21 - 0.33	-3.17	0.039	-3.5	0.014
9-Jun	0.29 - 0.38	-3.11	0.031	-3.65	0.011

Table 2.3: Summary of SL regression analyses regarding spectral slope at high wave numbers.

We have now identified the components that comprise the spectral model used in our friction velocity retrieval scheme: at low wave numbers we use NDBC buoy measurements; in the mid- and high- wave number regimes, we use the equilibrium spectral model of Phillips (1985). We now turn our attention to how these components are combined into one spectral representation. The spectral model and the buoy measurements must be joined at some point. It was necessary for us to determine where this join point should be located and how the two components should be spliced together. This was equivalent to determining a wave number below which the ASM would be given by buoy data, and above which it would use the equilibrium model.

In Phillips (1985), the lower limit of the equilibrium range is defined as 'wave numbers that are large compared with those of the spectral peak'. Other authors, e.g. Juszko (1995), have attempted to set specific upper and lower limits to this regime, but ultimately our decision regarding the lower limit of the equilibrium range was governed by the desire to use as much of the buoy data as possible. The buoy measurements typically extend to well above the spectral peak, so we decided to locate the first join point immediately above the highest buoy measurement ($k = 0.49$).

Given this location for the join point, we needed to determine how to match the two spectra at this point. One approach to matching sought continuity in the combined spectrum but without giving undue influence to the highest buoy measurement. Given that measurement noise increases with frequency (Shumway, 1986), it would be best to use an average value for the parameter, α, at this join point. We fit the equilibrium model to the ten highest frequency buoy observations, and averaged the result. This approach to matching assumes that the spectra are relatively linear in this region, which is justified on the basis of Figure 2.2a for the buoy data and Figure 2.6 for the SL data. That is, this relationship is given by

$$\alpha_i = S(k_i)/(u^* g^{-1/2} k_i^{-3.5}) \tag{2.61}$$

where $S(k_i)$ denotes the buoy-derived estimate of the power spectral density for a given wave number k; therefore, $\overline{\alpha}$ is given as

$$\overline{\alpha} = \frac{g^{1/2}}{u^*} \sum_{k(i)=k\,\max-9}^{k\,\max} S(k_i) k(i)^{3.5}. \tag{2.62}$$

Clearly, the choice of α determined at the join point has significant influence on the modeled portion of the spectrum. It was desirable, therefore, to characterize the variability of α, at least in some cursory fashion. To do so, we examined the mean and standard deviation of the α parameter for the five, highest-frequency buoy measurements at two different buoy locations and as a function of the environmental conditions. One buoy included in this investigation was located off Norfolk, VA and the other was located in Yaquina Bay, OR. These buoys are depicted in Figures (2a) and (2b), respectively. These particular buoys and time intervals were selected for study as they corresponded to the times and locations where we intended to apply our preliminary friction velocity retrievals.

The ten instances included in Table 2.4 will be investigated in greater detail in Chapters 3 and 4; they correspond to near-simultaneous buoy measurements and ERS-1 scatterometer measurements. These results suggest that α varies appreciably with environmental conditions at a single location. It also varies somewhat between the two buoy sites. From this limited investigation we made the following observations:

(1) α has significant influence over how spectral levels are set in general, and in the Bragg scattering regime in particular. This may cause us some problems in our analyses, given that the maximum wave number measured by the buoy is around 0.5 (m^{-1}) and the ERS-1 Bragg wave number is around 200 (m^{-1}). It seems likely that waves in these two regimes will exhibit appreciably different behavior.

(2) α appears to exhibit considerable variability both as a function of location and as a function of environmental conditions.

(3) In our analysis of the SL data, we observed that at high wave numbers, α appears to consistently decrease.

YAQUINA OR			
	u *	alpha avg.	alpha s.d.
	0.11	0.088	0.018
	0.28	0.072	0.017
	0.27	0.063	0.014
	0.45	0.069	0.016
	0.24	0.078	0.011
NORFOLK VA			
	u *	alpha avg.	alpha s.d.
	0.39	0.047	0.009
	0.16	0.051	0.014
	0.51	0.068	0.018
	0.24	0.045	0.017
	0.37	0.032	0.006

Table 2.4: Summary of α parameter mean and variance for NDBC buoy 46050 (Yaquina Bay, OR) and NDBC buoy 44014 (Norfolk, VA).

Given all of these issues, it was clear that it would be difficult to justify using the buoy-based α for the entire modeled portion of the spectrum. However, we would need some additional information, preferably derived directly from measurements of the high wave

number regime, to help us determine the best choice for α at wave numbers well above the upper limit of the buoy measurements. In Chapter 4 we will use the friction velocity retrieval scheme developed in this research effort as a tool for determining a preliminary basis for how to set the α parameter at high wave numbers.

In summary, the ASM is a spectral model that is appropriate for characterizing ocean wave spectrum for wave numbers ranging over five orders of magnitude. The low wave number regime is given by spectral estimates obtained from NDBC buoy measurements; the middle and high wave numbers are characterized by Phillips' equilibrium spectral model. Our decision to use this form was based on the analyses of the SL data from the open ocean discussed in this section as well as the findings of Jahne and colleagues. The α parameter for the mid range model will be determined by matching with the buoy measurements. For the high wave number regime, our choice for α will be based on the high wave number spectral information contained in the ERS-1 scatterometer measurements. For this reason, we defer presenting an exact model form, with respect to the choice of the α for the high wave numbers, until Chapter 4 where we will investigate these issues more closely using our friction velocity retrieval scheme.

2.7 2-D SPECTRAL PROPERTIES: SPREADING FUNCTIONS

Thus far, one-dimensional models for power spectral density have been the focus of this research. Time series measurements of the displacement of the ocean surface made at a single point, such as those obtained by a spar buoy or a wave staff can be comparatively straightforward to obtain and to analyze. Measuring the two-dimensional wave number spectrum on the open ocean, particularly at high wave numbers, has proven

to be a daunting task and remains an ongoing area of oceanographic research. To obtain predictions of radar backscatter from the ocean surface, however, requires that we specify the two-dimensional wave number spectrum.

In Section 2.4, we discussed two techniques for obtaining estimates of the two-dimensional spectrum from NDBC buoy measurements. Both of these approaches assume that it is possible to decompose the two-dimensional spectrum into a function of wave number, and a function of direction, i.e.

$$S(k,\theta)=(1/k)E(k)D(k,\theta), \tag{2.74}$$

where it is assumed that

$$D(k,\theta)=\int_0^{2\pi} kD(k,\theta)d\theta = 1. \tag{2.75}$$

Typically, $D(k,\theta)$ is referred to as the directional spreading function, and it provides a normalized description of the directional distribution of the ocean wave energy.

In this section we will begin with a discussion of two experiments from the mid-to late- 1980s that resulted in estimates of the directional spreading function: Donelan et al. (1985) and Banner et al.(1989). At the end of this section we will describe two recent attempts at modeling the directional spreading function: Elfouhaily et al. (1997) and Caudal and Hauser (1996).

Donelan et al. deployed an array of 14 capacitance wave staffs from a tower at the western end of Lake Ontario as part of a field experiment intended to measure the directional spectrum of wind-generated waves between 2 and 28 m. A new form for the frequency spectrum was developed from these measurements as well as an expression for the directional spreading of these waves. The model form for the spreading function is given as follows:

$$F(\sigma,\theta) = \frac{1}{2}\Phi(\sigma)\beta \sec h^2 \beta\{\theta - \bar{\theta}(\sigma)\} \tag{2.76}$$

where $\bar{\theta}$ is the mean wave direction and

$$\beta = 2.61(\sigma/\sigma_p)^{+1.3} \quad 0.56 < (\sigma/\sigma_p) < 0.95 \tag{2.77a}$$

$$\beta = 2.28(\sigma/\sigma_p)^{-1.3} \quad 0.95 < (\sigma/\sigma_p) < 1.6 \tag{2.77b}$$

$$\beta = 1.24 \quad \text{otherwise.} \tag{2.77c}$$

An extended form of this one-dimensional spectrum and spreading function, expressed in terms of wave number was applied with some success in the backscatter prediction efforts of Donelan and Pierson (1987).

Banner et al. made a series of spatial measurements in Bass Strait of waves between 0.2 and 1.6 m. These data were the basis for the one-dimensional spectral form of Banner et al. (1989) presented in Section 2.5. In addition, Banner (1990) derived a directional spreading function from these data. This spreading function was found to be consistent with a wave number form of the model developed by Donelan et al., and served to extrapolate their model to higher wave numbers. The model form presented in Banner (1990) is, in fact, an aggregation of these two models. Specifically, he proposes a spreading function of the form

$$D(k,\theta) = \text{sech}^2 b(\theta - \theta_{max}) \tag{2.78}$$

where θ_{max} is the direction of the dominant wind waves at the spectral peak, and

$$b = 2.28(k/k_p)^{-0.65} \quad \text{for } 0.97<(k/k_p)<2.56 \tag{2.79a}$$

$$b = 10^{-0.4+0.839\exp[-0.567\ln(k/k_p)]} \quad \text{for } k/k_p>2.56. \tag{2.79b}$$

This form for the directional spreading function is not normalized to integrate over direction

to yield unity; instead, it is constrained via a total energy requirement. The spreading function and associated constraint are given by

$$D(\theta,k)=\Psi(k,\theta)/\Psi(k,\theta_{max}) \tag{2.80}$$

and

$$\int_{-\pi}^{\pi}\int_{0}^{\infty}\Psi(k,\theta_{max})D(\theta,k)kdkd\theta = \overline{\xi^2}\,. \tag{2.81}$$

We sought a form of the directional spreading function to use in the ASM that had a physical basis, and was derived from measurements made on the open ocean. The directional spreading functions developed by Donelan and Banner are largely consistent with these goals.

Banner, as well as other researchers, e.g. Fung and Lee (1982), observed that the directional distribution of waves on the order of 0.1 - 1.0 m is quite broad. At smaller wavelengths (higher wave numbers) many observations suggest that the directional distribution narrows once again. This has been supported by measurements of two-dimensional wave spectra acquired in wave tanks by Jahne and Riemer (1992) and by Hara (1994), and by measurements of Shemdin et al. (1988) from the open ocean. This narrowing phenomenon has also been observed consistently in microwave measurements made on the open ocean.

To augment the Donelan-Banner spreading function, we needed additional data or models to characterize the directional spreading of waves in the ERS-1 Bragg regime. Ideally, we hoped to find two-dimensional spectral measurements from the open ocean at this scale from which we could derive a spreading function. We were able to identify data sets appropriate for addressing this issue, e.g. Hwang et al. (1995, 1996) and Donelan et al. (1996). There was insufficient time for us to derive a directional spreading model from these data but it is hoped that we can investigate these data sets in the context of this problem in future research.

Two recent papers by Elfouhaily et al. and by Caudal and Hauser suggest forms for the directional spreading function that apply to high wave numbers. Elfouhaily et al. propose an additional term, Δ, that can be applied to existing models. This term is essentially a ratio of the upwind and the crosswind mean squared slopes, which are derived largely from the measurements of Cox and Munk (1954). They apply this term in the form of a constraint to the spreading functions of Longuet-Higgins et al. (1963), Mitsuyasu et al. (1975), Donelan et al. (1985), Banner (1990) and Apel (1994). The authors note that their approach has problems at high wave numbers. In addition, their high wave number directional spreading function relies heavily on data obtained from wave tanks.

The model form of Caudal and Hauser is also a high wave number extrapolation that can also be applied to the models of Apel and Banner. As with Elfouhaily et al., this approach entails the application of a correction term to an existing spreading function. This correcting term vanishes for low wave numbers; 'at high wave numbers the correcting term is constrained by multifrequency microwave observations of the normalized radar cross section σ^0 from P band (frequency = 0.43 Ghz) up to Ka band (frequency = 34.43 Ghz) together with optical observations of the sea surface slope variance' (Caudal and Hauser, 1996).

Several data sets were combined in the development of this form: The first was a series of measurements made by the airborne Delft University of Technology Scatterometer (DUTSCAT) at six frequencies including C-band (5.3 Ghz). These measurements were made over the Atlantic Ocean near the coast of France in 1987. In addition, Caudal and Hauser obtained a set of X and Ka band measurements of the ocean surface that were described in Masuko et al. (1986). Measurements obtained from the RESSAC C-band radar, described in Hauser et al. (1992) were also included, as were a series of measurements from several campaigns at various frequencies, which were compiled by

Jones and Schroeder (Jones and Schroeder, 1978). Finally, the authors made use of the optical measurements of slope variance of Cox and Munk (1954).

Using all of the above sources, Caudal and Hauser (CH) arrived at a combined data set consisting of 244 observations. These data served as the input to their model inversion process, the result of which was a modified form for the directional spreading functions of Banner (1990) and Apel (1994). We will only describe the application to Banner's model, which is what was implemented in the ASM.

The CH correction term consists of an alternative expression for Equation (2.79a) and (2.79b). Specifically, $b=b_0(k)$ is replaced by

$$b=b_0(k) + \delta \tag{2.82}$$

where δ is given by

$$\delta = 10^{(p_1X^2+p_2X+p3)}. \tag{2.83a}$$

where

$$X = \log_{10}(k). \tag{2.83b}$$

The coefficients were obtained by fitting the above model to the remote measurements, and are given by

$$p_1=-0.177 \qquad p_2=1.11 \qquad p_3=-2.00, \tag{2.84}$$

with an RMS error of 1.40 dB. Although this expression was based on remote rather than *in situ* measurements of the ocean surface, it nonetheless provided us with a means for characterizing the directional spreading function at high wave numbers. Figure 2.18 illustrates the chief differences between the spreading functions of Banner (1990) and of Caudal and Hauser (1996). In addition to providing a comparison of the two parameters b

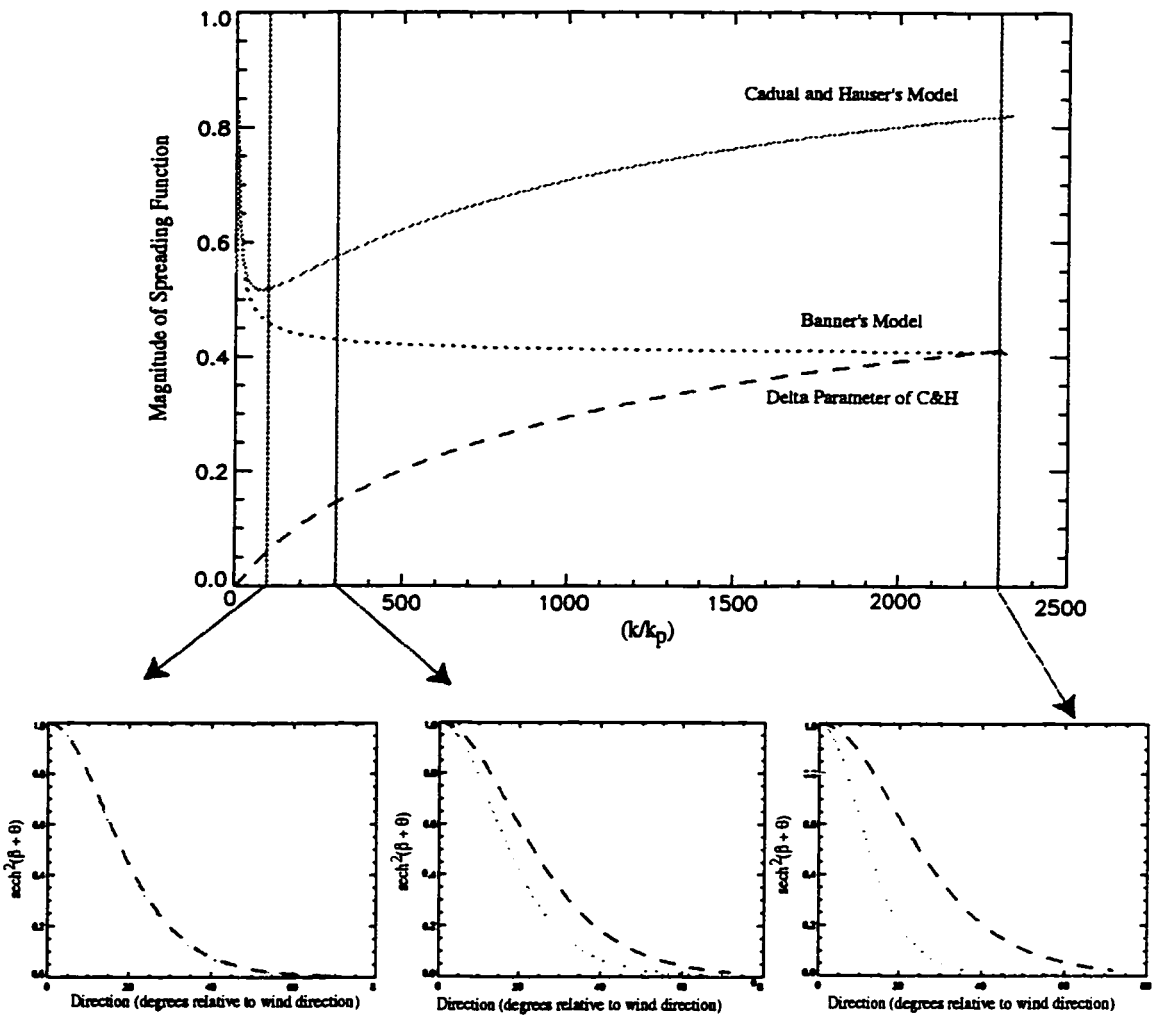

Figure 2.18: A comparison of the spreading functions of Banner and Caudal and Hauser. The upper panel illustrates the magnitude of the directional spreading function as a function of wave number (relative to the spectral peak). The lower panels illustrate the difference between the two for low, mid and high wave numbers. The spreading function of Caudal and Hauser narrows at high wave numbers, consistent with observations.

and b_0, it also illustrates the difference in the associated spreading functions for three different wave number regimes.

It was necessary to implement a modified form of this combined spreading function, which was normalized to integrate to unity. This was necessary to ensure consistency with the spreading functions estimated from the NDBC buoy measurements.

An example of this normalized form of the Donelan-Banner-Caudal/Hauser (DBCH) directional spreading function is illustrated in Figure 2.19.

In the vicinity of the transition between the NDBC data and the model we defined a linear weighting function so that the two could be smoothly merged. Specifically, the spreading function applied to the eight highest buoy measurements was a blend between buoy observations, Equations (2.78) and (2.79) and Equations (2.82) – (2.84). At k_{max-8}, this blend included a 10% contribution from the DBCH form and a 90% contribution from the NDBC buoy-based estimate. At k_{max-5} the blend is takes an equal contribution from each. Finally, k_{max} employs a 90 % contribution from the DBCH form, and only a 10% contribution from the buoy-derived spreading function.

Finally, it is worthwhile mentioning another approach of relevance to wind stress retrieval efforts such as this one. All of the directional spreading functions discussed above are concerned with the distribution of waves relative to the *wind* direction. The ASM, however, is intended for retrieving friction velocity from scatterometer data. In the introduction to this chapter, we mentioned that the wind vector and the friction velocity vector are not necessarily aligned. Several recent experiments have investigated this relationship, e.g. Reider and Smith (1994) and (1998), Geernaert (1988). A spreading function applicable to high wave numbers that related the directional distribution of waves to the *stress* direction would be an important and interesting extension of this research.

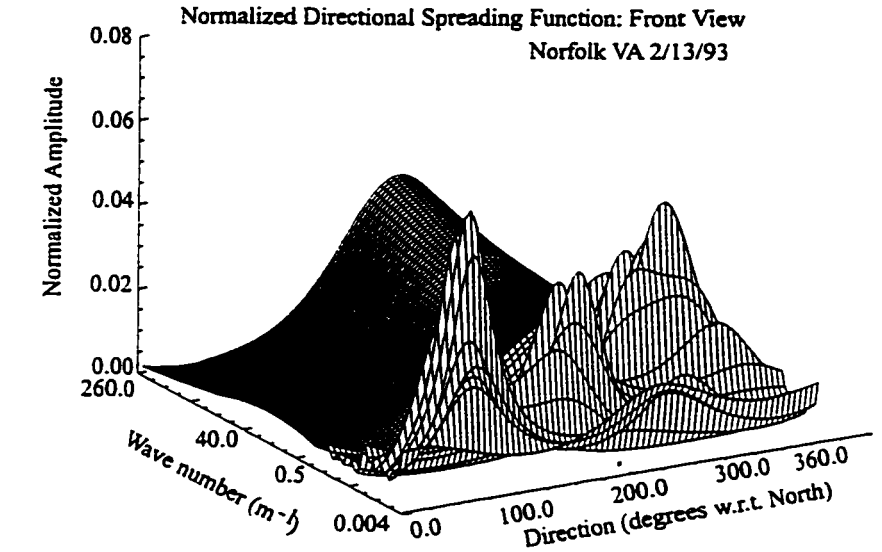

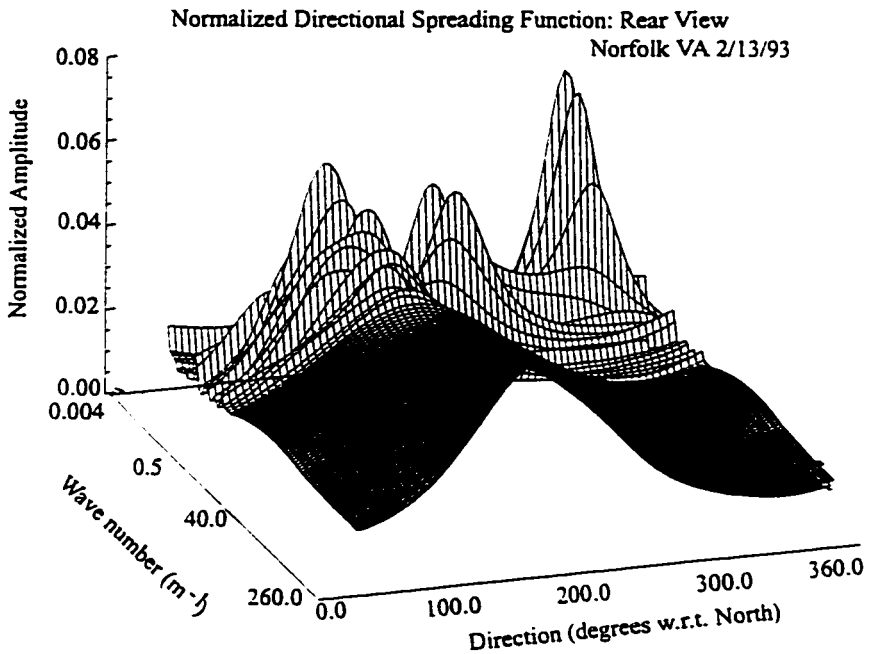

Figure 2.11: Example of the normalized form of the DBCH spreading function implemented in this research. This example is for 2/13/93 in Norfolk, VA where the wind direction is 220° and the friction velocity is 0.24 m/sec.

2.8 SUMMARY OF SPECTRAL MODEL

In this chapter, we have presented the preliminary components of the spectral form used in this research. These components consist of the following:

(1) The directional wave number spectrum for the low wave number regime of the spectrum, $0.004\ m^{-1} < k < 0.49\ m^{-1}$, is derived from application of the maximum likelihood technique for spectral reconstruction due to Oltman-Shay and Guza (1984) using measurements obtained buoys within the NDBC network.

(2) The one-dimensional wave number spectra for the mid- and high- wave number regimes of the spectrum, $0.5\ m^{-1} < k < 39.0\ m^{-1}$, and $40.0\ m^{-1} < k < 260.0\ m^{-1}$, respectively, are both given by the equilibrium spectrum model due to Phillips (1985). This model is given by:

$$S(k) = \alpha u^* g^{-1/2} k^{-3.5}, \tag{2.45}$$

Where u^* denotes the friction velocity (in m/s), k denotes wave number (in m^{-1}), g is gravity, α is a dimensionless constant determined by spectral levels. At the transition between the buoy measurements and the spectral model, α is set by matching Phillips' model with the buoy measurements in one dimension. Our choice of this model form for the mid-range of wave numbers was supported by several data sets discussed earlier. Our analysis of the Standard Leopard spar buoy measurements, presented in Section 2.6, supported use of Phillips' model for high wave numbers as well. This was also supported by analyses of detailed measurements made in several different wave tank experiments by Jahne and colleagues. A source of uncertainty, however, was how to determine the best

choice for the α parameter to apply to the model for the high wave number regime. This issue is discussed in Chapter 4.

(3) The two-dimensional wave number spectrum for the mid- and high- wave number regimes is obtained via a model of the directional spreading of wave energy relative to the wind direction. This model is, in fact, a combination of models developed by three different groups of researchers: Donelan et al. (1985), Banner (1990) and Caudal and Hauser (1996). The model of Donelan et al. (1985) was developed from in situ wave staff measurements. The model of Banner (1990) was developed from analysis of stereophotographs of the ocean surface. Caudal and Hauser (1996) developed their model form from analyzing numerous remote measurements of the sea surface spanning a broad range of electromagnetic wavelengths.

The Aggregate Spectral Model is applied in the following chapters to obtain predictions of radar backscatter, which in turn, are used in our technique for retrieving estimates of the wind stress vectors at the ocean surface from ERS-1 scatterometer measurements.

CHAPTER 3: RADAR CROSS SECTION PREDICTION

3.1 INTRODUCTION

The first of the three components that comprise our scheme for retrieving friction velocity from scatterometer measurements (see Figure 1.5), an ocean spectral model, was presented in the preceding chapter. This model estimates the spatial distribution of wave energy at the ocean surface attributable to a specified wind forcing. The second essential component of our scheme, which we present in this chapter, is an electromagnetic scattering model. This model is used to predict the normalized radar cross section that a radar system would measure if it interrogated a rough surface, such as the output of the ocean spectral model described in Chapter 2.

In this research, we are interested in predicting the radar backscatter that would be measured by the ERS-1 scatterometer. A scatterometer is a radar that transmits microwave energy towards a surface. Part of this energy is absorbed and part of it is scattered in various directions, depending on the properties of the surface. The proportion of energy scattered back towards the origin of the energy, or backscatter, is measured by the scatterometer and serves as the basis for characterizing the properties of the surface. This can be expressed mathematically by the radar equation. A clear, physical development of the radar equation is provided in Ulaby, Moore and Fung (1986). A brief summary of it is provided here as well.

The primary quantity of the radar equation is P_r, the backscattered power received from a given surface. It can be expressed as

$$P_r = \left(\frac{P_t G_t A_e}{(4\pi)^2 R^4} \right) \sigma. \tag{3.1}$$

The first term on the right hand side of Equation (3.1) characterizes the radar system: A_e is the effective area of the receiving antenna, $P_t G_t$ is the power per unit angle transmitted in the direction of the scatterer and $(1/(4\pi)^2 R^4)$ is a two-way spreading loss based on the range, R, from the target. The second term in the radar equation is referred to as radar cross section and is denoted by the parameter σ. It characterizes the scattering properties of the target, i.e. scattering object or surface. Here we are neglecting atmospheric attenuation, which is usually negligible for microwaves in the absence of heavy rain.

Scattering from natural surfaces like the ocean is characterized using a cross section that is normalized by area denoted σ^0. This characterizes the proportion of energy scattered from a unit area on the ocean surface relative to the energy that was incident on it. Using this normalized form of radar cross section, the variable σ, in equation (3.1) can be expressed as

$$\sigma = A_{ill} \sigma^0 \tag{3.2}$$

where A_{ill} denotes the area illuminated by the radar. Here we assume that the transmitting and the receiving antennas are the same antenna or view the same ocean area.

Radar backscattering from the ocean is difficult to model because the surface is complicated and irregular, and is not amenable to simple mathematical description. In addition, this complicated surface is evolving both in space and in time. To describe, much less to solve the appropriate boundary value problems requires several simplifying assumptions and/or the application of numerical methods. The primary aim of this chapter

is to briefly present a set of approximate techniques, referred to as composite surface theory, that are used for predicting radar backscatter from a rough surface, such as the ocean. In composite surface theory, the ocean surface is partitioned into two scattering regimes: one where the primary scattering mechanism is attributable to the small-scale ocean waves of the order of the radar wavelength and the other where the primary scattering is from the larger scale, gently-undulating waves. The scattered signal predicted from the short waves must be modified to include the effects of tilting and modulation by the underlying, long waves. The scattering from both regimes are combined to predict the overall scattering from the ocean surface. This is also referred to as a two-scale model (Valenzuela, 1978).

In this chapter we provide a brief overview of the theory of electromagnetic scattering from a rough surface, particularly at microwave frequencies. We describe the composite surface scattering model and some of its approximations and limitations. In addition, we mention some recent innovations relevant to predicting the normalized radar cross section of the ocean surface. In this chapter we implement our friction velocity retrieval technique as part of an investigation regarding the impact of long wave effects on radar cross section prediction. In addition, we provide an example that illustrates an application of the two primary components of our scheme for retrieval of friction velocity and direction at the ocean surface from ERS-1 scatterometer measurements. This example enables us to see how the radar cross section predictions vary as a function of the ocean spectral model inputs and sets the stage for the cost function analyses presented in Chapter 4.

3.2 THEORETICAL BACKGROUND

Maxwell's equations specify the fundamental relationships between electric and magnetic fields. If we use rationalized mks units, and take both the electric field, **E**, and magnetic field, **H**, to be time-harmonic, so that the time dependence can be expressed as $e^{-i\omega t}$, it is possible to write:

$$\nabla \times \mathbf{E} = i\omega\mu\mathbf{H} \tag{3.3}$$

$$\nabla \times \mathbf{H} = -i\omega\hat{\varepsilon}\mathbf{E} \tag{3.4}$$

$$\nabla \cdot \mathbf{E} = \rho / \varepsilon \tag{3.5}$$

$$\nabla \cdot \mathbf{H} = 0 \tag{3.6}$$

In these expressions, the complex dielectric constant is given by $\hat{\varepsilon} = \varepsilon + i\sigma/\omega$, where σ is the conductivity, ρ is the charge density and ω is the radian frequency. The permittivity ε and the permeability μ characterize the constitutive properties of the medium. In free space, $\varepsilon=\varepsilon_0=8.854\times10^{-12}$ Farads/meter and $\mu=\mu_0=4\pi\times10^{-7}$ Henry/meter. In the absence of charge, $\nabla \cdot \mathbf{E} = 0$.

An expression for the homogeneous wave equation can be obtained by combining (3.3) and (3.4). If the medium of interest is source-free, the **E** field can be expressed as

$$\nabla^2\mathbf{E} + \omega^2\mu\varepsilon\mathbf{E} = 0 . \tag{3.7}$$

A solution to this equation can be given by

$$\mathbf{E}(\mathbf{r},t)= E_0 \hat{\mathbf{e}}_i \exp(i\mathbf{k}_i \cdot \mathbf{r}), \qquad (3.8)$$

where $\mathbf{r}$ is defined as $r = (x\hat{\mathbf{x}} + y\hat{\mathbf{y}} + z\hat{\mathbf{z}})$ and $\hat{\mathbf{x}}$, $\hat{\mathbf{y}}$ and $\hat{\mathbf{z}}$ are unit displacement vectors. The wave amplitude is given by E_0 and $\hat{\mathbf{e}}_i$ characterizes the polarization state of the wave, indicating the direction in which the vector points. We will define the plane of incidence to be that formed by $\mathbf{k}_i$ and the normal to the surface. We assume the convention that if $\mathbf{E}$ is perpendicular to the plane of incidence a wave is called 'horizontally polarized' and is denoted by the subscript h; when $\mathbf{E}$ is in the plane of incidence it is called 'vertically polarized', and is denoted by the subscript v (Brown, 1990). The ERS-1 scatterometer transmits and receives only vertically polarized energy so we will generally restrict consideration to this case. In Equation (3.8), $\mathbf{k}_i = k_0 \hat{\mathbf{k}}_i$ where k_0 is the wave number of the medium in which the wave is propagating ($k_0 = \omega\sqrt{\mu_0 \varepsilon_0}$) and $\hat{\mathbf{k}}_i$ gives the direction of propagation. From Maxwell's equations, a similar expression can be obtained for $\mathbf{H}(\mathbf{r},t)$. $\mathbf{E}$, $\mathbf{H}$ and $\mathbf{k}_i$ define a mutually orthogonal coordinate system for describing the propagation of an electromagnetic wave through a medium.

As we are concerned with radar echoes in this research, it is important to consider wave reflection. Figure 3.1 provides an illustration of an electromagnetic plane wave, incident with angle θ_i at a planar interface between two media. At the interface, the incident wave will be reflected back into the upper medium as well as transmitted into the medium below. We can obtain expressions for the total fields both above and below the interface using the boundary conditions. If we specify the wave number for the lower medium by $k_1 = \omega\sqrt{\mu_1 \varepsilon_1}$, the transmitted and reflected waves can be expressed as $\mathbf{E}_r = E_{r0} \hat{\mathbf{e}}_r \exp(i\mathbf{k}_r \cdot \mathbf{r})$ and $\mathbf{E}_t = E_{t0} \hat{\mathbf{e}}_t \exp(i\mathbf{k}_t \cdot \mathbf{r})$, where the subscripts r and t are used to denote the reflected and transmitted quantities, respectively.

The tangential components of the $\mathbf{E}$ and the $\mathbf{H}$ fields must match on both sides of the boundary, and Snell's law, requiring matching of phases on both sides of the interface,

must be satisfied. These relationships enable us to define the Fresnel reflection coefficients, which relate the reflected and transmitted fields to the incident field, given the constitutive properties of the two media. Specifically,

$$R_V = \frac{\mu_0 k_1^2 \cos\theta_i - \mu_1 k_0 \sqrt{k_1^2 - k_0^2 \sin^2\theta_i}}{\mu_0 k_1^2 \cos\theta_i + \mu_1 k_0 \sqrt{k_1^2 - k_0^2 \sin^2\theta_i}} \tag{3.9}$$

and

$$R_H = \frac{\mu_1 k_0 \cos\theta_i - \mu_0 \sqrt{k_1^2 - k_0^2 \sin^2\theta_i}}{\mu_1 k_0 \cos\theta_i + \mu_0 \sqrt{k_1^2 - k_0^2 \sin^2\theta_i}}, \tag{3.10}$$

where R_H specifies the relationship between the reflected and the incident electric field, and R_V specifies the relationship governing the incident and reflected magnetic fields. For normal incidence, $R_H=R_V$. The transmission coefficients can be obtained using $T_V=1+R_V$ and $T_H=1+R_H$.

To get predictions of the reflected and transmitted fields when the interface between the upper and lower media is no longer planar, such as the air-sea interface, it is necessary to pursue a more general approach.

The Stratton-Chu Equation

J.A. Stratton (Stratton, 1941) and L.J. Chu developed a technique for predicting the scattered fields from an irregular surface which can be used when the simple laws of reflection no longer apply. The Stratton-Chu formulation enables one to represent the E and the H fields at a given point within a volume in terms of the electromagnetic fields present on a closed surface surrounding the point. We assume that all sources are outside of the volume of interest, although Stratton (1941) presents a development of these expressions that allows for inclusion of sources within the volume.

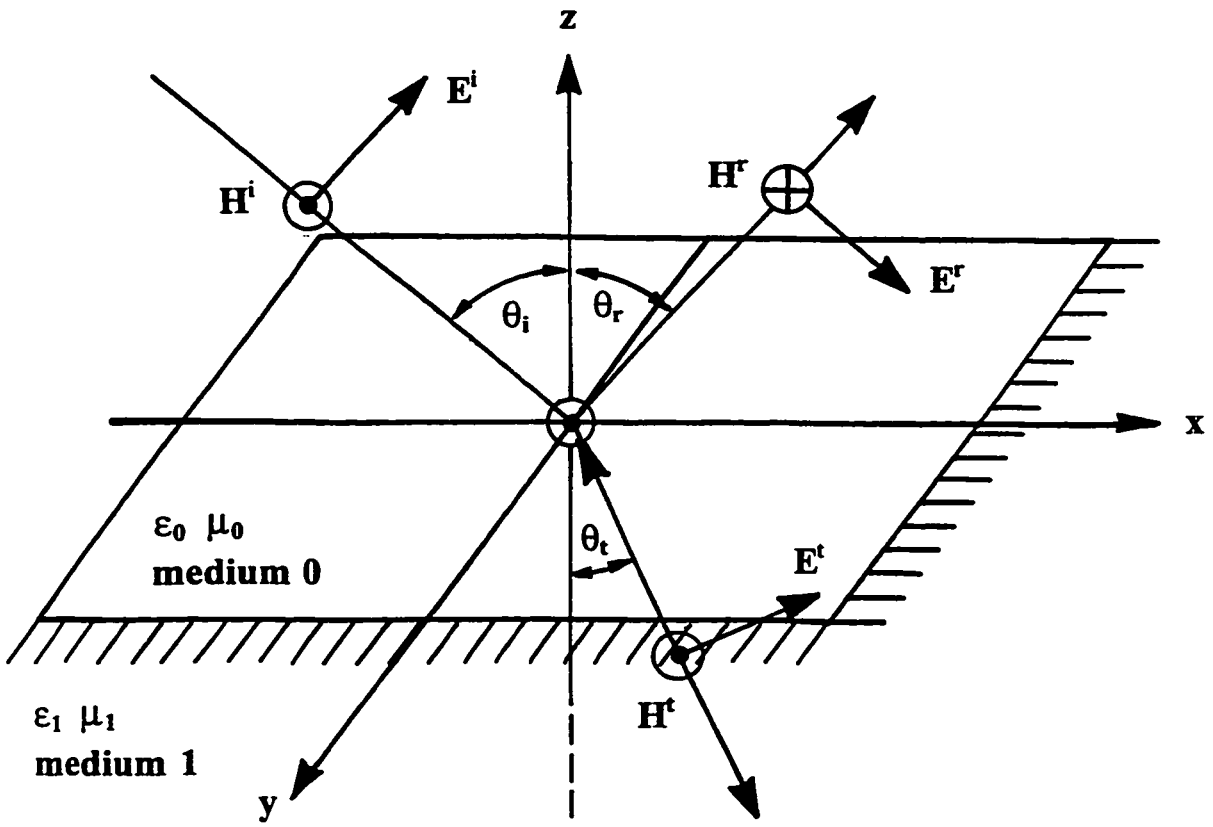

Figure 3.1: Illustration of an electromagnetic wave incident upon a planar interface. The upper medium has permittivity ε_1 and permeability μ_1; the lower medium has ε_2 and μ_2. The wave in the illustration is vertically polarized. From Brown (1990) and Balanis (1987).

Figure 3.2 illustrates the relationship between the relevant variables in this analysis. We let S be an arbitrary closed surface and let $\bar{r}$ be a point of observation inside S; S_γ is a sphere of small radius γ centered on $\bar{r}$, and V is the volume bounded internally by S_γ and externally by S. In addition, we take $\hat{n}$ to be a unit vector normal to S and to S_γ that is directed out of V. We apply Green's second identity, the divergence theorem as well as several additional vector identities to obtain the relationship (Plant, 1990)

$$\mathbf{E}_s(\bar{r}) = \frac{1}{4\pi}\int_S [i\omega\mu(\hat{\mathbf{n}}\times\mathbf{H})\phi_G - (\hat{\mathbf{n}}\times\mathbf{E})\times\nabla\phi_G - (\mathbf{E}\cdot\hat{\mathbf{n}})\nabla\phi_G]dS\,. \tag{3.11}$$

In Equation (3.11), $\phi_G = \dfrac{e^{ik|\bar{r}-\bar{r}'|}}{|\bar{r}-\bar{r}'|}$ is a Green's function; the subscript s denotes the scattered field, $\bar{r}'$ is the variable of integration over the surface of interest and all other quantities are as defined in the preceding section. This expression enables us to predict the scattered fields that would be observed at a particular point, in terms of the fields or currents present on the surface of the scatterer. The analogous quantity for $\mathbf{H}(\bar{r})$ can readily be obtained by the duality of the electric and the magnetic fields.

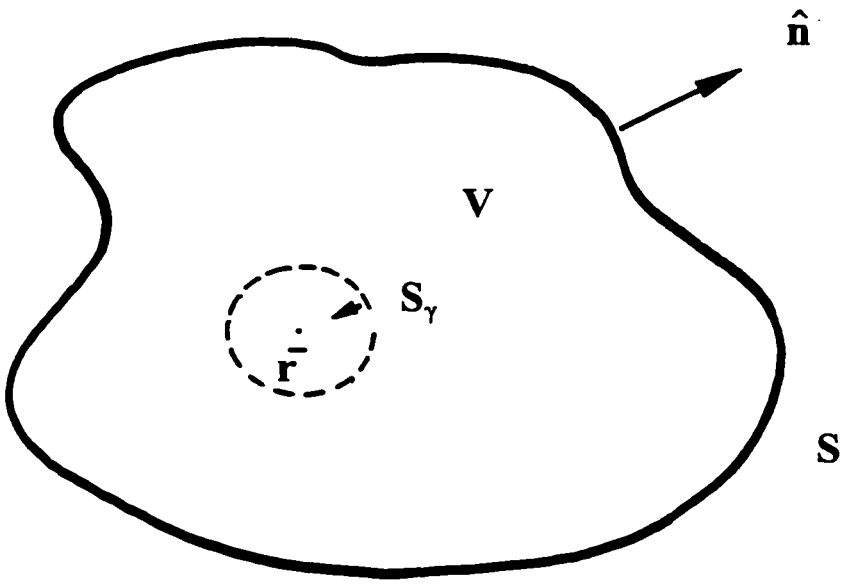

Figure 3.2: Illustration of primary variables in derivation of the Stratton-Chu equation.

If we wish to use the Stratton-Chu equations to predict the scattered fields at an observation point, we must know an expression for the total fields or currents on the scattering surface. For complicated, randomly rough surfaces such as the air-sea interface, it is not possible to obtain simple, analytic expressions for the fields or the currents on the surface. Therefore, additional assumptions are needed.

Approximations to the Stratton-Chu Equations

The two-scale, or composite surface model is a commonly encountered approximation for the Stratton-Chu equations. This model assumes that it is possible to partition the scattering elements of the ocean surface into two distinct regions of wave number space. Backscattering from the large-scale, low-wave number surface waves is modeled using the Physical Optics approximation, which will be described, in Section 3.3. Models of the scattering from small-scale, high-wave number waves exploit a resonant condition that occurs between the electromagnetic and the ocean waves known as Bragg scattering, which will be described in Section 3.4. Composite surface theory assumes that the two scales are disparate, and therefore independent. Under this assumption, the total scattering from the ocean surface can be represented as the sum of the contributions from these two regimes, i.e. $\sigma^0_{total}=\sigma^0_{physical\ optics}+\sigma^0_{Bragg}$.

These approximations make it possible to predict the scattering from complicated surfaces, but there are serious limitations to this approach. The most important and also the most controversial assumption is that is possible to treat the scattering at the two different scales as independent. This assumption clearly holds at the outer limits of the two regimes. However, this approach assumes that there exists a so-called 'separation wave number' that serves as the dividing point between the two scales. While broad guidelines exist regarding where this transition should be located, its precise location is somewhat subjective. Later

in this chapter, we will discuss the impact of various choices for separation wave number on the resulting radar cross section predictions. Also, realistically, there is significant wave energy at intermediate scales, which is not appropriately modeled by either the physical optics approximation or by the small perturbation theory. Nonetheless, composite surface theory has enabled researchers to make successful, albeit rough predictions of the radar scattering from the ocean surface for several decades. In the following two sections we will discuss the two model components that comprise this approach.

3.3 PHYSICAL OPTICS

The physical optics approximation applies to gently undulating large-scale ocean waves, i.e. those waves that have a radius of curvature that is large compared to the radar wavelength. For these waves, the surface fields can be estimated by using the so-called tangent plane approximation. Using this approach, the fields at a given point on the surface of the wave can be approximated by the fields that would be present on an infinite plane, tangent to the surface of the wave at that same point. This approach is illustrated in Figure 3.3. The field contribution due to the overall surface of the wave consists of an aggregation of such points.

Inherent to the tangent plane approximation are the following two assumptions (Brown, 1990): (1) The only field striking the point in question, p, is the incident field. Multiple scattering to p is excluded from consideration; (2) At p, the surface has sufficiently gentle curvature that it is possible to replace the surface itself by a plane tangent to the surface at p. These assumptions make it possible to estimate the fields on the surface in question.

If we can assume that k in the exponent of Equation (3.8) is quite large, then we can use the Method of Stationary Phase (Bender and Orszag, (1978), Nayfeh (1993)) to

simplify our analysis of this expression. This method enables us to describe the leading asymptotic behavior of generalized Fourier integrals of the form

$$I(\alpha) = \int_a^b f(t) e^{i\alpha h(t)} dt \,, \tag{3.12}$$

for b>a, when stationary points are present. A stationary point is defined to be a point where h'(t)=0 for some t in the interval [a,b]. In Equation (3.11), stationary points occur for those values of the long wave slopes that cause an incident ray to be specularly reflected.

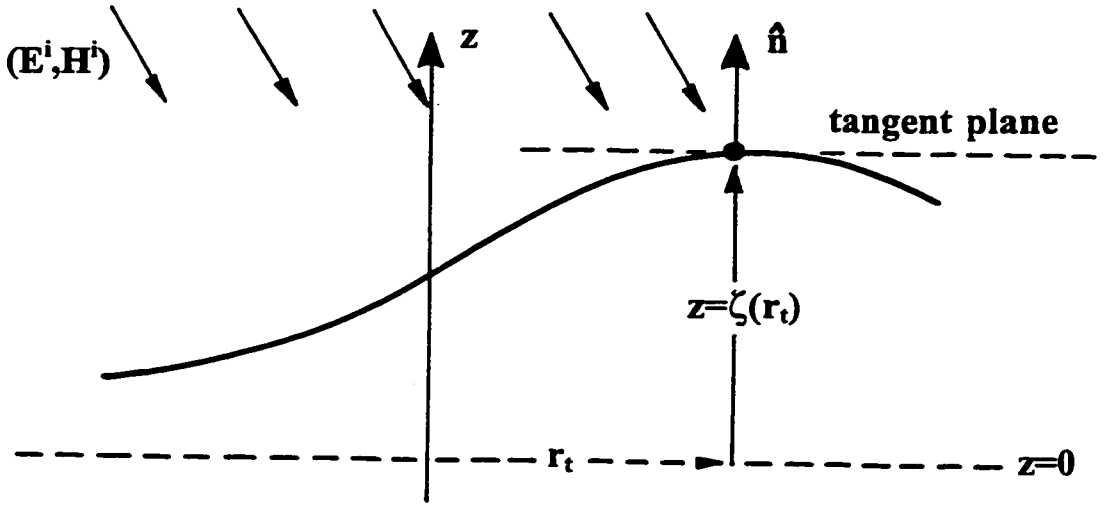

Figure 3.3: Illustration of the tangent plane approximation used in the physical optics approximation to the Stratton Chu equations, from Brown (1990).

Recall that the slopes of the surface waves are implicit to our definition of $\hat{\mathbf{n}}$, the unit normal to the surface at the point $\bar{\mathbf{r}}$. In using the Method of Stationary Phase, we evaluate Equation (3.11) at the points where the slopes assume specular values, and aggregate all such points to form a sum. In this computation, the random quantities are the surface displacements at the specular points, the number of specular points in the illuminated area and the surface curvatures at the specular points. To get the average scattered field, we must square the above-mentioned sum of the fields from the specular points, and then average it over the different realizations of the associated surface displacement. After considerable analysis efforts (Barrick, 1968), it is possible to define the scattering cross section per unit area in terms of this average. After taking the limit for large k and using the assumption of stationary phase, this result is also referred to as Geometric Optics.

Using these assumptions, the contribution to total cross section that arises from specular reflection of the radar energy from the long ocean waves can be given by

$$\sigma^0_{specular}(\theta_0,\varphi) = \frac{\pi}{\cos^4\theta_0}|R(0)|^2 P(\tan\theta_0,0). \tag{3.13}$$

Here, θ_0 denotes the radar incidence angle, φ denotes the azimuth angle and $P(S_x,S_y)$ denotes the probability distribution of the wave slopes in the plane of incidence, denoted by S_x, and orthogonal to it, given by S_y. In the case of Equation (3.13), $S_x=\tan\theta$ and $S_y=0$ specifies those wave facets that are perpendicular to the radar look direction (Jansen, 1993), and R(0) denotes the polarization-independent Fresnel reflection coefficient for normal incidence,

$$R(0)=\frac{1-\sqrt{\varepsilon}}{1+\sqrt{\varepsilon}} \tag{3.14}$$

where ε is the relative dielectric constant for the sea surface which is given by $\varepsilon = \frac{\varepsilon_w}{\varepsilon_0}$.

Here, ε_w is the dielectric constant for seawater and ε_0 is the dielectric constant for free space. The dielectric constant for seawater can be modeled as a function of salinity and temperature, as described in Ulaby, Moore and Fung (1986). After the physical optics criterion has been satisfied, in addition to being independent of polarization, Equation (3.13) is also independent of wavelength (Valenzuela, 1978).

The distribution of slopes is important to reflection and refraction of energy from the sea surface and is therefore of primary importance to radar remote sensing applications. Cox and Munk made a set of optical measurements of the slope of the sea surface in 1954, which, to this date, are still considered the standard against which other measurements are compared. Cox and Munk made airborne measurements of sea surface roughness in the vicinity of Hawaii using photographs of sun glitter from the sea surface. Measurements were made of both a 'clean' ocean surface, and one in which slicks (of varying amounts and types of oils) had been applied. In addition, the wind speed and direction were measured in the vicinity of where the photographs were obtained, so that the sea surface roughness measurements could be correlated with the local wind speed.
The mean squared slope (MSS) of the ocean surface is defined as

$$S^2 = \int k^2 S(\mathbf{k}) d\mathbf{k} . \tag{3.15}$$

Typically, this is decomposed into components aligned with the wind direction and components that are perpendicular to the wind direction, i.e.

$$S_x^2 = \int k^2 \cos^2(\theta) S(\mathbf{k}) d\mathbf{k} d\theta \tag{3.16}$$

$$S_y^2 = \int k^2 \sin^2(\theta) S(\mathbf{k}) d\mathbf{k} d\theta , \tag{3.17}$$

where x denotes the wind direction, and y denotes the orthogonal direction. Also of interest is S_{xy}, which is defined as

$$S_{xy}=\int k^2 \sin(\theta)\cos(\theta)S(\mathbf{k})d\mathbf{k}d\theta\,. \tag{3.18}$$

Cox and Munk suggested a model for each of the above quantities, under both 'clean' and 'slick' conditions, based on regression analyses of a large set of these data. Their results are summarized here.

$$S_{x(\text{C-M, clean})}^2 = 0.003+1.92\times10^{-3}W\pm0.002 \tag{3.19a}$$

$$S_{y(\text{C-M, clean})}^2 = 0.000+3.16\times10^{-3}W\pm0.004 \tag{3.19b}$$

$$S_{(\text{C-M, clean})}^2 = 0.003+5.12\times10^{-3}W\pm0.004 \tag{3.19c}$$

$$S_{x(\text{C-M, slick})}^2 = 0.003+0.84\times10^{-3}W\pm0.002 \tag{3.19d}$$

$$S_{y(\text{C-M, slick})}^2 = 0.005+0.78\times10^{-3}W\pm0.002 \tag{3.19e}$$

$$S_{(\text{C-M, slick})}^2 = 0.008+1.56\times10^{-3}W\pm0.004 \tag{3.19f}$$

In the above expressions, W corresponds to the wind speed in m/sec measured at 41 feet above sea level.

In Equation (3.13), we are assuming that the long wave slopes have a Gaussian distribution. To first order it is appropriate to treat the probability distribution of the sea surface slopes as Gaussian. However, Cox and Munk (1954 a, b) showed, as depicted in Figure 3.4, that the probability distribution of the slope of the sea surface deviates somewhat from Gaussian behavior. This issue is discussed in Phillips (1977). It is, nonetheless, a reasonable approximation to express both S_x and S_y as Gaussian random variables, so that their joint distribution function $P(S_x,S_y)$ is also Gaussian. That is,

$$P(S_x,S_y)=\frac{1}{2\pi\sqrt{\langle S_x^2\rangle\langle S_y^2\rangle-\langle S_xS_y\rangle^2}}\exp-\left(\langle S_x^2\rangle S_x^2-2\langle S_xS_y\rangle S_xS_y-\langle S_y^2\rangle S_y^2\right) \qquad (3.20)$$

where $\langle S_x^2\rangle,\langle S_y^2\rangle$ and $\langle S_xS_y\rangle$ are the mean squared slopes of the ocean surface waves defined in (3.16) -(3.17). In Section 3.4, we consider this probability distribution function for the long wave slopes once again.

The proportion of the total radar return from the sea surface attributable to ocean waves in the physical optics regime depends on incidence angle. For incidence angles that are close to normal, much of the scattering is specular and physical optics is the dominant

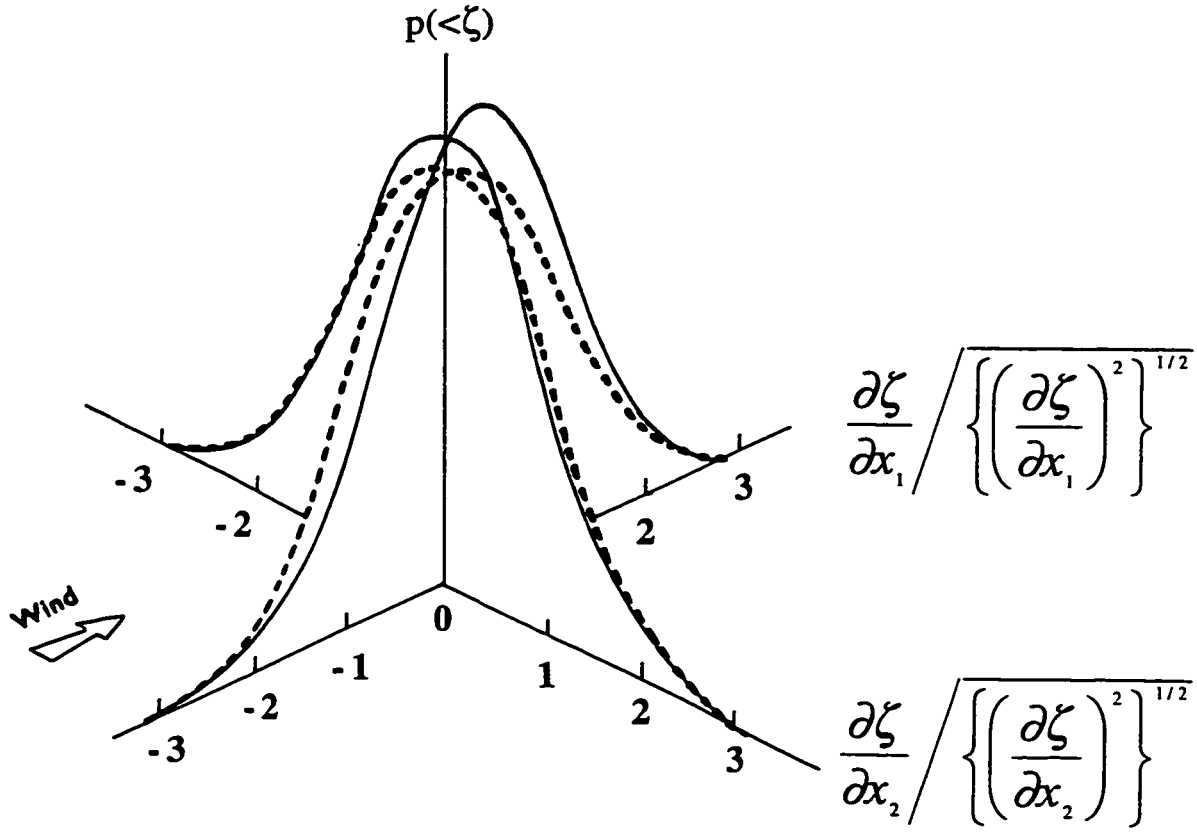

Figure 3.4: Illustration of the slope measurements obtained by Cox and Munk (1954), compared to the assumed Gaussian distribution for the slope of the sea surface, from Phillips (1977).

mechanism. For intermediate incidence angles, such as those of the ERS-1 system, where θ_{IA} is typically between 20 and 60 degrees, a comparatively small component of the total backscatter arises from physical optics-like scattering. For the ERS-1 system, the predominant return from the sea surface is due to Bragg scattering, which is discussed in the following section.

3.4 SMALL PERTURBATION APPROXIMATION

The primary mechanism governing radar backscattering from the sea surface at intermediate incidence angles is referred to as Bragg scattering, so named for W.L. Bragg, who in 1913 observed a similar type of scattering behavior when crystals are illuminated by X-rays (Plant, 1990). In radar remote sensing of the oceans, this mechanism arises when a resonance condition between the incident electromagnetic waves and the small-scale waves on the ocean surface is met, as illustrated in Figure 3.5. The Bragg theory predicts a linear relationship between the amplitude of the small-scale water waves and the square root of the associated backscattering cross section. This relationship was verified by Wright (Wright, 1966).

An expression for the Bragg component of radar backscattering from the air-sea interface can be derived from the Stratton-Chu equations using perturbation techniques. This has been accomplished successfully using two different approaches. One, due to Mitzner (1964), assumes an arbitrarily shaped mean surface, and expresses the fields on that surface using perturbation expansion techniques. Another approach due Rice (1951), replaces the unknown fields arising from a wavy surface of slight roughness by the equivalent currents on the flat, mean surface, whose values can be calculated from

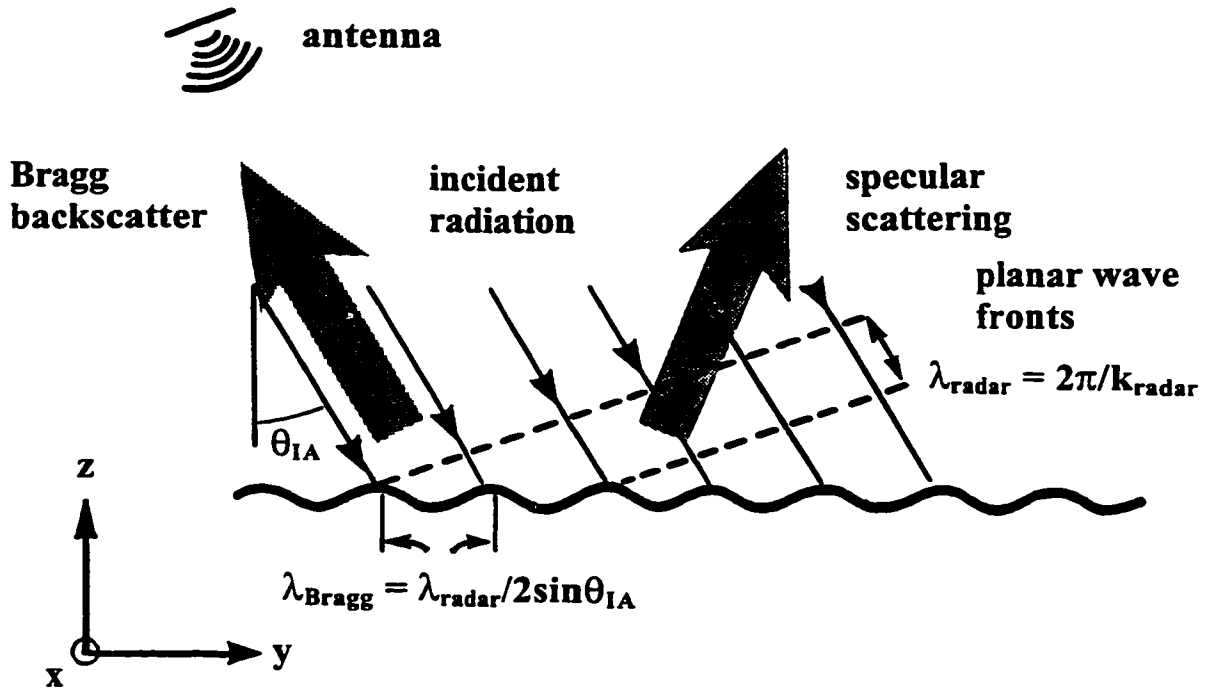

Figure 3.5: Illustration of the resonance condition arising between the electromagnetic waves and the waves at the ocean surface known as the Bragg condition, from Verma (1989).

expansions of the boundary conditions. Plant (1990) presents an overview of this physically intuitive approach, which we summarize below.

We initially take the air-sea interface to be flat, and assume that a transmitting microwave antenna illuminates this surface. An expression for the fields scattered from this hypothetical surface can be developed using the Stratton-Chu formulation. The average power incident on a receiving antenna can be estimated by taking the Fourier transform of an expression for the scattered power and convolving it with an expression for the antenna illumination pattern. The resulting expression consists only of Fourier

components with $k_x=0$ and $k_y=-k_0\sin\theta_0$. From this we can infer that only plane waves propagating from the surface directly towards the antenna will contribute to the received power. If we only consider scattering from a flat surface, however, all scattering will be directed away from the receiver. Therefore, it is necessary for us to take into account the actual roughness of the air-sea interface. To do this, we evaluate the boundary conditions at a sea surface displacement $z=\zeta(x,y,t)$, and express the resulting fields in terms of an expansion around $z=0$. This approach is valid only for small surface displacements, ζ, and small surface slopes, S_x and S_y. This condition is implemented by requiring that $|S_x| < 1$, $|S_y| < 1$. In addition, we require that the projection of the surface displacement on the incident ray is small, which is specified as $|k_0\zeta\cos\theta_0| < 1$ (Plant, 1990).

The following expression (the derivation of which is furnished in Plant (1990)) can be used to estimate the backscattered power incident on a receiving antenna from a slightly rough air-sea interface. Here, we consider the expression for the case of vertical polarization.

$$P_r = \left[\frac{A_e k_0 E_0^2}{8\omega\mu_0}\right]\left[\frac{k_0^2 G^2 \left|R_v\cos\theta_0 + T_v^2(1-\frac{\varepsilon_0}{\varepsilon_w})\sin^2\theta_0\right|^2}{2\pi r_0^2}\right]\left\langle\left|\int a^2(x,y)\zeta\exp(i2k_0 y\sin\theta_0)dxdy\right|^2\right\rangle \tag{3.21}$$

We will consider each of the three components of this expression separately, following the approach of Plant (1990).

In the first term on the right hand side, A_e denotes the effective area of the aperture, which is not necessarily the same as its physical area. The wave number corresponding to the transmitted radar wavelength, propagating in air is denoted by k_0; ω is the

corresponding radian frequency, μ_0 denotes the permeability for air and E_0 denotes the amplitude for the transmitted field. The first term on the right hand side of Equation (3.21) is, in fact, an expression for the transmitted power.

In the middle term, the variable G denotes the antenna gain, which is taken to be the same for the transmitter and the receiver, k_0 is the radar wave vector appropriate for scattering into the air and θ_0 denotes the nominal incidence angle. Variables included in the middle term can be used to determine the scattering coefficient for vertically polarized electromagnetic energy, which is given by

$$g_V(\theta_0) = R_V \cos^2\theta_0 + \frac{1}{2}T_v^2(1-\frac{\varepsilon_0}{\varepsilon_w})\sin^2(\theta_0). \tag{3.22}$$

More commonly, this is written as

$$g_V(\theta_0) = \frac{(\varepsilon-1)[\varepsilon(1+\sin^2\theta_0)-\sin^2\theta_0]\cos^2\theta_0}{[\varepsilon\cos\theta_0+\sqrt{\varepsilon-\sin^2\theta_0}]^2} \tag{3.23}$$

where ε is the relative dielectric constant described earlier in this section. The scattering coefficient for horizontal polarization can be given by

$$g_H(\theta_0) = \frac{(\varepsilon-1)\cos^2\theta_0}{[\cos\theta_0+\sqrt{\varepsilon-\sin^2\theta_0}]^2}. \tag{3.24}$$

The variation of g_V and g_H with incidence angle, θ_0, is illustrated in Figure 3.6.

An intuitive way of presenting the third term on the right hand side of Equation (3.21) entails considering a slightly different form for the radar equation than was presented at the beginning of this chapter, namely

$$P_r = \left(\frac{P_t G^2 \lambda^2}{(4\pi)^3 R^4}\right)\sigma. \tag{3.25}$$

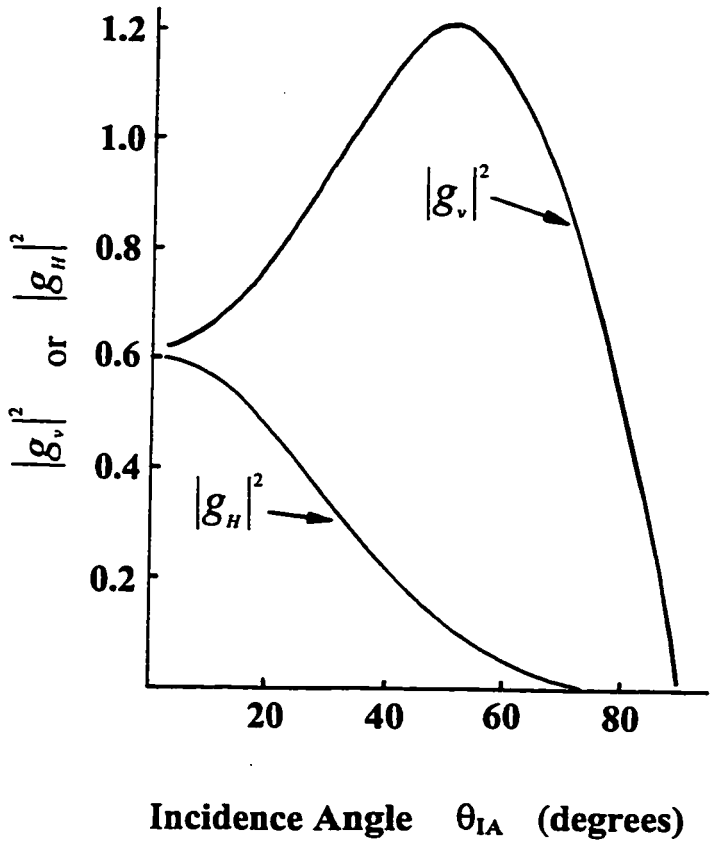

Figure 3.6: Variation of the polarization scattering coefficient g_v and g_h as a function of the angle of incidence θ_{IA}, from Plant (1990).

We can now use Equation (3.25) and Equation (3.21) to derive an expression for the radar cross section of the illuminated area, σ, by making use of the fact that the first term on the right hand side of Equation (3.21) expresses the transmitted power:

$$\sigma = \left(\frac{4k_0^4 |g_v|^2}{\pi} \right) \left\langle \left| \int a^2 \zeta \exp(i2k_0 y \sin\theta_0) dx dy \right|^2 \right\rangle, \tag{3.26}$$

where the angled brackets denote averaging. If we expand the second term of Equation (3.26), we obtain

$$\sigma = \left(\frac{4k_0^4 |g_v|^2}{\pi} \right) \int a^{*2}(x,y) a^2(x+x', y+y') \left\langle \zeta^*(x,y,t) \zeta(x+x', y+y', t) \right\rangle \exp(i2k_0 y \sin\theta_0) dx' dy' dx dy \tag{3.27}$$

$$\sigma = \left(\frac{4k_0^4 |g_v|^2}{\pi} \right) \iint a^{*2}(x,y) a^2(x+x', y+y') \langle \zeta^*(x,y,t) \zeta(x+x', y+y', t) \rangle \exp(i2k_0 y \sin\theta_0) dx' dy' dx dy \tag{3.27}$$

From this expression we can see that the electric field backscattered from a slightly rough air/sea interface is proportional to the two-dimensional Fourier transform of the surface displacement $\zeta(x,y,t)$ evaluated at $k_x=0$, $k_y=2k_0\sin\theta_0$ (Plant, 1990). It is more appropriate, however, to use the normalized radar cross section, σ^0, for applications involving scatterometer measurements of the sea surface. To obtain an expression for σ^0, we need to normalize Equation (3.27) by area. This requires that we make some simplifying assumptions regarding the illumination pattern, $a(x,y)$, and the sea surface displacement, ζ.

If we assume that $a(x,y)$ varies only slowly in distances over which the surface displacement decorrelates, then we may set x' and y' equal to zero in $a^2(x,y)$. We can then express the illuminated area as

$$A_{ill} = \iint |a^2(x,y)|^2 dx dy. \tag{3.28}$$

If, in addition, we assume that $\zeta(x,y,t)$ is a homogeneous, mean-zero, Gaussian process, then it is independent of x and y, and we can use the fact that the covariance of the sea surface displacement is the Fourier transform of the power spectral density of the sea surface. If we convert the wave number spectrum from (k,θ) to (k_x,k_y) using the relationship $k_x=k\cos\theta_0$ and $k_y=k\sin\theta_0$, we can write

$$\Psi(0, 2k_0 \sin\theta_0) = \frac{1}{4\pi^2} \iint \langle \zeta^*(x,y,t) \zeta(x+u, y+v, t) \rangle \exp(ik_0 y \sin\theta_0) du dv \tag{3.29}$$

There is a distinction between the directional wave spectrum $\Psi(k,\theta)$ introduced in Chapter 2 and the two-dimensional spectrum $\Psi_S(k,\theta)$ that is described in Banner (1990) and in Caudal and Hauser (1996). The *directional wave number* spectrum is defined as

$$\Psi(\mathbf{k}) = 2\int_0^{\infty} E(\mathbf{k},\sigma)d\sigma, \tag{3.30}$$

where $E(\mathbf{k},\sigma)$ was defined in Equation (2.19) and $\Psi(\mathbf{k})=\Psi(k,\theta)$; it represents the actual wave number directional distribution of wave energy propagation (Banner, 1990). On the other hand, the *wave number* or *folded wave number* spectrum

$$\Psi_s(\mathbf{k}) = \int_{-\infty}^{\infty} E(\mathbf{k},\sigma)d\sigma, \tag{3.31}$$

is the Fourier transform of the covariance function of a frozen spatial image of the sea surface, and as such it has a reflectional symmetry in wave number (Caudal and Hauser, 1996). The folded wave number spectrum does not contain actual wave propagation information; it has partitioned the wave energy equally into components 180° apart (Banner, 1990). Although this form contains no information about the direction of propagation of the Fourier components, we can use the fact that

$$\Psi_s(k,\theta)=0.5[\Psi(k,\theta)+\Psi(k,\theta+\pi)] \tag{3.32}$$

to infer azimuthal behavior, accepting the fact that our solutions will contain an ambiguity of 180°.

We may now obtain an expression for the normalized radar cross section due to Bragg scattering from the ocean surface (for the case of vertical transmit and receive polarization):

$$\sigma^0_{Bragg} = 16\pi k_0^4 |g_v(\theta_0)|^2 \breve{\Psi}(0, 2k_0 \sin\theta_0) \tag{3.33}$$

where $\breve{\Psi}(0, 2k_0 \sin\theta_0)$ is the folded spreading function described above, transformed from $\Psi(k,\theta)$ to $\Psi(k_x,k_y)$ and evaluated at $k_x=0$ and $k_y=2k_0\sin\theta_0$.

If the Bragg scatterers were distributed on a flat surface, then Equation (3.33) would enable us to predict the σ^0 for a given area of the ocean surface. However, the situation on the ocean surface more closely resembles a carpet of Bragg scatterers riding on the surface of the large-scale ocean waves. Therefore, we must consider the effects on the Bragg-scale roughness elements of tilting and modulation by the longer waves. The effects of tilting by the long waves are typically included in a composite surface model by averaging the cross section for a tilted, slightly rough surface over all possible large-scale tilts. In one dimension, this can be written as

$$\sigma^0(\theta_0) = \int_{-\infty}^{\infty} \sigma^0_{Bragg}(\theta_0, h_x) p(h_x) dh_x, \tag{3.34}$$

where $p(h_x)$ is the slope probability density function. This approach assumes that we may add the return from the various portions of the sea surface incoherently. This is valid in the context of small perturbation theory, which assumes that the fields at different angles of incidence are proportional to the different Fourier components of the surface. Since these components are independent, the fields are independent as well and can be added together incoherently (Durden, 1986).

In order to evaluate Equation (3.34), we need to estimate $p(h_x)dh_x$. This is typically done by assuming that the long wave slopes have a Gaussian probability distribution function, as given in Equation (3.20), which requires that we specify the mean squared slopes of the sea surface, that was given in Equations (3.16) and Equation (3.17). In Equation (3.34), we only consider the one-dimensional case.

To determine the desired estimates of the mean squared slopes of the sea surface, the integrals must make use of the separation wave number, k_{cut}. The separation wave number is a critical aspect of the two-scale model. The definition of the separation wave number assumes that there exists a particular wave number, k_{cut} that divides the wave number spectrum of the sea surface into two, essentially independent components. The separation wave number is applied in Equations (3.36a) and (3.36 b) as the upper limit of integration. Lyzenga and Bennett (1988), have suggested that a good choice for k_{cut} is

$$k_{cut} \sim O(k_{Bragg}/3). \tag{3.35}$$

While different researchers have used a range of choices for k_{cut}, it was shown by Plant (1986) that the mean squared slopes are not particularly sensitive the exact value assumed by this variable. For simplicity, we have taken $k_{cut} = (k_{Bragg}/3)$ in the research presented here. In Equations (3.36), k_{min} corresponds to the smallest wave number included in our analyses. This will be given by the smallest wave number measured by the NDBC buoys which is k~0.004. Therefore, we have

$$S_x^2 = \int_{k_{min}}^{k_{cut}} \int_0^{2\pi} k^2 \cos^2\varphi \Psi(k,\varphi) k dk d\varphi \tag{3.36a}$$

$$S_y^2 = \int_{k_{min}}^{k_{cut}} \int_0^{2\pi} k^2 \sin^2\varphi \Psi(k,\varphi) k dk d\varphi . \tag{3.36b}$$

In Equations (3.36), the x-axis denotes the plane of incidence of radar energy, and the y-axis is the orthogonal direction. $\Psi(k,\varphi)$ is the two-dimensional power spectral density of the ocean surface, where φ denotes the angle relative to the radar look direction and k denotes wave number.

It is necessary to consider two reference frames to characterize the effects of the long waves on the Bragg scatterers: a local reference frame that includes the effects of

tilting by the underlying waves and a more generalized, 'earth' reference frame. Figure 3.7 depicts the two coordinate systems.

An expression for the normalized radar cross section that would arise from an ocean surface consisting of small-scale scatterers that are tilted by the long waves is

$$\sigma^0_{tiltedBragg} = 8\pi k_0^4 \iint \left|\breve{g}(\theta_0, S_x, S_y)\right|^2 \breve{\Psi}(\varphi, 2k_0 \sin\breve{\theta}_0) P(S_x, S_y) dS_x dS_y . \tag{3.37}$$

Here, k_0 is the radar wave number, $\breve{\theta}_0$ is the local radar incidence angle depicted in Figure 3.7 and $\breve{g}(\theta_0, S_x, S_y)$ is a polarization-dependent geometrical factor. In the case of vertical polarization, it is given by

$$\breve{g}(\theta_0, S_x, S_y) = (\hat{v} \cdot \hat{v}')^2 g_v + (\hat{v} \cdot \hat{h}')^2 g_h , \tag{3.38}$$

where $(\hat{v}, \hat{h})$ and $(\hat{v}', \hat{h}')$ are the unit vertical and horizontal polarization vectors in the earth frame and local frame, respectively. These are given by

$$(\hat{v}, \hat{v}') = \frac{\sin\theta_0 - S_x \cos\theta_0}{\sqrt{(S_x \cos\theta_0 - \sin\theta_0)^2 + S_y^2}} \tag{3.39a}$$

and

$$(\hat{v}, \hat{h}') = \frac{-S_y}{\sqrt{(S_x \cos\theta_0 - \sin\theta_0)^2 + S_y^2}} . \tag{3.39b}$$

The relationship between the local incidence angle and the earth frame incidence angle is given by

$$\cos\breve{\theta}_0 = \frac{\cos\theta_0 + S_x \sin\theta_0}{\sqrt{1 + S_x^2 + S_y^2}} \tag{3.40}$$

$$\sin\bar{\theta}_0 = \frac{\sqrt{S_y^2 + (\sin\theta_0 - S_x\cos\theta_0)^2}}{\sqrt{1+S_x^2+S_y^2}}, \tag{3.41}$$

where S_x and S_y are the sea surface slopes in the plane of incidence and the orthogonal direction, respectively. The relationships between variables in the two coordinate frames are summarized in Jansen (1993).

We use equation (3.37) in this research to predict the tilted Bragg component of the total radar backscattering from the sea surface, where the two dimensional integration over long wave slopes is accomplished using Gaussian quadrature.

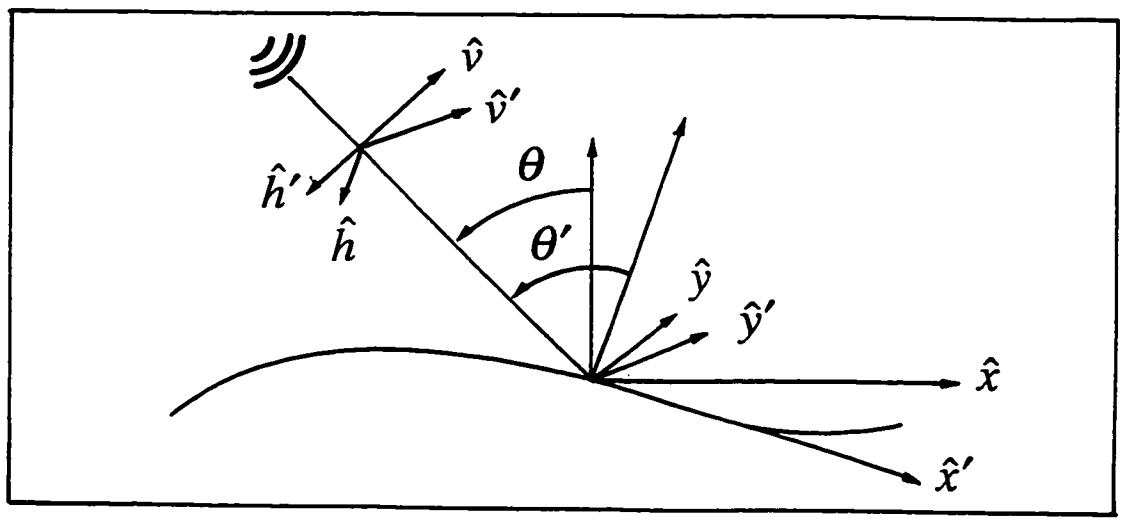

Figure 3.7: The two primary reference frames for calculating the radar cross section arising from the tilted Bragg or composite surface model for predicting the scattering from the small-scale waves propagating at the tilted air-sea interface, from Jansen (1993).

Now that we have introduced the Small Perturbation Theory and its relationship to the Two-Scale model for predicting radar backscattering from the ocean surface, we will investigate the impact of integrating over long wave slopes on the prediction of normalized radar backscatter. To do so, we will compare the backscatter predictions obtained using the so-called 'Nominal' Bragg model given by Equation (3.33) with the 'Tilted Bragg' model given by Equation (3.37).

3.5 INVESTIGATION OF LONG WAVE EFFECTS

In the preceding section, we presented a derivation of the expressions used to characterize the component of radar backscatter arising from the small-scale waves on the ocean surface. This expression is repeated here for convenience:

$$\sigma^0_{Bragg} = 16\pi k_0^4 \left| g_v(\theta_0) \right|^2 \breve{\Psi}(0, 2k_0 \sin\theta_0) . \tag{3.33}$$

Here, $\breve{\Psi}(0, 2k_0 \sin\theta_0)$ is the folded wave number spectrum defined in equation (3.31). We will refer to expression (3.33) as the 'Nominal Bragg Model'. Implicit in this expression is the assumption that the Bragg scatterers are distributed on a flat surface, rather than the undulating surface of the large scale waves on which these small waves actually ride. It is recognized that a more realistic characterization of the backscattering from these small waves takes into account some of the effects imparted to the Bragg scatterers by tilting and modulation by the underlying waves. One approach often used to incorporate these long wave effects was presented in Equation (3.37). We refer to this expression as the 'Tilted Bragg Model', which is repeated here for convenience as well:

$$\sigma^0_{tiltedBragg} = 8\pi k_0^4 \iint \left| \bar{g}(\theta_0, S_x, S_y) \right|^2 \breve{\Psi}(\varphi, 2k_0 \sin\bar{\theta}_0) P(S_x, S_y) dS_x dS_y . \tag{3.37}$$

In this expression, the slope of the sea surface is assumed to obey a Gaussian distribution,

which is described, in part, using the variance of the long wave slopes in the plane of incidence and the orthogonal direction. This assumed slope distribution suggests that we consider the Bragg scatterers to be distributed on a series of tilted 'facets' rather than a flat surface. Consequently, the primary angular quantities must be modified to include the effects of the tilting by the long waves, as illustrated in Figure 3.7.

For many years there has been considerable interest directed at studying the interaction between short surface waves and the underlying swell or long wind waves. Many theoretical and experimental efforts (e.g. Plant and Wright (1980),Valenzuela and Laing (1972)) have investigated various aspects of this complicated problem. Starting in the mid-1970s, radar remote sensing measurements have enhanced these efforts considerably. There have been several successful studies investigating this problem, but none have directly compared predictions of σ^0 using a nominal Bragg model with predictions of σ^0 using a tilted Bragg model that included a realistic characterization of the swell. Durden (1986) performed a limited investigation of long wave effects, but it used the Pierson-Moskowitz spectrum (Equation 2.24) to characterize the spectrum for the long wave number waves. Becaues the ASM uses *in situ* buoy measurements to characterize the low-wave number components, it is ideally suited for such an investigation.

It is valuable to characterize the magnitude of the long wave effects for a number of reasons. First, it is important to identify the contribution of non-local effects on radar backscatter. It is recognized that the short wave portion of the spectrum dominates radar backscattering from the ocean surface at moderate incidence angles. The high-wave number regime of the spectrum changes most rapidly, and primarily reflects the effects of the local winds. However, depending on the magnitude of the tilting effects, there could potentially be an appreciable penalty on radar cross section predictions that do not properly take long wave effects into account. Empirical schemes for predicting σ^0, such as CMOD-4, are parameterized only in terms of the local wind speed, which excludes these effects.

Norfolk VA

4/8/93	u*=0.39 (m/s)	wd=337	swh=2.7 m				
beam	look (wrt N)	ia	mss x	mss y	sig0 tilt	sig0 nom	diff (dB)
fore	213.6	43.9	3.00E-02	2.95E-02	-18.633	-19.101	0.468
mid	259.2	33.4					
aft	304.8	43.8	2.95E-02	3.00E-02	-17.570	-17.878	0.309
3/30/94	u*=0.16 (m/s)	wd=305	swh=0.4 m				
beam	look (wrt N)	ia	mss x	mss y	sig0 tilt	sig0 nom	diff (dB)
fore	53.4	56.8	1.69E-02	1.76E-02	-17.122	-16.364	-0.758
mid	99.4	45.4	1.76E-02	1.69E-02	-12.434	-12.403	-0.030
aft	145.3	56.8	1.76E-02	1.69E-02	-15.086	-14.318	-0.768
3/1/93	u*=0.51 (m/s)	wd=324	swh=2.9 m				
beam	look (wrt N)	ia	mss x	mss y	sig0 tilt	sig0 nom	diff (dB)
fore	213	36.3	6.41E-02	6.54E-02	-13.686	-15.834	2.148
mid	258.6	26.9					
aft	304	36.2	6.55E-02	6.41E-02	-12.388	-14.134	1.746
2/23/93	u*=0.24 (m/s)	wd=270	swh=0.7 m				
beam	look (wrt N)	ia	mss x	mss y	sig0 tilt	sig0 nom	diff (dB)
fore	54.99	38.3	1.78E-02	8.494 E -3	-18.996	-20.177	1.181
mid	99.98	28.6	1.74E-02	1.72E-02	-16.576	-16.596	0.020
aft	146.96	38.3	1.75E-02	1.77E-02	-19.626	-20.969	1.343
2/13/93	u*=0.37 (m/s)	wd=220	swh=1.7 m				
beam	look (wrt N)	ia	mss x	mss y	sig0 tilt	sig0 nom	diff (dB)
fore	55.3	42	2.31E-02	2.19E-02	-12.877	-13.143	0.266
mid	101.1	31.8	2.25E-02	2.24E-02	-11.596	-11.772	0.176
aft	146.5	42	2.19E-02	2.31E-02	-14.584	-15.200	0.616

Table 3.1: Summary of analysis of long wave effects for Norfolk, VA.

Yaquina Bay

3/20/93	u*=0.42(m/s)	wdir=246.0	swh=2.9 m				
beam	look (wrt N)	ia	mss x	mss y	sig0 tilt.	sig0 nom.	diff. (dB)
fore	214.6	53.1	5.57E-02	5.22E-02	-15.850	-15.528	-0.322
mid	260.5	41.7	5.37E-02	5.42E-02	-11.805	-12.924	1.120
aft	306.4	53	5.22E-02	5.57E-02	-17.212	-16.778	-0.435
3/4/93	u*=0.45 (m/s)	wdir=305.0	swh=4.6				
beam	look (wrt N)	ia	mss x	mss y	sig0 tilt.	sig0 nom.	diff. (dB)
fore	215.1	56.9	6.18E-02	5.85E-02	-13.458	-13.125	-0.334
mid	261.1	45.4	5.89E-02	6.14E-02	-11.701	-12.725	1.024
aft	307.2	56.8	5.85E-02	6.18E-02	-14.283	-14.023	-0.260
2/16/93	u*=0.27 (m/s)	wdir=55.0	swh=1.9 m				
beam	look (wrt N)	ia	mss x	mss y	sig0 tilt.	sig0 nom.	diff. (dB)
fore	215.1	56.9	3.26E-02	3.06E-02	-16.055	-15.229	-0.827
mid	261.1	45.4	3.13E-02	3.19E-02	-13.098	-13.344	0.246
aft	307.2	56.8	3.06E-02	3.26E-02	-17.932	-17.258	-0.673
2/10/93	u*=0.24 (m/s)	wdir=98.0	swh=2.2 m				
beam	look (wrt N)	ia	mss x	mss y	sig0 tilt.	sig0 nom.	diff. (dB)
fore	213.7	45.6	2.84E-02	2.81E-02	-19.281	-19.547	0.266
mid	259.4	34.9	2.86E-02	2.79E-02	-14.168	-15.302	1.134
aft	305.1	45.5	2.81E-02	2.84E-02	-17.878	-17.696	-0.183
2/7/93	u*=0.11	wdir=135.0	swh=2.2 m				
beam	look (wrt N)	ia	mss x	mss y	sig0 tilt.	sig0 nom.	diff. (dB)
fore	213.1	40.3	1.79E-02	1.81E-02	-13.979	-14.855	0.875
mid	258.8	30.2	1.81E-02	1.80E-02	-10.996	-10.991	-0.005
aft	304.3	40.1	1.81E-02	1.80E-02	-12.211	-12.628	0.417

Table 3.2: Summary of analysis of long wave effects for Yaquina Bay OR,

While it is possible that these models include some degree of averaged long wave effects, depending on the magnitude of this phenomenon, wind retrieval performance could probably be improved by inclusion of these effects.

In Tables 3.1 and 3.2 we compare predictions of $\sigma^0_{nominal}$ with σ^0_{tilted}. Half of the cases we considered were obtained in the vicinity of Norfolk, VA, which is located off the East Coast of North America. When there is an offshore breeze at this location, the buoy measurements will include minimal contributions from swell. In the vicinity of this buoy, we compared predictions of $\sigma^0_{nominal}$ and σ^0_{tilted} for light, intermediate and strong winds. In addition, we analyzed measurements obtained in the vicinity of Yaquina Bay, OR, which is located off the west coast of North America, and is much more likely to have swell present. We compared predictions of $\sigma^0_{nominal}$ and σ^0_{tilted} at both locations under a broad range of wind conditions.

Consistent with the findings of Durden (1986), our results suggest that long wave effects on Bragg scatterers are comparatively small: typically on the order of 1 dB, with the greatest differences occurring at shallow angles of incidence, as one would expect. It must be borne in mind, however, that these results are strongly dependent on the choice of spectral model and also on the choice of the model parameter α. Although the results we present span a broad range of wind and wave conditions, they are based on the analysis of a limited number of cases, and as such, it is difficult to draw any strong conclusions at this time on the basis of these results.

This investigation, while still preliminary, shows that this technique is a valuable tool for investigating the effects of long waves on radar backscatter. This tool offers promise for future improvements to modeling efforts both in cross section prediction and wind retrieval. A future extension of this work could be to obtain a more comprehensive and statistically valid set of observations, representing a broad range of wind and wave

conditions, and to use these data to more systematically characterize the impact of long wave effects.

3.6 APPLICATION

We will now consider an application of our friction velocity retrieval scheme that illustrates the relationship between its two primary components, namely, the ocean wave model and the composite surface scattering model. In this example, we consider the vicinity of Yaquina Bay, Oregon, on 4 March, 1993, at 6:47 GMT. As mentioned in Chapter 2, at this location there is a NDBC buoy that obtains measurements of the directional spectrum of ocean waves. We have selected this particular date and time for analysis because, as we will present in Chapter 4, it corresponded to an ERS-1 overpass that obtained σ^0 measurements of the area.

To identify the appropriate ERS-1 resolution cells to include in such a comparison, we consulted Monaldo (1988) and Dobson et al. (1987). These papers analyzed the impact of various temporal and spatial separations on comparisons between buoy and satellite measurements. They noted that the maximum temporal separation between a pair of measurements will be 30 minutes since buoys obtain measurements once per hour. Regarding spatial separation, to ensure that the meteorological conditions within a resolution cell and those at the buoy were reasonably similar, we took the maximum allowable separation to be 50 km, which was considerably more conservative than the findings of Monaldo and Dobson.

The environmental conditions recorded at the buoy location at this date and time are: U_5=8.4 m/sec, T_{air} = 10.5° C, T_{sea} = 10.2° C, wind direction = 95 ° and barometric pressure = 1012.8, which were used to estimate for u* using the approach described in Section 2.1. This estimate of u* served as one of the two inputs to our ocean wave spectral model. The additional input to our spectral model was the wind direction. In this example,

we considered, for this fixed friction velocity, all possible choices for the wind direction. That is, we obtained 72 different realizations of our two-dimensional ocean wave number spectrum: one for each choice of θ_{wind}=[0°,5°,10°,...355°], each of which was regarded as a hypothetical wind direction. The cost function defined in Chapter 4 provides a means by which we hope to identify the 'true' wind direction from among these hypothetical ones. In conjunction with this set of ocean wave number spectra, specified several additional parameters: radar frequency and polarization, which we took to be those for the ERS-1 system (frequency = 5.3 GHz; polarization = vv). For the complex dielectric constant of the sea surface we have assumed ε=(81.0,0.0), as suggested by Plant (1986). Additional inputs were the mean squared slopes in the plane of incidence and in the perpendicular plane computed from the ASM spectrum. Finally, in order to generate a suite of σ^0 predictions for each of the three beams of the ERS-1 Active Microwave Instrument (AMI), we used the incidence and azimuth angles provided by ESA, describing the position of each antenna beam at the time of the buoy overpass by the satellite. Using these inputs, we obtained the radar cross section predictions discussed below.

The results of these σ^0 predictions are illustrated in Figures 3.8 a – 3.8 c. These plots serve two purposes: first, they illustrate the general σ^0 prediction capability of our technique. Also, they illustrate the expected azimuthal variability of σ^0 analogous to that depicted in Figure 1.3. That is, when the hypothetical wind direction corresponds to the antenna look direction, σ^0 is a maximum; in the orthogonal direction, σ^0 is a minimum. Figures 3.9 a – c illustrate the analogous σ^0 predictions, but in these figures, in addition to considering all hypothetical wind directions, we also consider 23 different possible choices for u*: (u*=[0.08,0.10,0.12,...,0.52], each of which corresponded to a hypothetical wind friction velocity, if we were to assume that the true friction velocity was unknown.

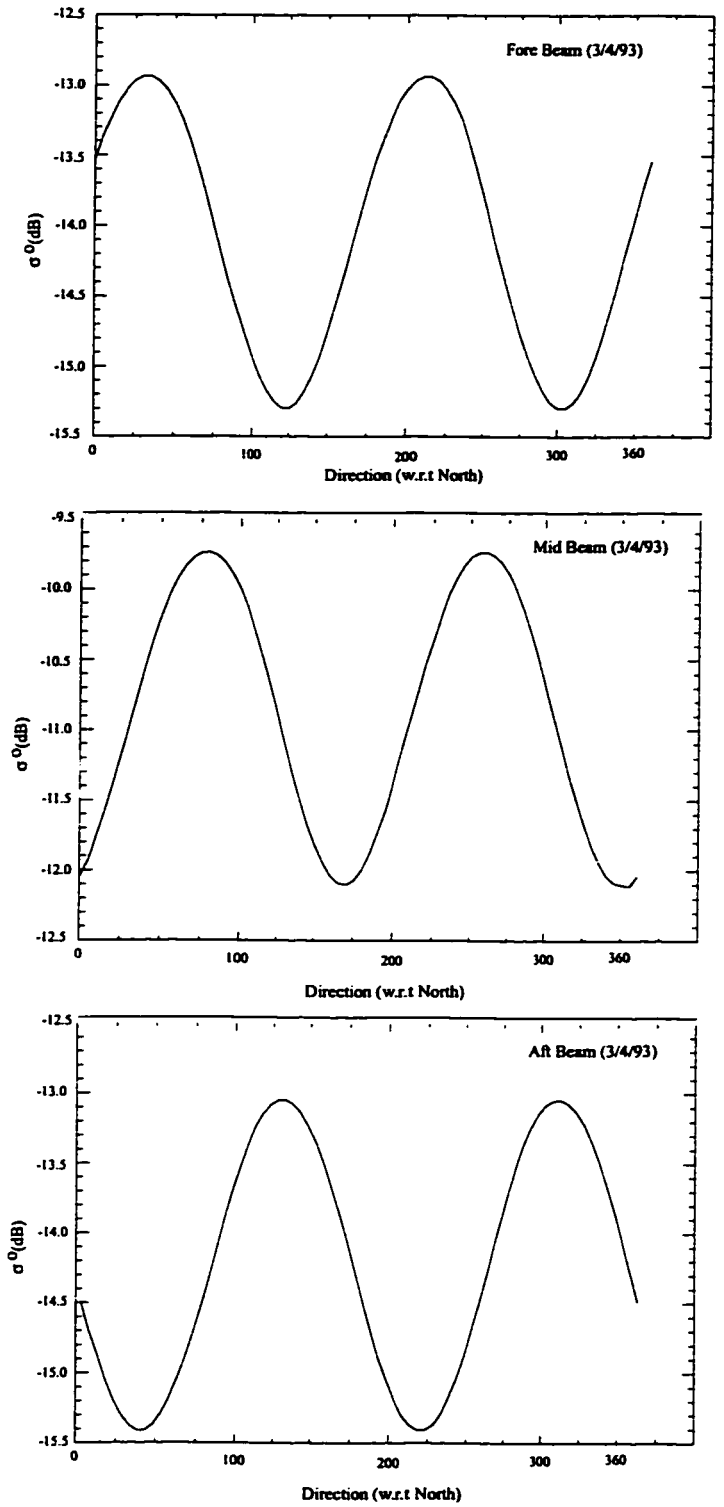

Figure 3.8: Illustration of the azimuthal variability observed for each beam, holding u* constant at 0.44 and varying direction from 0 to 355 degrees. 3/4/93. The incidence and azimuth angles for the fore, mid and aft beams are: (56.9,215.1),(45.4,261.1), (56.8,307.2), respectively.

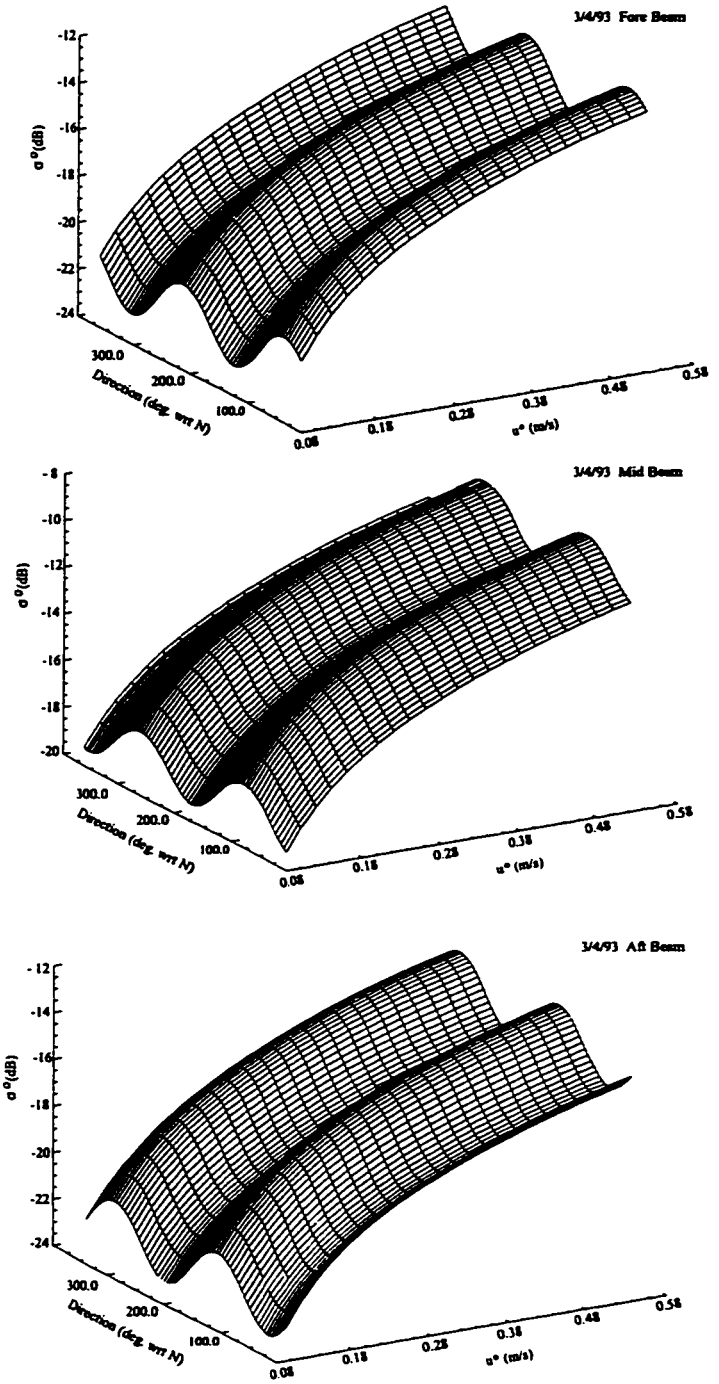

Figure 3.9: Depiction of variability of σ^0 with both azimuth angle and u*. Incidence and azimuth angles are as specified in Figure 3.8, for 3/4/93

These plots illustrate both the azimuthal variability in σ^0 as well as the anticipated increase in the σ^0 predictions as u* increases.

3.7 RECENT SCATTERING MODELS

Within the last year, an enhanced form of the composite surface model for predicting radar backscattering from the ocean surface has been proposed by Romeiser et al. (1997). The method they present is based on Bragg scattering theory, but includes additional terms derived from obtaining a Taylor expansion in the two-dimensional surface slope. The results of this expansion are terms that are used to characterize the effect of geometric and hydrodynamic modulation of the Bragg scatterers by the long, underlying wave field. The modified composite surface model presented by Romeiser et al. includes higher order terms that may make it possible to resolve directional ambiguity. We hope that in the future it will be possible to use this advanced electromagnetic scattering model in our scheme for retrieving friction velocity at the ocean surface.

Another technique that is well suited for modeling the electromagnetic scattering from the ocean surface is known as the Integral Equation Model (IEM) (Fung, 1994). This approach uses both the surface roughness spectrum as well as the surface bispectrum. Two-dimensional models of the roughness spectrum are centro-symmetric, and therefore can not be used to resolve directional ambiguity to within 180°. As we mentioned in the preceding section, two solutions are possible for each potential direction, φ: φ and $\varphi+\pi$. Skewness is a third order statistic that can be used to characterize the asymmetry of a distribution. The bispectrum used in the IEM includes third-order statistics, which could make resolution of the wind direction and the upwind/downwind asymmetry possible. We hope to implement the IEM in a future realization of the friction velocity retrieval scheme developed in this research.

3.8 CONCLUSIONS

In this chapter we have described the scattering model by which we obtain predictions of the electromagnetic scattering from the air-sea interface. Our primary focus is on the composite surface, or two-scale scattering model. We have used the scheme developed in this research to investigate the impact of long wave effects on σ^0 prediction. This was accomplished by comparing the difference in σ^0 predictions obtained from a nominal Bragg and a tilted Bragg scattering model. In addition, we have presented an example illustrating the application of the two-scale model to spectra generated by the ASM described in Chapter 2. This example demonstrates that our scheme reproduces both the anticipated azimuthal variability as well as the increase in radar backscatter with friction velocity. In Chapter 4, we will present our technique for retrieving the friction velocity and direction at the ocean surface. This technique derives predictions of σ^0 using the spectral model presented in Chapter 2 and the scattering model described in Chapter 3. These predictions are combined with σ^0 measurements obtained by the ERS-1 scatterometer in a cost function. The minimization of this cost function yields estimates of the friction velocity and direction at the ocean surface.

CHAPTER 4. COST FUNCTION ANALYSES

4.1 INTRODUCTION

The goal of this research is to estimate the friction velocity and direction at the ocean's surface using physically-based models and space-borne scatterometer measurements. The approach we pursue to achieve this end combines the following two components: measurements of normalized radar cross section, σ^0, obtained by the ERS-1 Active Microwave Instrument (AMI) and model-based predictions of σ^0. These predictions are derived from the application of the Aggregate Spectral Model (ASM), and a composite surface scattering model. These models are described in Chapters 2 and 3, respectively. The σ^0 measurements and predictions are selected so that they are nearly temporally coincident and spatially co-located, for use in this analysis. The analysis sites are chosen because they contain ocean surface measurement buoys that assist us in evaluating the results.

A cursory overview of our scheme for retrieving the friction velocity and direction was provided in the introductory chapter and illustrated in Figure 1.5. We now revisit this diagram in Figure 4.1 and consider the relationship between its components more closely. At the top of the figure, we note that the friction velocity u*, and the wind direction θ_{wind}, are the two inputs required for the ASM, the ocean wave spectral model used in this

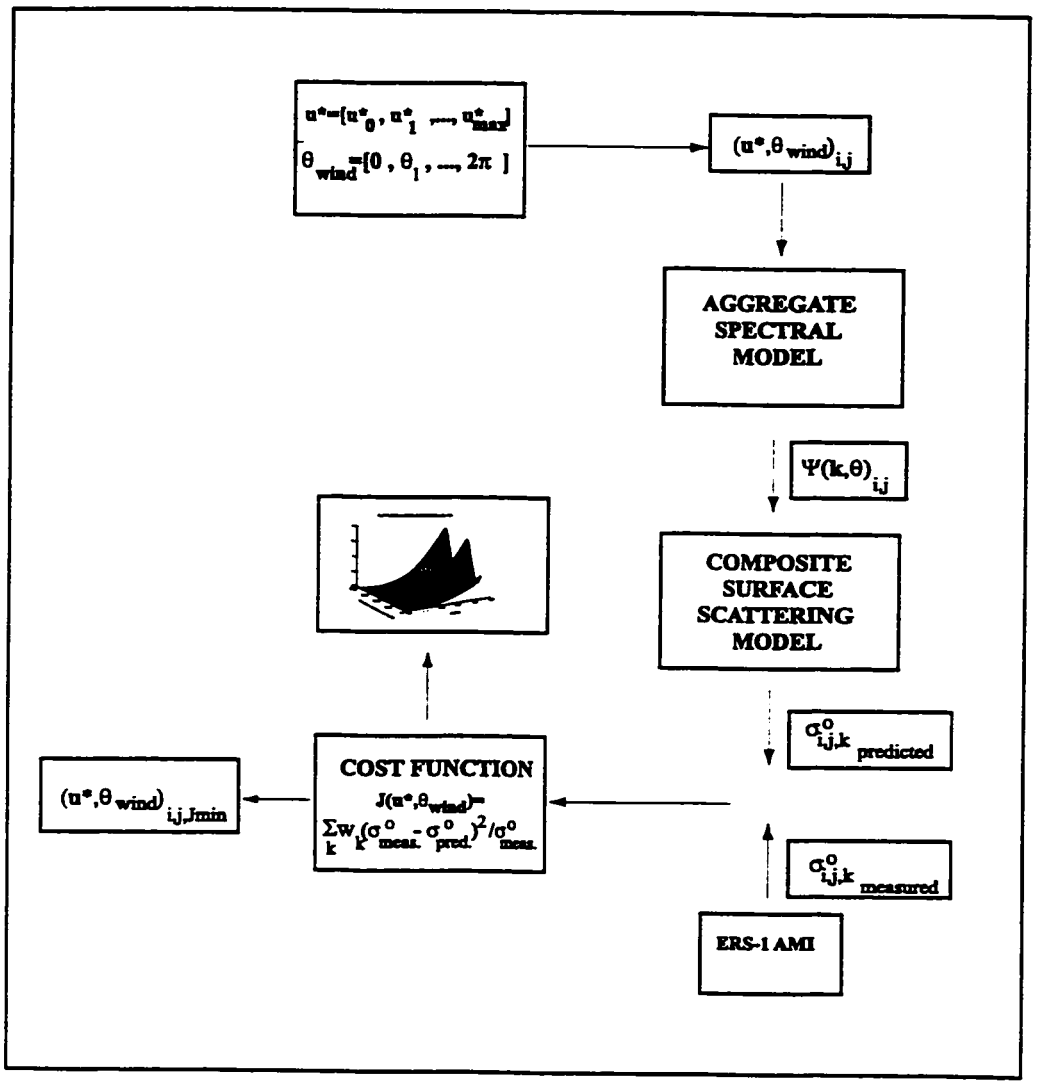

Figure 4.1: An overview of the friction velocity retrieval scheme implemented in this research. A detailed description of this scheme is provided in Figure 1.5.

research. As discussed in Chapter 2, we choose to retrieve the friction velocity and not the wind speed.

At the air-sea interface, the stress field is determined by the wind speed, the stability of the air column and the sea state. It is recognized by many, such as Janssen et al. (1998), that wind waves, which dominate the Bragg component of radar backscatter, are more closely related to the surface stress field than to the wind field. The surface stress, τ, is directly related to the friction velocity u* by the relationship $\tau=\rho_a u^{*2}$, where ρ_a is the air density. Using a straight-forward set of calculations, such as the ones described in Graber et al. (1996), and presented in Section 2.1, it is possible to obtain estimates of U_z, the wind speed at a particular reference height, z, from u*.

Although the friction velocity, u*, is a vector quantity, in the literature, this term is frequently used to refer only to the scalar magnitude of the friction velocity vector. Also, as discussed in Chapter 2, the direction of the wind vector and the friction velocity vector are not necessarily coincident. Ideally, we would like to use the direction of the friction velocity vector θ_{u*} in this research. However, at this time, there does not exist a satisfactory model for θ_{u*}. We therefore use u* and θ_{wind} as the two primary input variables to the ASM. This is equivalent to assuming that the dominant wave direction is aligned with the wind direction.

For each pair of input parameters, the ASM generates an estimate of the directional ocean wave spectrum, $\Psi(\mathbf{k},\theta)$; $\mathbf{k}$ denotes the magnitude of the wave number vector and θ denotes its clockwise direction with respect to North (as with a compass). Note that several wave spectrum models are defined such that $\theta=0°$ in the down wind direction. This output from the ASM, $\Psi(\mathbf{k},\theta)$, is the primary input to the composite surface scattering

model. Other inputs are the radar parameters and the observational geometry. The scattering model estimates the radar backscattering cross section, σ^0, that would arise from the ocean surface specified by $\Psi(\mathbf{k},\theta)$. From this two step process, for a particular choice of the input parameters, we obtain a prediction of σ^0. For each region of the ocean surface corresponding to an ERS-1 resolution cell (which is approximately 50 km on a side), we obtain a trio of σ^0 predictions: one corresponding to the viewing geometry of the fore beam, one for the mid beam and one for the aft beam. The final components needed for this scheme are the radar scatterometer measurements obtained by the three beams of the ERS-1 AMI.

The environmental variables we seek to determine by means of this scheme are u* and θ_{wind}, both of which are generally unknown on the open ocean. However, in order to generate a prediction of $\Psi(\mathbf{k},\theta)$ using the ASM we need an estimate of these parameters. This suggests that we may need to apply an iterative technique in order to solve for u* and θ_{wind}. The technique we have chosen to pursue is briefly summarized here and is described in detail in subsequent sections.

The approach we use takes advantage of *a priori* knowledge of the two variables that we seek to determine. For example, we know that θ_{wind} will always be within $[0,2\pi]$ and that u* will almost certainly be within [0.01,1.0], say. We consider all possible combinations of these two variables within the above limits and generate a model prediction of σ^0 for each hypothetical condition. For each σ^0 prediction, we evaluate a measure (called the cost function) of the degree to which the model prediction deviates from the measurements. Ideally, the model predictions of σ^0 will most closely resemble the ERS-1 σ^0 measurements when the model inputs correspond to the prevailing conditions in the

region. To verify that the minimal discrepancy between model predictions and measurements occurs when the prevailing conditions are used as model inputs, we restrict the initial implementation of this technique to the vicinity of NDBC buoys, where u* and θ_{wind} measurements are available for model validation.

This measure of the deviation between the model predictions and the measurements is often referred to as a 'cost function', 'objective function' or 'penalty function'. An objective function is a single measure of 'goodness' of a solution, which depends in some way on the variables used in the problem (Gill et al., 1981). In the context of an optimization problem, the cost function represents an undesirable property that one wishes to minimize, such as the discrepancy between the model predictions and the data. Cost functions often arise within the context of 'Data Assimilation' schemes. Data Assimilation refers to a set of techniques often used in the atmospheric and oceanic sciences that combine physical models with data. It encompasses estimation theory, sequential estimation (Kalman filters), as well as variational and statistical methods (Ghil and Malanotte-Rizzoli, 1991). Using these tools, data assimilation techniques seek to identify the 'optimal blend' between model predictions and observations.

In Section 4.2 we will briefly summarize some relevant data assimilation techniques. Section 4.3 presents an analysis in which we investigate the relationship between retrieval performance and the model parameters of the ASM. In particular, we focus on the impact of different choices for the parameter α used in the model for the high wave number regime. In section 4.4, we present several examples illustrating the application of this technique. We also include a brief discussion of the performance of this friction velocity retrieval scheme in Section 4.4. Section 4.5 suggests some applications to which this scheme could be applied in the future, and finally our conclusions are presented in Section 4.6.

4.2 DATA ASSIMILATION OVERVIEW

There are many data assimilation techniques that blend observational data with mathematical or physical models of atmospheric and oceanic phenomena. Which of these techniques is appropriate depends on the nature of the problem to be solved as well as the available data. Two excellent and comprehensive references on this subject are Daley (1991) and Ghil and Malanotte-Rizzoli (1991).

In the field of meteorology, data assimilation research has been evolving for decades, beginning with the pioneering work of Panofsky (1949), Charney et al. (1950) and Eliassen (1954). One of the results of these efforts was the quantitative numerical estimation technique known as objective analysis. This technique made it possible to use automated mathematical methods in weather analysis, complementing or replacing the graphical interpolation of observations (Ghil and Malanotte-Rizzoli, 1991). By the late 1960s, sophisticated data assimilation tools known as four-dimensional space-time continuous data assimilation were developed and implemented. These techniques took advantage of the data acquired by space-borne observing systems and increasingly powerful computing capabilities. In this type of data assimilation scheme, model forecasts for a set of atmospheric fields are continuously updated, incorporating new observations as they become available (Ghil and Malanotte-Rizzoli, 1991, Charney et al. 1969). Oceanographic applications of data assimilation techniques are considerably more recent (Wunsch, 1996), largely because observations have traditionally been much more sparse.

The starting point for our discussion of data assimilation methods will be optimization techniques, as this is frequently the means by which data assimilation schemes obtain the desired 'optimal blending' of observations and theoretical models. The simplest optimization problem is referred to as unconstrained minimization. If we wish to obtain the

minimum of an univariate function f, without imposing any constraints, we require the following conditions. First, f must be everywhere twice continuously differentiable. In addition, in order for a local minimum of f to exist at a finite point x*, the following two conditions must hold:

$$f'(x^*) = 0 \tag{4.1a}$$

and

$$f''(x^*) \geq 0. \tag{4.1b}$$

Let us define f for the problem at hand. It can be given by

$$f=(\sigma^0_{measured} - \sigma^0_{predicted})^2. \tag{4.2}$$

In this case, since $\sigma^0_{measured}$ is constant for a given resolution cell, $f=f(\sigma^0_{predicted})$. The variable $\sigma^0_{predicted}$ is a function of both u*, and θ_{wind}, however, so the objective function to be minimized is multivariate, i.e. $F=f(u^*,\theta_{wind})$. An unconstrained minimization problem in n dimensions can be specified as

minimize F(**x**) where **x** is in $\mathbf{R}^N$. (4.3)

As in the univariate case, there is a set of necessary conditions for **x*** to be a local minimum; they are the vector analogues of (4.1a) and (4.1b). First, **x*** must be a stationary point (i.e. the gradient vector of F evaluated at the point **x*** must be equal to zero). In addition, the Hessian matrix of F, evaluated at the point **x*** must be positive semi-definite (i.e. all the eigenvalues of the symmetric matrix H(**x***) must be non-negative, where H is the Hessian of F, which is the matrix of the second derivative of F). The definitions and derivations for these conditions are discussed in detail in Gill et al. (1981).

Let us now rewrite our objective function, F, in terms of the variables of interest to this particular problem and using vector notation. We will denote a vector of ERS-1 σ^0 measurements by **O**, and let the σ^0 predictions be given by **M**. In addition, we will define

a set of weights, **W**. These weights can be assigned based on any of several considerations, such as the degree of uncertainty associated with the σ^0 measurements (Wunsch, 1996). Both the observations, **O**, and the model results ,**M**, trace out some trajectory in space. If we assume that the observations are representative of the real phenomenon of interest then it is meaningful to consider a measure of the distance between the two trajectories given by the model predictions and the observations. This distance metric, which can be taken to be an inner product, is our cost function, and is denoted by **J**. That is,

$$\mathbf{J} = \left\langle (\mathbf{O}-\mathbf{M})^{\mathrm{T}} \mathbf{W} (\mathbf{O}-\mathbf{M}) \right\rangle . \tag{4.4}$$

The trajectories of **O** and **M** will depend on the initial conditions and boundary conditions of the two systems, and in the case of **M**, upon the free 'tunable' parameters of the system. In general, we can assume that the 'best' estimates of the initial conditions, boundary conditions and free parameters of the numerical model **M** will be those which best agree with the observations and will be those that minimize **J**.

If one wishes to minimize **J** subject to a physical constraint, then this suggests the application of 'variational analysis' or 'adjoint methods', so-called because they require the solution of the adjoint equations of the linearized model equations (Moore, 1991). Variational analysis is a technique derived from the calculus of variations and optimal control theory that is attributed to Sasaki (1958, 1970). In variational analysis, while changes are being made to the vector of model predictions, minimizing its distance in a least squared sense from the measurement vector, the result is simultaneously being required to satisfy additional physical constraints, either locally or else integrated over the domain (Sashegyi and Madala, (1994)).

Two examples of dynamic constraints that could be applied to this problem are geostrophy (Daley, 1991) and smoothness (Thacker, 1988). For example, if in addition to

the system of models implied by our least squares cost function, (Equation (4.4)), we required our model equations to satisfy the constraint

$$\mathbf{DM=0}, \tag{4.5}$$

where **D** denotes the finite difference operator, which numerically estimates the first derivative of the elements of the matrix **M**, this would change the problem at hand from one of optimization to constrained optimization (Moore, 1991).

In order to approach this problem using the techniques of variational analysis, we would use undetermined Lagrange multipliers as a means of enforcing the model constraints. This is tantamount to defining a new version of the cost function, **J**, which is known as the augmented Lagrange function, **L**:

$$\mathbf{L} = \mathbf{J} + \Lambda^T \mathbf{DM}, \tag{4.6}$$

where Λ is a vector of unknown Lagrange multipliers and **DM**=0 represents the set of hypothetical, dynamical constraints that have been imposed on our system in this example. Clearly, it is important that the model constraints be somewhat simple, analytical models.

By using the Lagrange multipliers, we are able to define a set of new equations known as the adjoint equations. The adjoint equations effectively transform the problem from one of minimizing the model-data misfit into the problem of obtaining the gradient of the cost function with respect to the control parameters. This then amounts to replacing the constrained optimization problem by a series of unconstrained problems, defined with respect to each of the model variables. That is, the problem of minimizing the cost function subject to the model equations can be re-defined as the problem of finding the stationary points of the augmented Lagrange function (Yu and O'Brien, 1991).

The gradient can then be used within an appropriate iterative descent method to search out the optimal estimates of the control parameters (Yu and O'Brien, 1991). Since the minimum of **J** will coincide with a stationary point of **L**, we seek solutions for **M** at such a stationary point. That is, at an extremum of **L**,

$$\frac{\partial \mathbf{L}}{\partial \mathbf{M}} = \frac{\partial \mathbf{J}}{\partial \mathbf{M}} + \frac{\partial \Lambda^T \mathbf{DM}}{\partial \mathbf{M}} = 0, \tag{4.7}$$

where differentiation is carried out with respect to all elements of **M** and **L**. As noted by Moore (1991), although this technique is very promising and powerful, construction of the adjoint model is not trivial and usually requires a great deal of effort.

Variational data assimilation methods, such as those described above, are generally used in time-varying applications. The ERS-1 system, however, only interrogates a given patch of ocean approximately every three days. Therefore, it would be necessary to identify a non-dynamic adaptation of this technique if we wished to apply it to the problem of scatterometer-based friction velocity retrieval. However, we encountered several complicating issues that discouraged us from applying this particular technique. One problem was that it was difficult to find an appropriate set of models to use for constraints. Although we mentioned that 'smoothness' could be used as a model constraint, by itself, it did not provide sufficient benefit to warrant its use. We also cited geostrophy as a candidate constraint, but it is recognized that geostrophy is not a very accurate characterization of the wind field in the atmospheric boundary layer. Alternatively, we hoped to find a model of the wind field at the ocean surface, which was both accurate and simple that we could use as a constraint. We were not successful in identifying a good candidate wind model, however. For example, although the wind field model of Cardone (1970) seemed a good choice for this application, it required knowledge of several environmental variables not readily available within our scheme. In addition, it required more computations than could readily be undertaken within the context of a constrained minimization problem.

An additional source of difficulty was that, in order for us to identify the point corresponding to the minimum of our objective function, we would need to take the derivatives of **J** or **L** with respect to u* and with respect to θ_{wind}. However, the relationship between and the variables u*, θ_{wind} and $\sigma^0_{predicted}$ is indirect; numerous, non-

linear computations must be performed in order to obtain $\sigma^0_{predicted}$ from a given set of input values. That is, it would not be practical to directly compute $\frac{\partial \sigma^0}{\partial u^*}$ and $\frac{\partial \sigma^0}{\partial \theta_{wind}}$ analytically. Although we could approximate the gradient using finite-difference methods, we decided, instead, to pursue an approach that is discussed below. This decision was strongly influenced by extensive discussions with Professor J.-S. Pang of the Johns Hopkins University, an expert in the field of optimization theory.

An additional consideration was the potential impact of modeling and measurement errors on the performance of our chosen optimization technique. For example, modeling errors arise due to the fact that many of the physical processes relevant to scattering from the surface of the ocean at centimeter scales are not incorporated in either the ASM or the composite surface model. It was also important to consider the sensitivity of the optimization techniques under consideration to our choice for the initial values of u* and θ_{wind}. Often, the choice of initial values will exert considerable influence over whether a given optimization scheme will converge to a solution at all, or to a realistic solution. Also, even though they are quite small (in the vicinity of 0.2 dB; P. Lecomte, personal communication, (1998)) we must not disregard the potential impact of ERS-1 measurement errors on our friction velocity retrievals. It is worth noting that our cost function is defined in terms of linear units, not in terms of dB.

In the light of all of the uncertainties associated with the various components of our scheme, especially the geophysical model functions, we could only justify using a comparatively coarse technique for minimizing our cost function. The minimization approach which we chose to pursue is often referred to as a pattern search (Pang, (1998), personal communication). Essentially, a pattern search simplifies the minimization by reducing the dimensionality of the problem. A pattern search in two dimensions requires

that one variable be held fixed at some value while the other is varied in the search for a minimum. Once a minimum has been found for the first variable, it is held constant at its minimal value, and the other variable, in turn, is searched for a minimum. This approach, of holding one variable fixed while the other is minimized is undertaken successively until a suitable accuracy criterion is met. It is prudent, once an overall minimum has been found, to plot the error surface generated in the course of minimization. The following sections provide a closer look at our choice of cost function, $J(u^*,\theta_{wind})$, its application in our scatterometer-based friction velocity retrieval scheme, and some factors impacting retrieval performance.

4.3 MODEL PARAMETER ANALYSIS

The preceding sections have provided an introduction to each of the components of our friction velocity retrieval technique: an ocean wave spectral model, a composite surface scattering model, satellite-based measurements of radar backscatter and a cost function. The overall performance of this scheme will depend on the accuracy of each of its components. In this section we return to the subject of Section 2.6, namely, the model form used to characterize the ocean wave spectrum in this research, particularly at high wave numbers. We will examine the impact on our friction velocity retrieval scheme of different choices of the model parameter, α. We present this analysis at this point in our discussion because its results impact the analyses presented in Section 4.4.

The ASM was presented in Chapter 2. It aggregates *in situ* measurements of the ocean wave number spectrum made by an NDBC buoy, at low wave numbers, with Phillips' equilibrium spectral model. The wave number form of this model is provided in Equation 4.8 below. The model parameter, α, serves as a level-matching parameter in this

context. It is determined at the join-point where the buoy measurements and the model are spliced together. At this point, as discussed in Chapter 2, we use an average α that is determined from the ten highest frequency buoy measurements. Although this buoy-based, average α is clearly appropriate to use in the vicinity of the buoy measurements, it is unclear whether or not this value of α is appropriate to apply to the high-wave number regime as well.

One way to investigate this issue is to determine whether the α derived from minimizing the difference between the ocean spectral model and the NDBC buoy measurements, and the α derived from minimizing the difference between model-based radar cross section predictions and ERS-1 measurements, are consistent. In an effort to resolve this question, we implemented a two-segment form of the ASM: one that used buoy measurements for $k < k_{max,buoy}$ (m^{-1}), and a single realization of the equilibrium spectral model for all $k > k_{max,buoy}$ (m^{-1}). The value of α for the entire modeled portion of the spectrum would be determined at the buoy-model join-point.

Here, our primary concern was the one-dimensional model for the power spectral density, i.e.

$$S(k) = \alpha u^* g^{-0.5} k^{-3.5}. \tag{4.8}$$

Therefore, we did not consider the directional variability of either the ASM or of the associated σ^0 predictions, which simplified the analyses considerably. In particular, we implemented a one-dimensional version of our cost function that solved for friction velocity only. For this one-dimensional cost function we restricted consideration to those cases where the antenna look was within 30° of either the up- or the down-wind direction. In addition, since we were not solving for direction in this particular investigation, it was only necessary to consider one antenna at a time.

Using this one-dimensional form of the cost function, we compared 'retrieved' estimates of u*, i.e. the u* solutions obtained by our scheme corresponding to the cost function minimum, with buoy-based measurements of u*. The results of this analysis are summarized in Table 4.1, below. In this table, 'alpha buoy' indicates the buoy-based values for α. The buoy-measured value of u* is indicated in the column denoted by 'u*meas'. The right-most column of this table indicates the estimate of u* derived from our cost function-based scheme.

	alpha buoy	u* meas.	u* pred. -buoy
16-Feb	0.062	0.27	0.15
13-Feb	0.032	0.37	0.2
1-Mar	0.68	0.51	0.1
30-Mar	0.051	0.05	0.16
20-Mar	0.078	0.42	0.1

Table 4.1: Comparison of retrieved and measured values of u* for five cases in which we implemented the one-dimensional cost function that used a two-segment form of the ASM.

From this analysis we observe that if we use the two component form of the ASM described above, and determine the value of α from buoy measurements, the resulting model is almost certainly *not* accurately characterizing the behavior of the spectrum at high wave numbers. We infer this because under all conditions except for very light winds, the cost function minimum occurs at a significantly lower u* than the measured u*. This suggests that for a given value of u*, our model-based predictions of σ^0 will be much higher than the σ^0 values measured by the ERS-1 system, and that this particular two-segment form of the ASM will consistently over-predict spectral levels at high wave

numbers. Therefore, we can not justify using the same value of α for both components, with the possible exception of conditions of light winds.

In Section 2.6, we noted that there was considerable variability in α, both at a given buoy and between buoys at different locations. In addition, in our analysis of the Standard Leopard measurements we observed α to decrease steadily at high wave numbers. Although this apparent trend may be due at least in part to residual Doppler shifting effects that have not been removed from the data, it is likely that the observed trend of decreasing α at high wave numbers would persist even if the all of the Doppler shifting were removed. This observation supports our findings in Table 4.1, above, suggesting that α at high wave numbers is probably lower than α at low wave numbers. All of these results suggest that it is appropriate to use different values for α when modeling the low and the high wave number regimes.

Whereas ideally we would like to develop an expression for α at high wave numbers from *in situ* measurements obtained on the open ocean, there are no open ocean-based measurements of the wave number spectrum over a sufficiently broad range of scales for this purpose. Therefore, it was necessary for us to identify another source of measurements of the air-sea interface, to assist us in determining the best choice of α to use for the high wave number spectral model. ERS-1 scatterometer measurements that are co-located with NDBC buoys provide one readily available source of ocean surface measurements that can be used for this purpose. It should be possible for us to gain at least some limited information regarding the high wave number portion of the spectrum from the scatterometer measurements, which can in turn help us to select the best choice of α to use in the high wave number spectral model.

In order to use scatterometer measurements as a basis for selecting this high-wave number α, we pursued the following approach. First, we assumed a three-component form of the ASM, treating the low, mid and high wave number regimes of the ocean spectrum separately. As with the analyses presented earlier, the lowest wave number portion of the spectrum would be determined by the measurements obtained by an NDBC buoy. The mid- and high-wave number regimes would still be given by a form of Phillips' equilibrium spectral model, but the relationship between these two components would now need to be specified more explicitly.

First of all, it would be necessary to identify a specific range of wave numbers that would be characterized using the 'mid-range' form of the equilibrium spectrum, and to identify a range of wave numbers that would be given by the 'high-wave number' form of this model. Since waves from the mid-range portion of the spectrum are primarily used in the calculation of the mean squared slopes, we selected $k_{cut} = k_{Bragg}/3$ to be the highest wave number to be characterized by the mid range model form. Here k_{Bragg} is the Bragg resonant wave number described in Section 3.4, and the wave number $k_{cut}=k_{Bragg}/3$ is the highest wave number used in computing the mean squared slope of the sea surface in the two scale model. All wave numbers above k_{cut} would be modeled using the high wave number form of the equilibrium spectrum model. For the mid-range of wave numbers, we used the value of α determined from the buoy measurements, using the approach described earlier. For the high wave number regime, however, we faced appreciable problems. This is the regime which exerts the greatest influence over the entire friction velocity retrieval scheme, due to the dominance of Bragg scattering at high wave numbers. However, this is also the regime about which there are the fewest measurements and the greatest uncertainty.

The approach that we took for determining α for the high wave number regime used the one-dimensional form of our cost function that was introduced earlier in this section. We implemented this scheme on nine data sets obtained from two different

locations over a range of wind and wave conditions. We then obtained numerous realizations of our cost function, each of which assumed a different value for α for the high wave number regime ($0.005 < \alpha < 0.1$). For each data set we identified the value of α that resulted in u* predictions closest to the measured values of u* obtained by the buoy. The results of these analyses are summarized in Table 4.2, below.

Occasionally, in order to obtain the optimal agreement with the scatterometer measurements, it was necessary to consider values of α for the mid-range model that differed slightly from the average value determined by the buoy. In these instances, we used a value for α that was within one standard deviation of the average α measured by the buoys, rather than the average value itself. This was within the observed buoy measurement variability discussed in Chapter 2. The cases where this was necessary are indicated in Table 4.2. Rather than 'set by buoy', we indicate the specific value that was used. Using this approach, we determined the best choice of α to use for the high wave number model for each data set.

It is important to note that in this situation we must be willing to accept the possibility of a discontinuity at the transition between the mid- and the high-wave number models. Although intuitively this is undesirable, given that it is preferable not to have a discontinuous model of a physical phenomenon, there are nonetheless several grounds on which we can justify allowing such a discontinuity in our model.

NORFOLK, VA					
	Date	u* measured	alpha low	alpha hi	u* predicted
	8-Apr	0.39	0.04	0.007	0.35
	13-Feb	0.37	set by buoy	0.018	0.5
	1-Mar	0.51	set by buoy	0.0085	0.5
	30-Mar	0.16	0.06	0.06	0.15
YAQUINA, OR					
	Date	u* measured	alpha low	alpha hi	u* predicted
	10-Feb	0.24	0.053	0.01	0.3
	4-Mar	0.45	set by buoy	0.035	0.45
	16-Feb	0.27	set by buoy	0.03	0.3
	20-Mar	0.42	0.066	0.0175	0.35
	7-Feb	0.11	set by buoy	0.06	0.1

Table 4.2: Summary of cost function-based analyses directed at determining the best choice of α for use at high wave numbers.

First, the comparison of our model-based σ^0 predictions with σ^0 measurements are the primary means by which we can characterize the sea surface at high wave numbers. These predictions are subject to the 'filter' of the composite surface model, which provides an incomplete characterization of the complicated processes that govern radar backscattering from the air-sea interface. The ocean spectral model itself is a generalization and hence may provide an incomplete description of the power spectral density of ocean surface waves under certain conditions. This is particularly true at the highest wave numbers under consideration, where we are at the upper limit of the equilibrium range. In addition, processes or variables, which are not explicitly included in the equilibrium spectral model, may be 'lumped' into the parameter α, such as waves that are not at equilibrium due to rising or falling winds. Finally, even at the low wave number cut-point, which is well within the bounds of the equilibrium range, we have observed considerable variability in α. For all of these reasons, we were willing to consider an aggregate spectral model that would include a discontinuity at the beginning of the high wave number regime.

An additional source of difficulty that we faced regarding our choice of α for the high wave number regime was that although we had hoped to be able to identify a systematic relationship between α and some of the other variables, such as the friction velocity, this was not possible. Reasons for this included the limited number of cases included in this study, all of the above-mentioned sources of uncertainty and also the complexity of the phenomena under consideration.

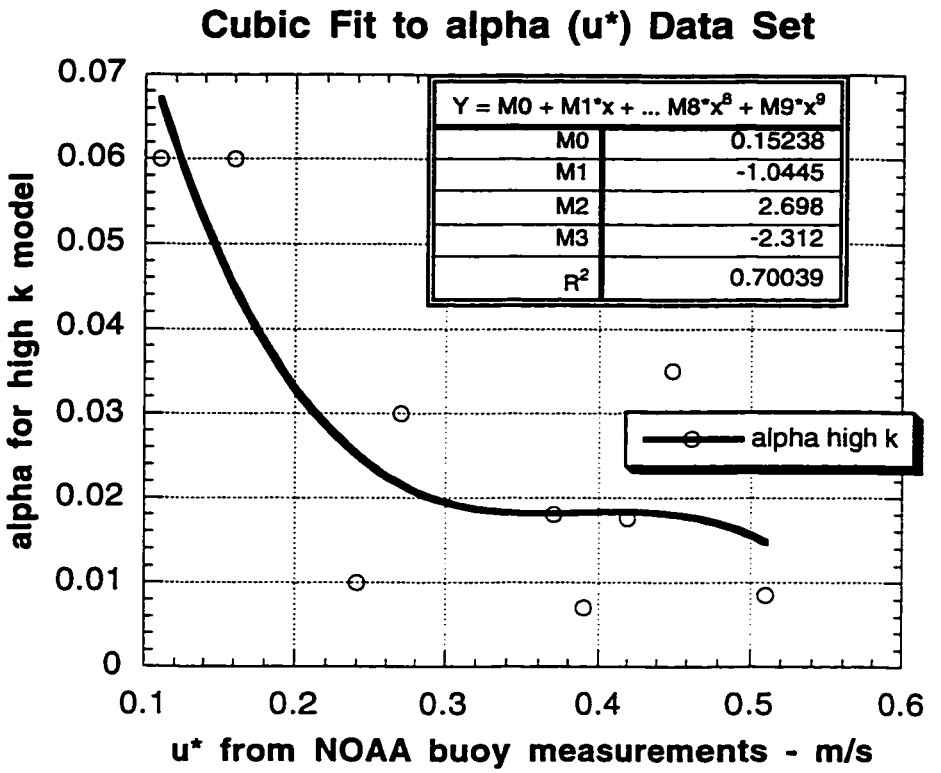

Figure 4.2a: This plot depicts the cubic fit between friction velocity and α for high wave numbers suggested by the data in Table 4.2.

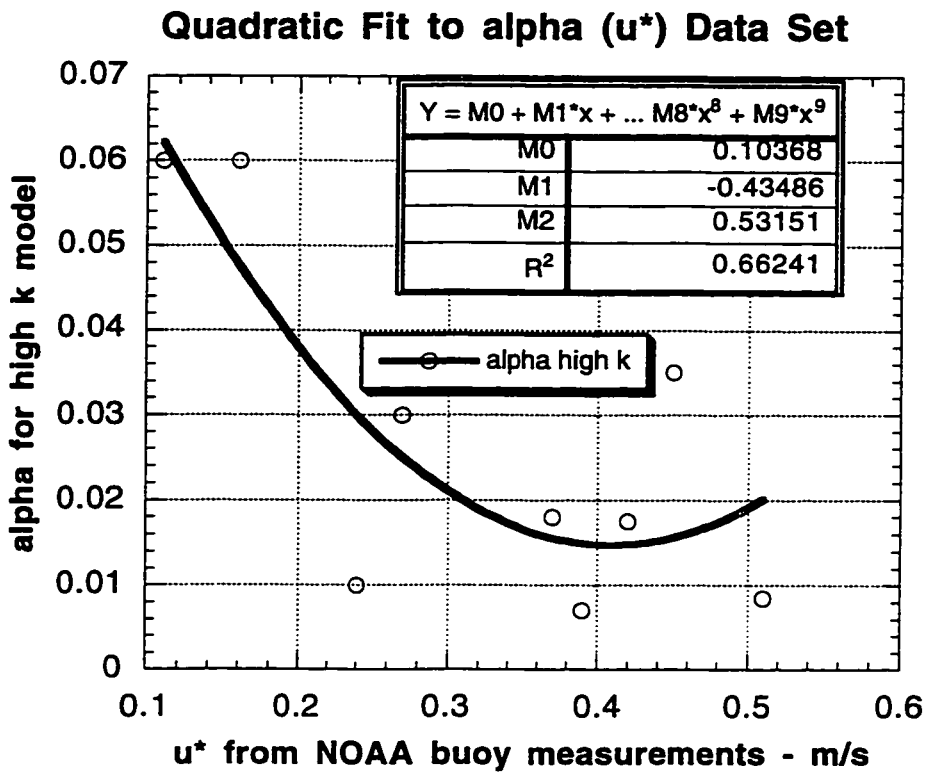

Figure 4.2b: This plot depicts the quadratic fit between friction velocity and α for high wave numbers suggested by the data in Table 4.2.

We were, nonetheless, able to obtain a 'feasibility' analysis, wherein we identified a cubic (4.2 a) and a quadratic relationship (4.2 b) between the friction velocity and the high wave number α, both of which are provided here:

$$\alpha = 0.152 - 1.045u^* + 2.7\, u^{*2} - 2.31\, u^{*3} \qquad (4.9\text{ a})$$

$$\alpha = 0.104 - 0.435u^* + 0.531u^{*2} \qquad (4.9\text{ b})$$

The R^2 statistic is a measure for characterizing the performance of a given model. This statistic expresses the proportion of the variability in the data that can be explained by a particular choice of model. For expression (4.9 a), $R^2 = 0.70$; for expression (4.9 b), $R^2 = 0.66$. Equations (4.9 a and b) suggest that it is possible that α may be related to u^* via either a quadratic or a cubic relationship. However, both of these expressions are only a preliminary step towards modeling or characterizing the parameter α. We have suggested these relationships because they provide a systematic, albeit limited basis for specifying α at high wave numbers when this friction velocity retrieval scheme is used on the open ocean.

Any meaningful approach directed at characterizing α at high wave numbers, however, would require some underlying physical basis. In addition, such modeling efforts would require access to a significantly more comprehensive data set than the handful of cases discussed above. Ideally, in addition to including combined buoy and ERS-1 scatterometer measurements spanning a broad range of wind and wave conditions, these data would also include *in situ* ocean wave measurements at high wave numbers. Such an analysis is well beyond the scope of this thesis. Nonetheless, the above preliminary analyses suggest that the friction velocity retrieval scheme developed in this research could serve as an investigative tool in future research efforts that may lead to a better understanding of some of the physical processes impacting centimeter-scale ocean waves. For example, we may be able to use this approach to investigate the impact of the wind and wave history on the current ocean spectrum.

4.4 COST FUNCTION ANALYSES

The technique developed in this work for retrieving the friction velocity and direction at the ocean surface has been introduced both in the earlier sections of this chapter and also in Section 3.6. One of the central components of this scheme is the cost function. We now provide a closer look at this costs function and examine some of its salient properties as well as some examples. The cost function provides the framework in which the model predictions are compared with the ERS-1 scatterometer measurements; it is by the process of minimizing this cost function that we obtain estimates of the friction velocity and direction at the ocean surface.

The cost function requires that we specify an array of hypothetical environmental conditions that encompasses all possible directions for θ_{wind}, as well as a broad range of values for u*. In the analyses presented in this section, we vary u* from 0.08 m/s to 0.52 m/s in increments of 0.02; we vary θ_{wind} from 0 to 355 degrees in 5 degree increments. Each (u*, θ_{wind}) pair is used as an input to the Aggregate Spectral Model (ASM) which, in turn, generates a two-dimensional ocean wave spectrum. For each spectrum, the directional distribution of wave energy and the level of the power spectral density are explicitly determined by the parameters u* and θ_{wind}. Using the viewing geometry parameters for the ERS-1 resolution cells included in a given analysis, we generate a trio of σ^0 predictions for each of these spectra using the composite surface scattering model. These σ^0 predictions consist of what each of the three beams of the ERS-1 AMI would measure, if each one of these hypothetical conditions were, in fact, the true conditions prevailing at the ocean surface at the time of the ERS-1 over pass.

In Figures 3.9 a – c, presented in Section 3.6, we provided an example of the σ^0 prediction surfaces are obtained by the combined application of the ASM and the composite surface scattering model. For each beam, a surface of σ^0 predictions is generated by considering all possible combinations of u* and θ_{wind} as well as a description of the beam's viewing geometry. In Section 3.6, we noted that as expected, σ^0 increases as u* increases. In addition, we observed that the maximal values of σ^0 occur when the antenna look direction and the wind direction are coincident. Because the composite surface model uses the folded spectrum (defined in Chapter III), all of these plots are, in fact, two copies of a single surface that is defined over $[0,\pi]$.

We will now consider the cost functions obtained by comparing each cell of the σ^0 prediction surfaces with the corresponding ERS-1 σ^0 measurements. The cost function for each individual beam is given by:

$$J(u^*,\theta_{wind}) = (\sigma^0_{predicted} - \sigma^0_{measured})^2/\sigma^0_{measured}. \qquad (4.10)$$

In the cost function, σ^0 is taken in linear units, not in dB. The first cost function example that we will present will continues the analysis of the example presented in Section 3.6. For convenience, in this section we have repeated the plots of σ^0 surfaces that were depicted in Figure 3.9 a – c. These are provided in Figure 4.3 a - c. The cost functions that correspond to these σ^0 surfaces are illustrated in Figure 4.4 a –c.

Although they are all somewhat similar, the cost function for each beam assumes a different shape for the following reasons. The strongest influence on the shape of a given cost function is the absolute difference between the σ^0 predictions and the σ^o observations.

The angle of incidence of a given beam also influences the cost function shape, primarily because the magnitude of both the observations and the predictions increases at shallower incidence angles. For this reason, the mid beam, which is always pointed at a shallower incidence angle than the fore or the aft beams, often assumes a different shape than the other two. Of course, when an anomalous σ^o measurement is encountered for any beam, it significantly impacts the shape of the resulting cost function.

The total cost function is obtained when the individual cost functions for each beam are combined. It is given by:

$$J(u^*,\theta_{wind}) = \Sigma w_f(\sigma^0_{predicted,f} - \sigma^0_{measured,f})^2/\sigma^0_{measured,f} + W_m(\sigma^0_{predicted,m} - \sigma^0_{measured,m})^2/\sigma^0_{measured,m} + W_a(\sigma^0_{predicted,a} - \sigma^0_{measured,a})^2/\sigma^0_{measured,a} \quad (4.11)$$

and is illustrated in Figure 4.5. In Equation (4.11), the subscripts f, m, and a denote the fore, mid and aft beams, respectively. The total cost function is illustrated in Figure 4.5. In this case, we have assumed that the cost function for each beam will contribute equally to the total, i.e. $w_f = w_m = w_a = 0.333$ in Equation (4.11).

We note the following important points regarding the example presented in Figures 4.4 a – c and Figure 4.5. These data were acquired on 4 March 1993, in Yaquina Bay Oregon. The location of this buoy is indicated in Figure 2.1, and a general description of this buoy and its location are provided in Section 2.4.

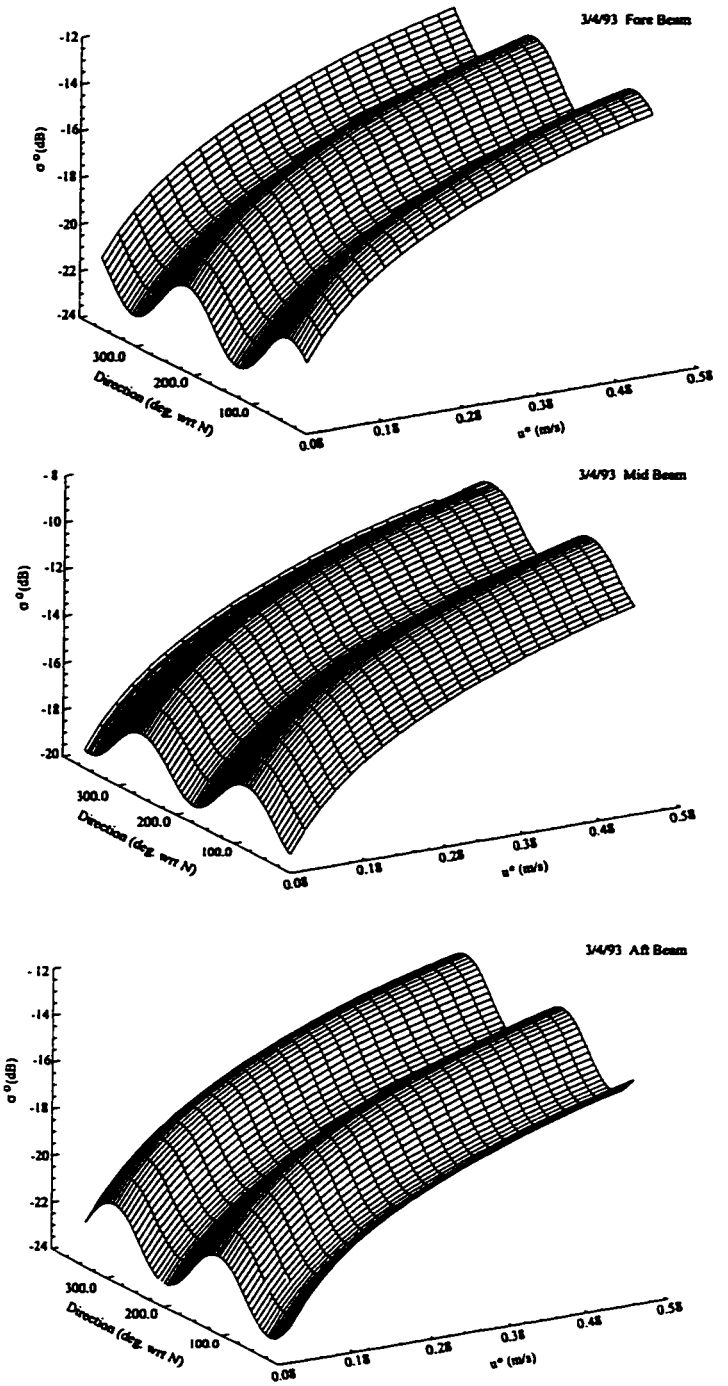

Figure 4.3: σ^0 prediction surfaces obtained using ASM and composite surface scattering model for 3/4/93. Additional information regarding this case is provided in Figure 3.9.

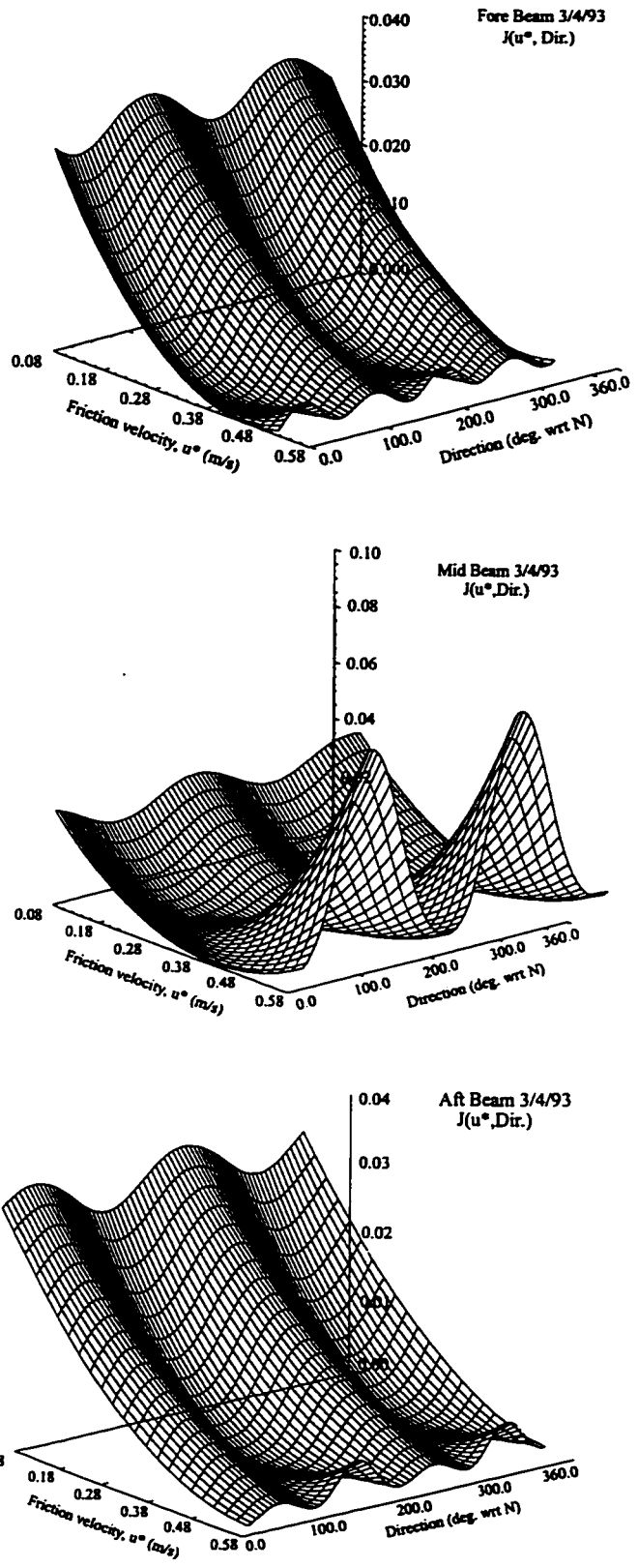

Figure 4.4: Cost functions for the fore, mid and aft beams for 3/4/93. The incidence angles are: 56.9°, 45.4° and 56.8°, respectively. The azimuth angles are 215.1°, 216.1° and 307.2°, respectively.

The wind direction measured by the buoy was 305°; the direction corresponding to the cost function minimum was 340°. In this case, the friction velocity estimate determined by the buoy was 0.45 m/s; the friction velocity corresponding to the cost function minimum was 0.44 m/s. To identify the location of the estimated solution for the friction velocity and the wind direction it is necessary to consider the combined cost function depicted in Figure 4.5. In this case, the friction velocity and direction corresponding to the cost function minimum are quite close to those determined by the buoy.

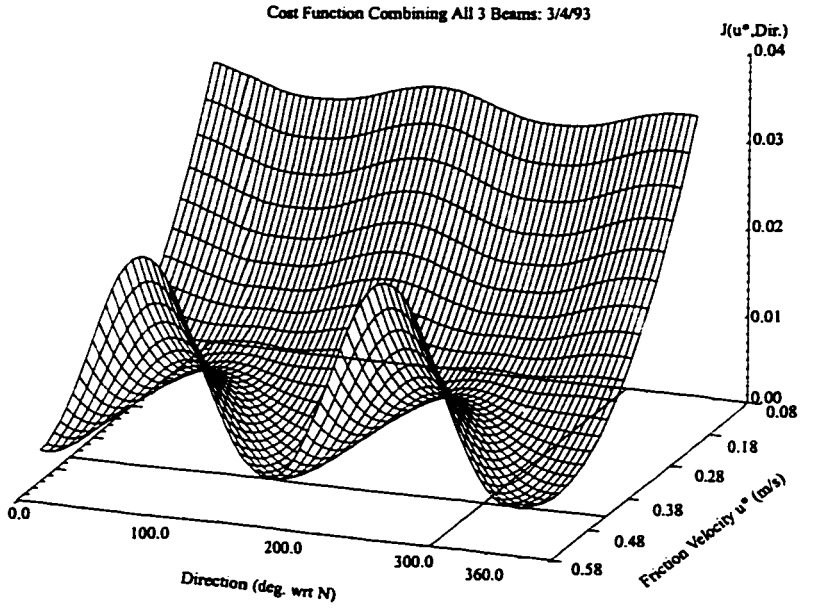

Figure 4.5: Illustration of the cost function combining all three beams, 3/4/93. The graph has been rotated relative to the depiction of the three individual cost functions in order to make it easier to see the behavior of the cost function in the vicinity of the minima. The lines on the plane J=0 indicate the location of the 'true' friction velocity and direction.

Table 4.3 presents a summary of the results of the retrievals considered in this section, and the corresponding environmental conditions. Four of the analyses presented in this table are from Yaquina Bay, OR. At this location, the friction velocity varied between u*~0.11 and u*~0.44; this corresponded to wind speeds between 3.3 m/s and 10.1 m/s. The other analyses were for a location off the coast of Norfolk, VA. At this location, the friction velocity varied between u*~0.16 to u*~0.51; this corresponded to wind speeds between 6.3 m/s and 11.3 m/s. In cases where the incidence angle was too shallow, it was not possible to obtain a complete retrieval because there was not an acceptable prediction of σ^0 for each of the three beams.

Yaquina OR	u* measured (m/sec)	u* retrieved (m/sec)	wind dir meas. (degrees wrt N)	wind dir. ret. (degrees wrt N)	Remarks
20-Mar	0.42	0.52	246	185	falling winds: 12 - 9 m/s
4-Mar	0.45	0.44	305	340	
16-Feb	0.27	0.22	55	55	
10-Feb	- -	- -	- -	- -	mid beam non-Bragg
7-Feb	0.11	0.14	135	145	
Norfolk VA	**u* measured (m/sec)**	**u* retrieved (m/sec)**	**wind dir meas. (degrees wrt N)**	**wind dir. ret. (degrees wrt N)**	**Remarks**
8-Apr	- -	- -	- -	- -	mid beam non-Bragg
30-Mar	0.16	0.1	305	335	
1-Mar	0.51	0.52	324	295	
23-Feb	- -	- -	- -	- -	rising winds: 3 - 6 m/s
13-Feb	0.37	0.28	220	230	

Table 4.3: Summary of friction velocity retrieval performance results.

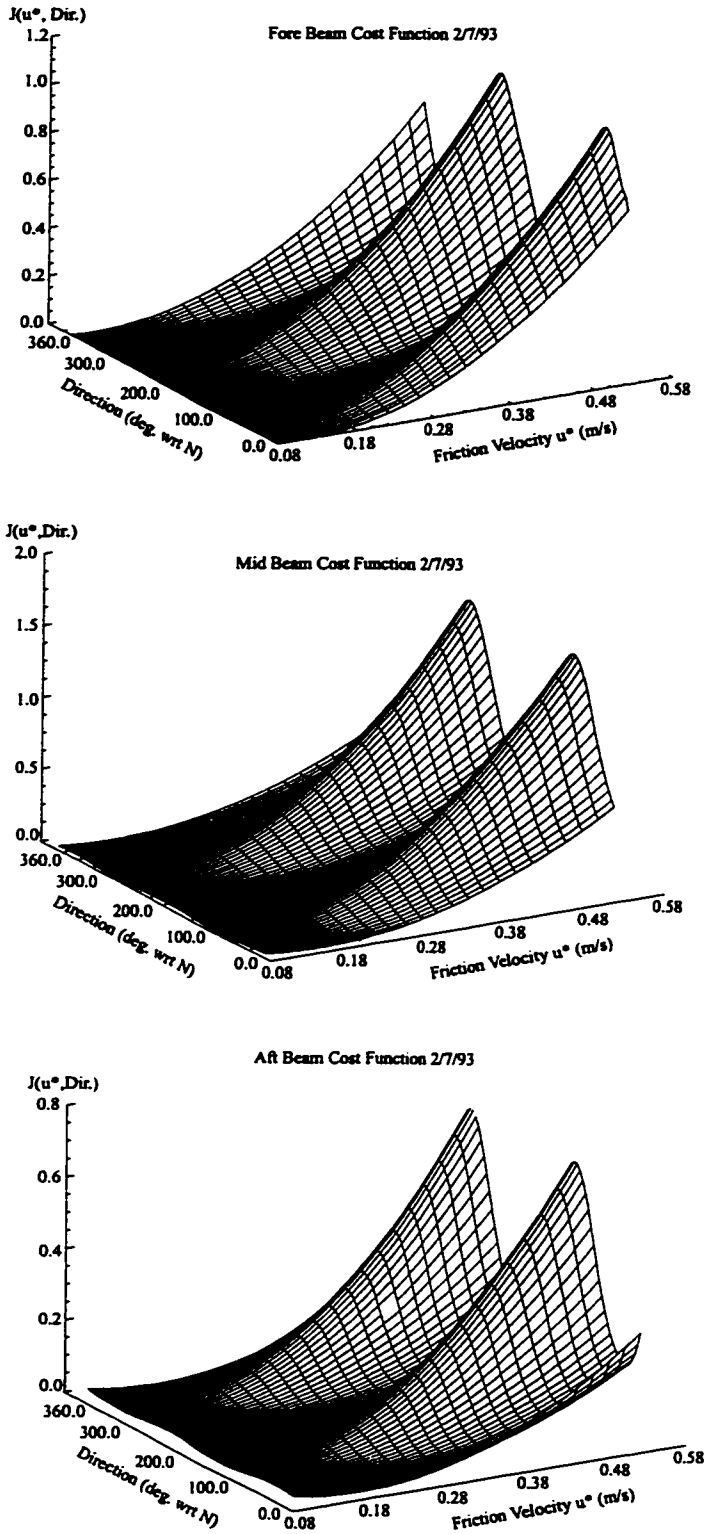

Figure 4.6: Cost functions for the fore, mid and aft beams for 2/7/93. The incidence angles are: 40.3°, 30.2° and 40.1°, respectively. The azimuth angles are 55.3°, 101.1° and 146.5°, respectively.

The conditions of atmospheric stability and the wind directions at the analysis times are included in the table. This table is a companion to Figures 4.4 - 4.14, which illustrate the behavior of the cost function by beam as well as the total cost function, for each of the data sets included in this study. These figures, in particular those that illustrate the three-beam aggregate of the cost function, enabled us to visually assess the performance of this friction velocity retrieval scheme, whereas Table 4.3 presents a more quantitative means of assessing the retrieval scheme performance. In this table, in addition to a summary of the above-mentioned environmental conditions, we compare the buoy-estimated values of u* and θ_{wind} with those obtained from our retrieval scheme.

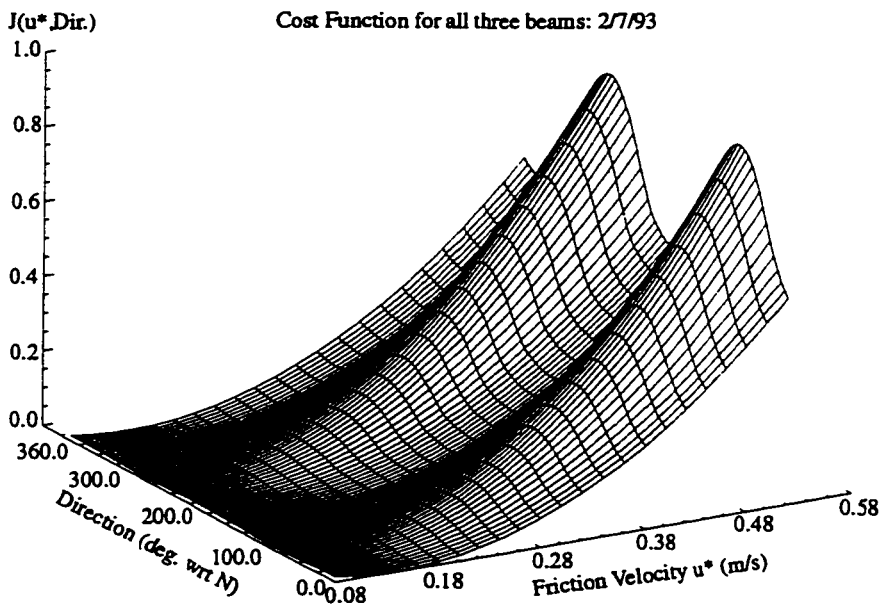

Figure 4.7 a : Illustration of the cost function combining all three beams for 2/7/93.

Figure 4.6 depicts the cost function for the three beams corresponding to the ERS-1 over pass of Yaquina Bay, Oregon on 2/7/93. Figures 4.7 a and 4.7 b depict the cost function that aggregates all three beams for this date. In these figures, particularly Figure 4.7 b, we can see that the cost function minimum occurs at u* = 0.14 m/sec, whereas the buoy –based estimate is u* = 0.11 m/sec. The direction corresponding to the cost function minimum is 145°, whereas the wind direction measured by the buoy is 135°. In this instance, the retrieved friction velocity is within 27 percent of the measured friction velocity and the retrieved direction is within 10° of the measured wind direction.

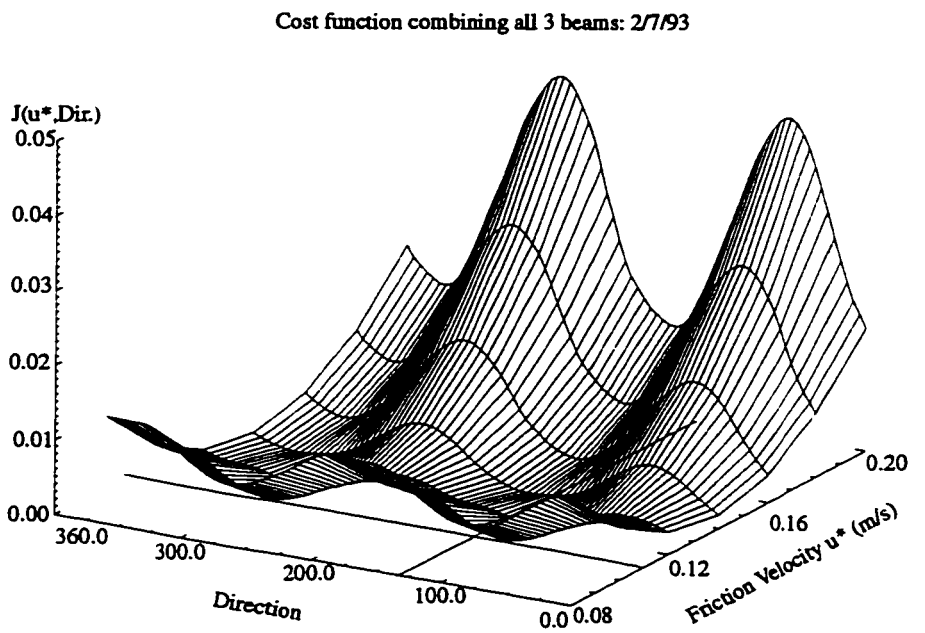

Figure 4.7 b: Total cost function for 2/7/93, close-up view indicating location of cost function minimum. Plot has been rotated to make it easier to see the behavior of the cost function in the vicinity of the solution.

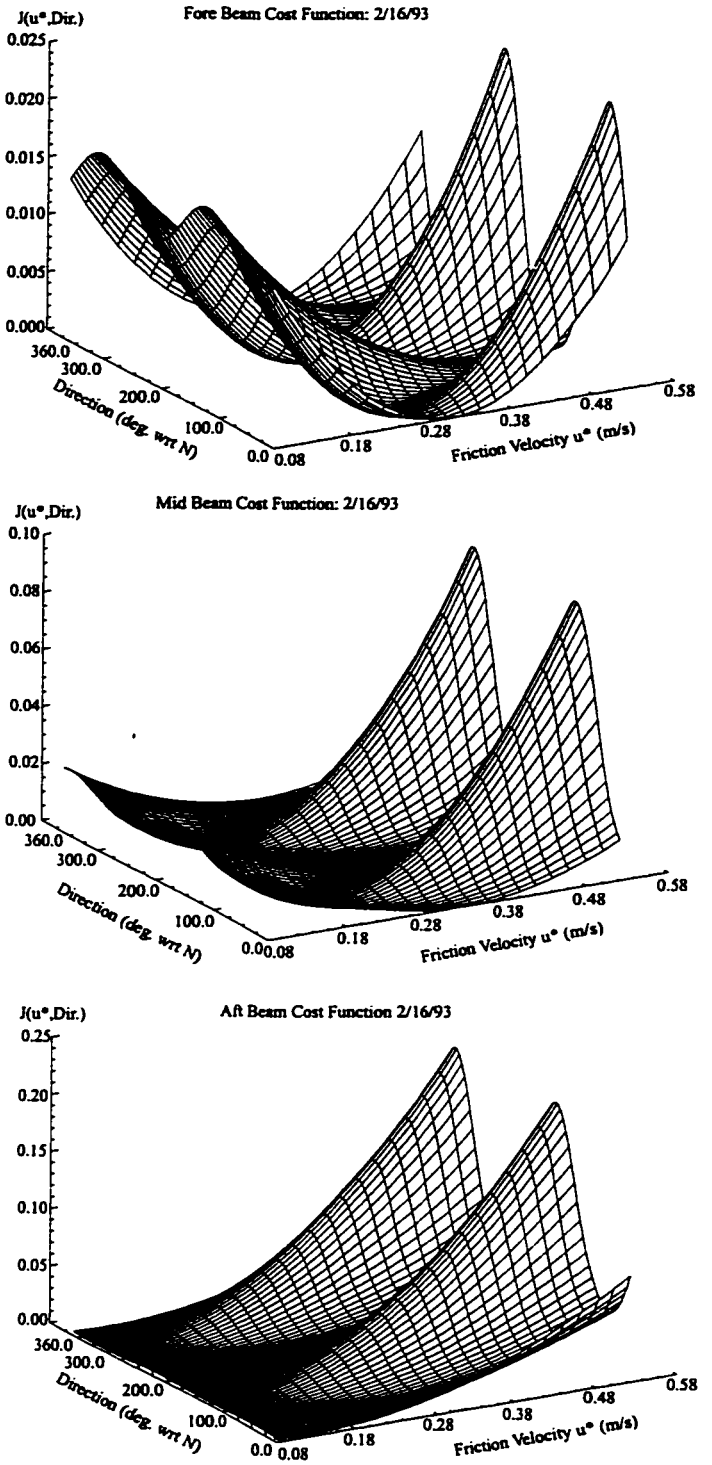

Figure 4.8: Cost function for the fore, mid and aft beams for 2/16/93. The incidence and azimuth angles for each beam are, (56.9,215.1), (45.4,261.2) and (56.8,307.2), respectively.

Figure 4.8 depicts the cost function for the three beams corresponding to the over pass of Yaquina Bay, Oregon that took place on 2/16/93. Figure 4.9 depicts the cost function for this date that aggregates all three beams. From these figures, we can see that the cost function minimum occurs at u* = 0.22 m/sec. The buoy –based estimate is u* = 0.27 m/sec. The direction corresponding to the cost function minimum is 55°, and the wind direction measured by the buoy is 55°. In this instance, the retrieved friction velocity is within 19 percent of the measured friction velocity and the retrieved direction is identical to the measured wind direction.

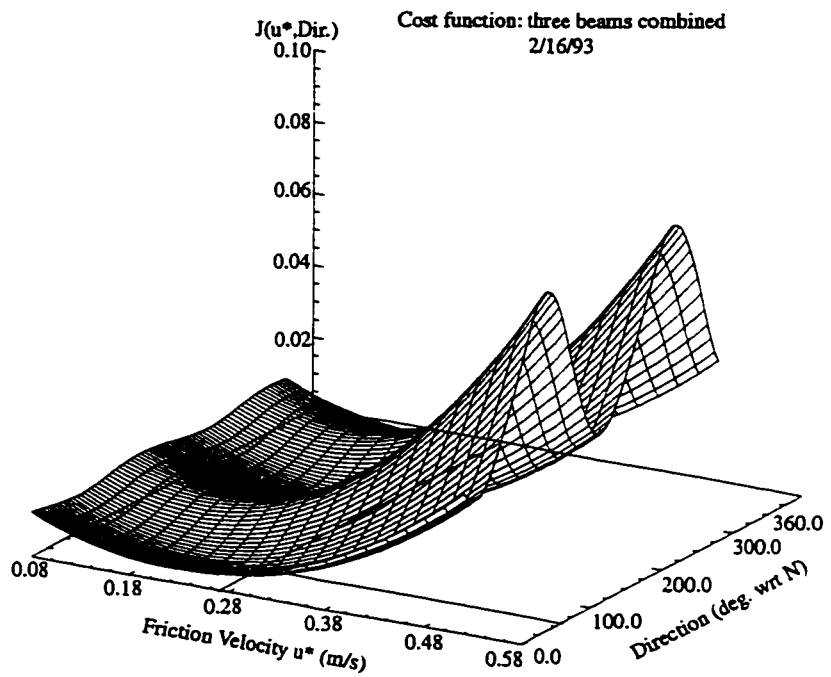

Figure 4.9: Cost function combining all three beams for 2/16/93.

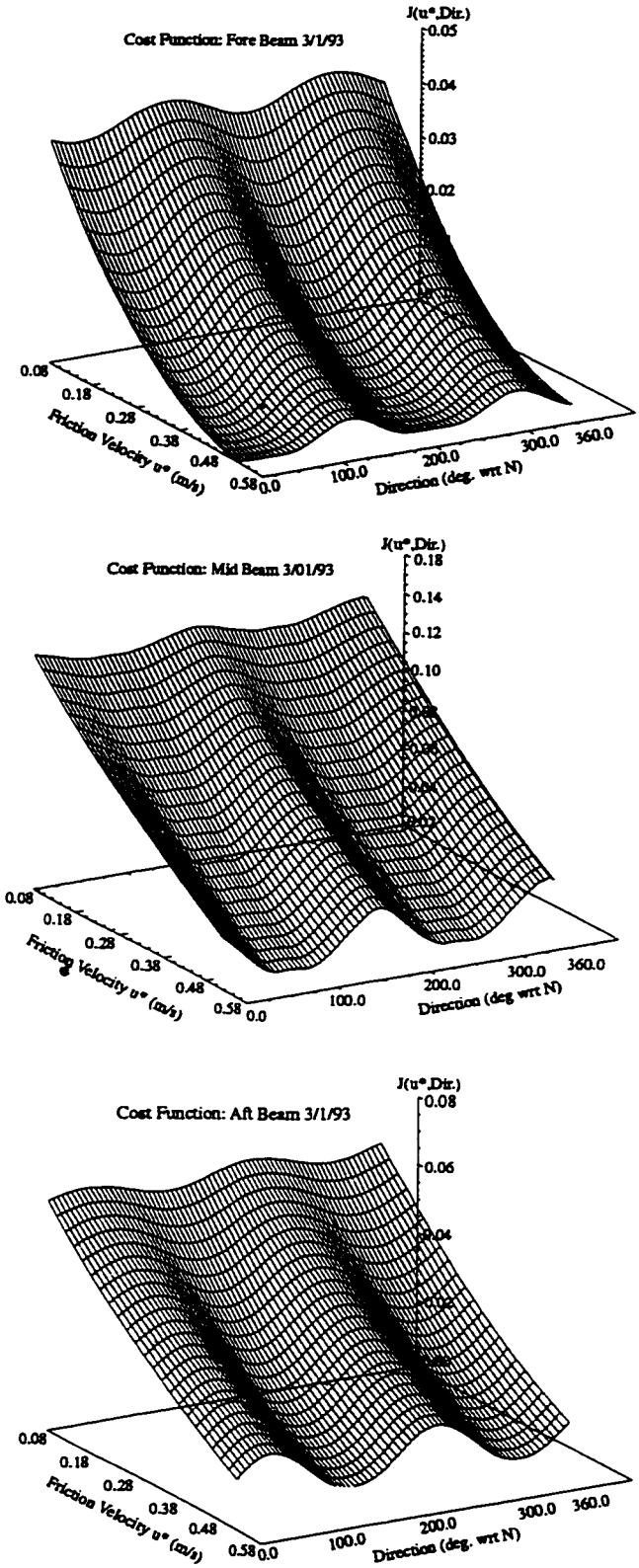

Figure 4.10: Cost function by beam from 3/1/93: Incidence and azimuth angles for each beam are: (50.3,214.3),(39.1,260.1) and (50.2,305.9), respectively.

Figure 4.10 depicts the cost function for the three beams corresponding to the over pass of Norfolk, Virginia that took place on 3/1/93. Figure 4.11 depicts the cost function that aggregates all three beams for this date. From these figures, particularly Figures 4.11, we can see that the cost function minimum occurs at u* = 0.52 m/sec. The buoy –based estimate occurs at u* = 0.51 m/sec. The direction corresponding to the cost function minimum is 295°, whereas the wind direction measured by the buoy is 324°. In this instance, the retrieved friction velocity is within 19 percent of the measured friction velocity and the retrieved direction is within 30° of the measured wind direction.

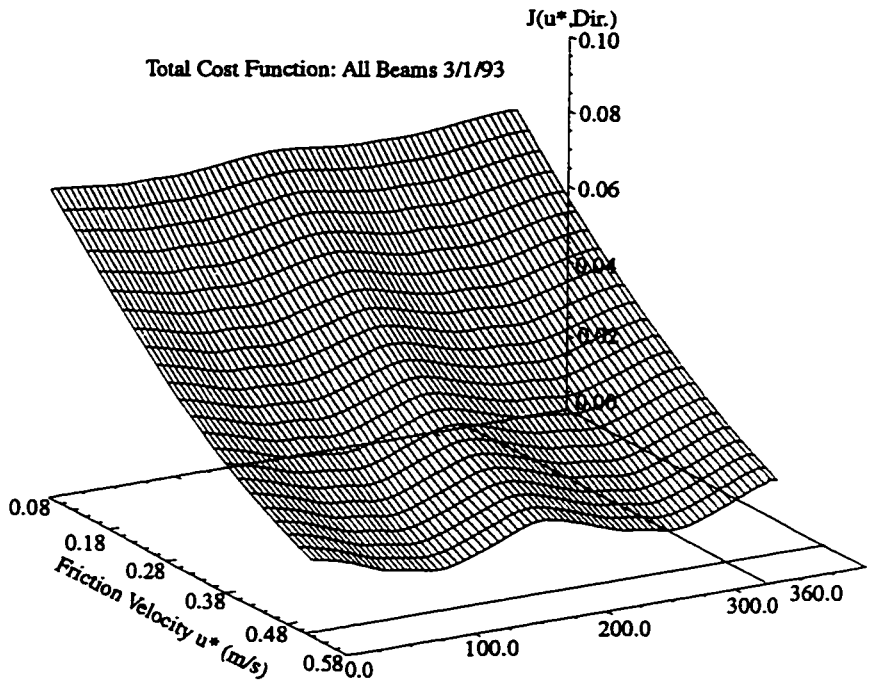

Figure 4.11: Cost function combining all three beams for 3/1/93.

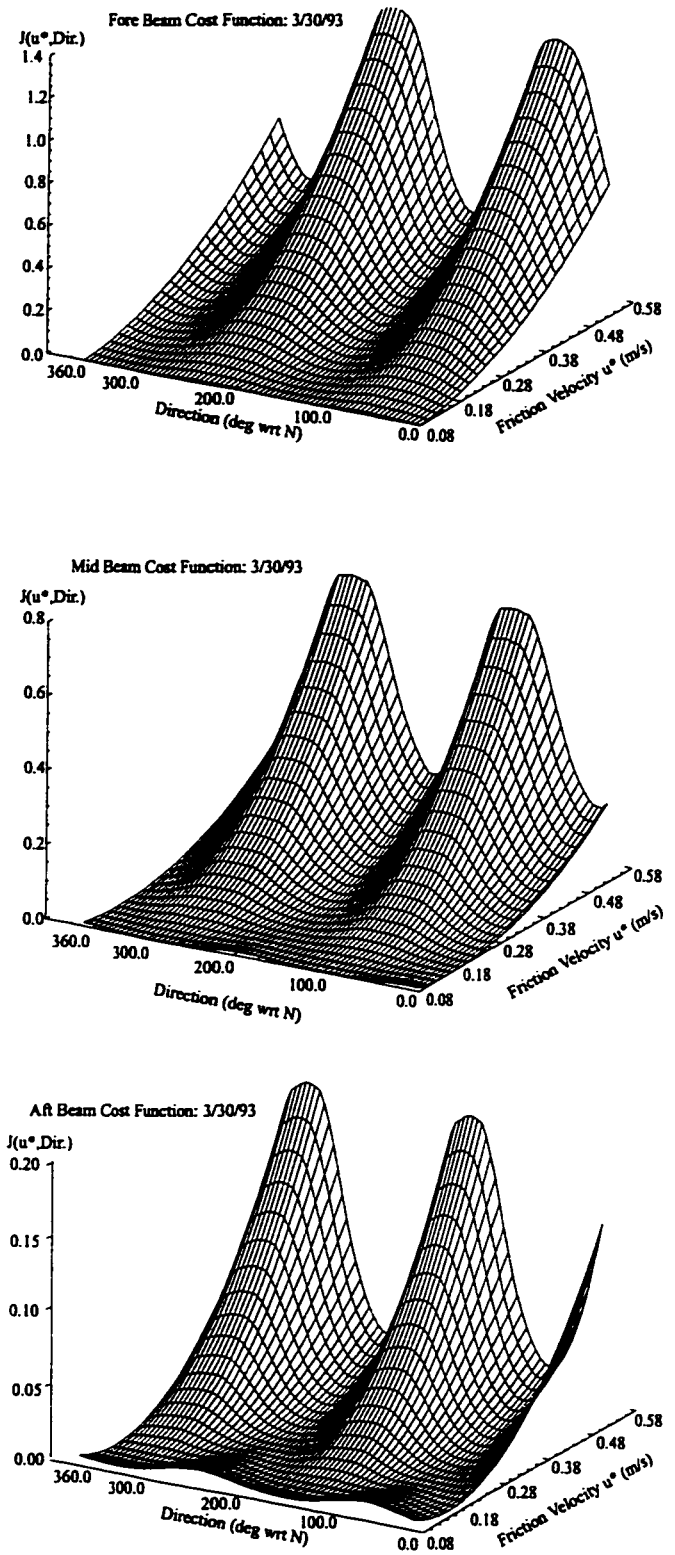

Figure 4.12: Cost function by beam for 3/30/93: Incidence and azimuth angles for each beam are, (56.8,53.4), (45.4,99.4) and (56.8,145.2), respectively.

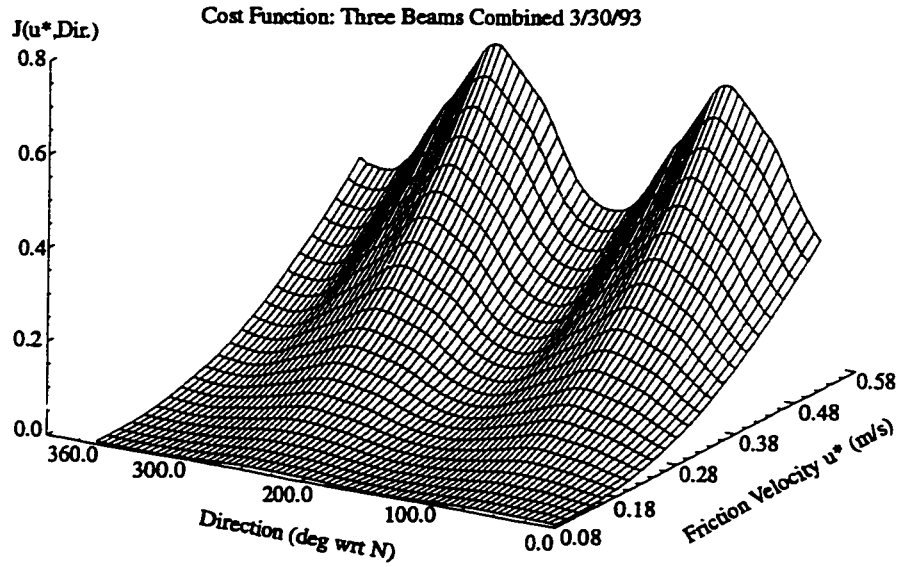

Figure 4.13a: Total cost function combining all three beams for 3/30/93.

Figure 4.12 depicts the cost function for the three beams corresponding to the over pass of Norfolk, Virginia from 3/30/93. Figures 4.13 a and 4.13 b depict the cost function that aggregates all three beams for this date. From these figures, particularly Figure 4.13 b, we can see that the cost function minimum occurs at u* = 0.16 m/sec. The buoy –based estimate occurs at u* = 0.1 m/sec. The direction corresponding to the cost function minimum is 335°, whereas the wind direction measured by the buoy is 305°. In this instance, the retrieved friction velocity is within 38 percent of the measured friction velocity and the retrieved direction is within 30° of the measured wind direction.

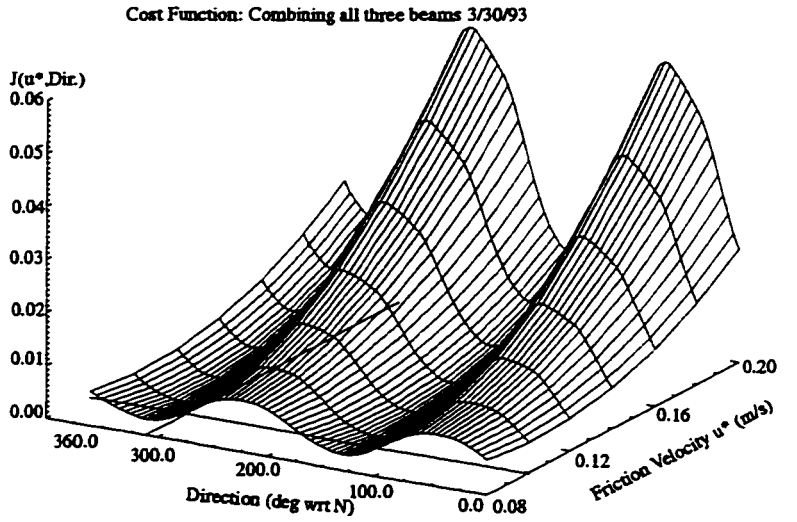

Figure 4.13b: Close-up view of the total cost function depicted in Figure 4.13a for 3/30/93.

Figure 4.14 depicts the cost function for the three beams for the over pass that occurred off the coast of Norfolk, VA on 2/13/93. Figures 4.15 depicts the cost function that aggregates all three beams for this date. In these figures, particularly Figure 4.15, we can see that the cost function minimum occurs at $u^* = 0.28$ m/sec. The buoy –based estimate occurs at $u^* = 0.37$ m/sec. The direction corresponding to the cost function minimum is 230°, whereas the wind direction measured by the buoy is 220°. In this instance, the retrieved friction velocity is within 24 percent of the measured friction velocity and the retrieved direction is within 10° of the measured wind direction.

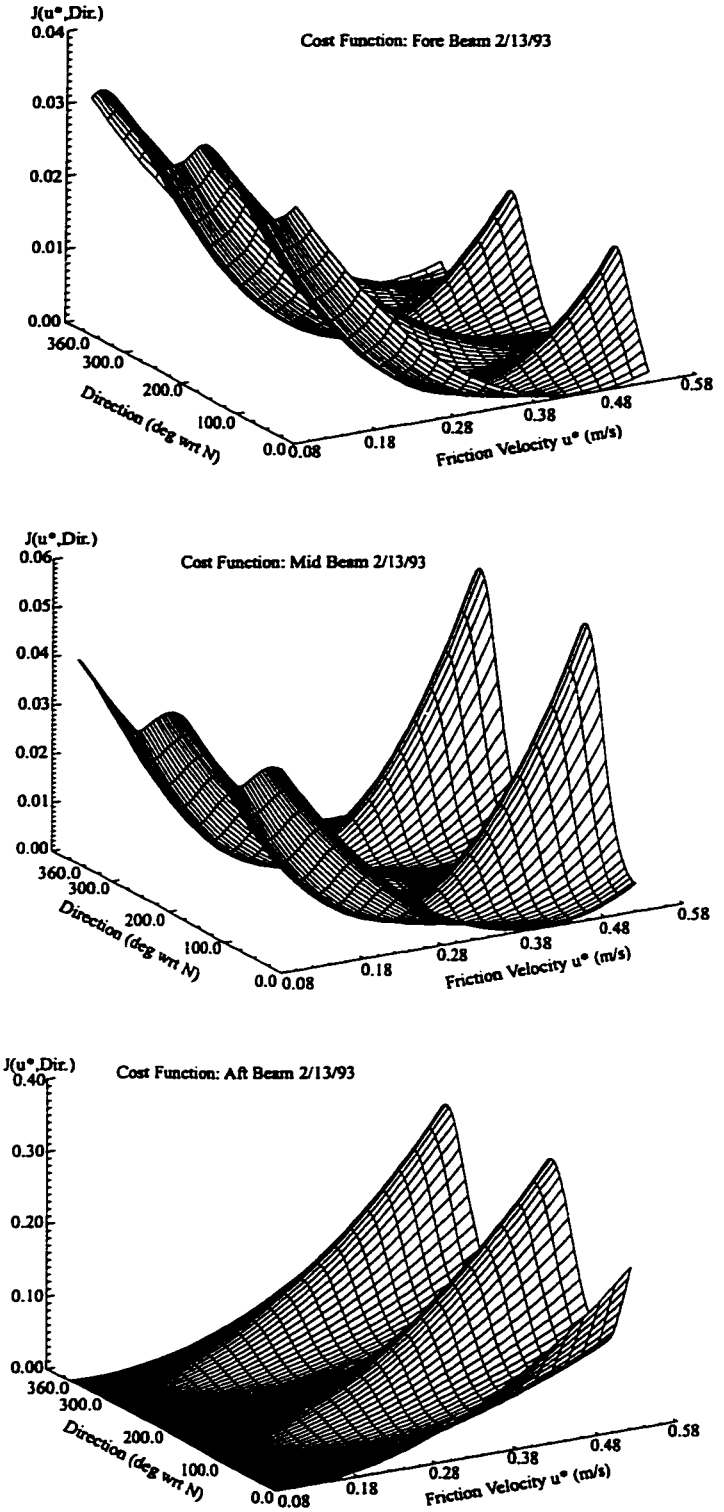

Figure 4.14: Cost functions for 2/13/93. The incidence and azimuth angles by beam are, (42.,55.3), (101.1,31.8) and (42.0,146.5), respectively.

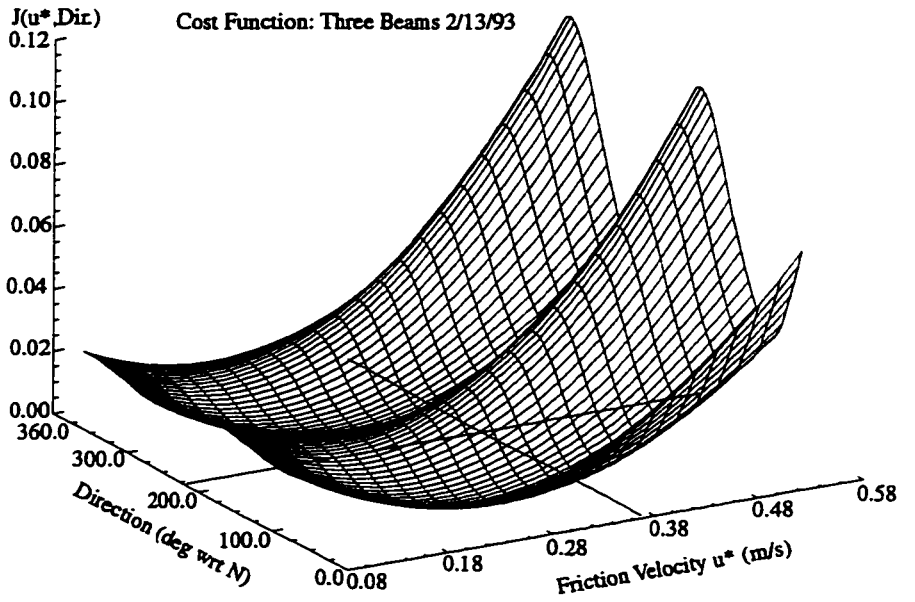

Figure 4.15: Total cost function for 2/13/93, combining over all beams.

The preceding results illustrated the implementation of our friction velocity retrieval scheme when applied to an individual resolution cell within a given region. To evaluate whether the friction velocity retrieval performance varied appreciably from cell-to-cell at a particular location, we performed the following analyses. We compared the friction velocity and direction estimates obtained by our scheme for four different resolution cells that were selected at random (subject to the requirement that $\theta_{IA} > 25°$, to ensure that we were well within the Bragg scattering regime) in the vicinity of Yaquina Bay, OR, 2/13/93. We observed negligible variability in these results, which is consistent with the ERS-1 AMI specification of accuracy within +/- 0.2 dB (P. Lecomte, personal communication, (1998)).

Ideally, in order to characterize the viability of our friction velocity retrieval scheme, we would obtain several friction velocity retrievals over a range of environmental conditions, at several locations, and making use of many different resolution cells.

Because conditions at the ocean surface can vary greatly, a comprehensive or statistically meaningful set of analyses such as that suggested above would require an extensive effort, well beyond the scope of this effort. Hence, we have presented the results of seven friction velocity retrievals that were obtained at two different locations, that encompassed a broad range of wind and wave conditions.

As a final note, it is important to recognize that retrieval performance depends both on factors that we can control and on those that we can not. Those we can control include cost function weighting schemes, ocean spectral model parameter choices, and on the scattering model parameter choices. Those that we can not control include errors in the ocean wave spectrum, errors in the composite surface scattering model and measurement variability. This final category includes errors in the σ^0 measurements, in the NDBC buoy measurements and also in the original, *in situ* wave measurements. Throughout this analysis we have acknowledged the numerous sources of uncertainty that could potentially impact our results, but only some of these can readily be quantified. For example, it is unclear how to model or characterize the uncertainty associated with the Doppler shift compensation technique discussed in Chapter 2. The best way to address the sources of uncertainty over which we have minimal control is through statistical analyses. For example, with access to additional *in situ* wave measurements, particularly those obtained under a broad range of environmental conditions we could refine and validate the ASM. Certainly, data acquired directly in wave number space would be an extremely valuable component of any model validation efforts. In addition, the retrieval performance should be characterized using a much larger data base. Optimally, such a data base would encompass several locations and have multiple observations, with several observations acquired for a given set of conditions, as well as a range of environmental conditions. Such efforts would be a valuable enhancement to the research presented here, and would strengthen our findings considerably.

4.6 CONCLUSIONS AND RECOMMENDATIONS FOR FUTURE RESEARCH

In this chapter we have discussed the considerations that impacted our choice of data assimilation technique, and examined the particular cost function that we chose to use in this implementation in some detail. We presented friction velocity retrieval results obtained by this scheme under a variety of wind and wave conditions. The cost function scheme that we developed in this research enabled us to investigate some related topics such as the impact of long wave effects on radar cross section prediction and also the choice for the spectral model parameter, α.

An interesting outcome from this research was that this cost function framework, developed as component of our friction velocity retrieval scheme, could also be applied as a general analytical tool to several investigations regarding scattering from the ocean surface. Some potential applications appropriate for future efforts will be discussed here.

The framework of our cost function is modular and flexible. It would be straightforward to expand this scheme to include alternative ocean wave spectral models or electromagnetic scattering models. This modularity would make it possible, for example, to investigate the impact of different ocean surface characterizations or spectral models on friction velocity retrieval performance, similar to the investigations pursued in our model parameter analysis. Similarly, the potential benefits arising from alternative scattering models such as the Integral Equation Model could be readily evaluated using this scheme. In the same spirit of the analyses presented in Chapter 3, this scheme could be applied to investigate more closely the effects on radar cross section due to modulation by the long waves. It could also be used to evaluate alternative cost function forms (i.e. besides weighted mean squared difference) and different choices of beam weightings. These are all important, relevant issues that could be easily explored further using this scheme as a tool.

CHAPTER 5: SYNOPSIS AND CONCLUSIONS

The primary goal of this research is to develop a technique for retrieving the wind friction velocity and direction at the ocean surface by combining radar scatterometer measurements with a physical model of the ocean spectrum and a physical model for predicting electromagnetic scattering from a rough surface. We anticipated that such an approach, in addition to producing viable predictions of the friction velocity and direction at the sea surface, would yield additional physical insight about some of the processes taking place at the air-sea interface, that influence the observed radar signature. In particular, we sought to gain a better understanding of the ocean surface and its response to the wind at scales in the vicinity ERS-1 Bragg scatterers, namely, for ocean waves of wavelengths between 3 and 9 cm. To a large extent, these anticipated results were achieved.

We provide a brief overview of our technique here. The friction velocity retrieval scheme developed in this effort is applied in a particular region of the ocean where ERS-1 measurements are available. In this region, we specify a set of hypothetical friction velocities and directions that span a broad range of allowable values. Associated with each candidate forcing (i.e. friction velocity and wind direction) is a realization of the ocean wave number spectrum which describes the distribution of roughness elements on the ocean surface for the region in question. For a set of radar viewing parameters, the composite surface model generates a trio of radar backscatter predictions for each of these spectra, one corresponding to each antenna beam of the ERS-1 system. Therefore, there is a set of backscatter predictions obtained from these models associated with each resolution cell in a given region. For this same region, we will have a trio of radar backscatter measurements. An error metric or cost function combines these backscatter predictions

with the ERS-1 measurements. A procedure seeking the minimal discrepancy between the measurements and the predictions serves as the basis for identifying the presumed forcing for each resolution cell. The accuracy of these retrievals of the wind stress is verified using National Data Buoy Center (NDBC) measurements that are co-located with the ERS-1 resolution cells.

We now review the important attributes of each of the components of our scheme. First, in its current implementation, this friction velocity retrieval scheme is applied in the vicinity of an NDBC buoy. This is both to assist in validating our results and also to provide an accurate characterization of the wave spectrum at low wave numbers. In the future, this technique will be generalized to use a model for the low wave number spectrum. To characterize the spectra for both the intermediate and the high wave number waves we use the equilibrium spectral model developed by Phillips in 1985. Our decision to use this model was supported by analysis of a new set of high frequency, *in situ* measurements obtained in the Caribbean Sea by researchers at the Johns Hopkins University Applied Physics Laboratory. The wave tank measurements of Jahne and Riemer (1990) and Klinke and Jahne (1992) also support this model choice. We obtained a two-dimensional wave number spectrum using this one-dimensional spectral model in conjunction with spreading functions derived from both remote sensing and *in situ* wave measurements. In summary, the ocean wave spectrum used in this research combines NDBC measured spectra for low wave numbers with Phillips' model at intermediate and high wave numbers. Since it is an aggregation of spectral measurements and models, we refer to this model as the Aggregate Spectral Model.

The second major component of this scheme is a composite surface scattering model. This model is used to obtain predictions of the radar backscatter associated with a given configuration of the air-sea interface suggested by the wave number spectrum estimated by the ASM. We present an example that illustrates the combined application of these two models. In addition, the framework developed as part of this scheme was used

to investigate the difference between the tilted Bragg and the nominal (un-tilted) Bragg scattering models. In this investigation we analyzed a handful of cases spanning a range of wind and wave conditions, and found that long wave effects on radar cross section prediction are on the order of 1 dB.

Finally, we present the basis for how we combine the model results and the scatterometer measurements. We discuss some of the primary considerations underlying our choice of cost function, and briefly mention a few alternative data assimilation techniques that may be appropriate for use in future applications of this scheme. This cost function scheme is successfully used to obtain accurate predictions of the friction velocity and direction at the ocean surface under a variety of conditions, for seven different cases.

We present detailed depictions of the cost functions used in this scheme as well as a summary of the retrieval performance. Overall, we obtained friction velocity retrievals within 22 % of the friction velocity estimates determined by the NDBC buoys. We obtained estimates of the wind direction that were within 25° of the measured wind direction. The friction velocity retrieval scheme developed in this research enabled us to investigate two related topics. First, as mentioned earlier, we were able to obtain a preliminary evaluation of the impact of long wave effects on radar cross section prediction. In addition, we were able to use the technique developed in this research to investigate the impact of varying one of the spectral model parameters on the resultant friction velocity retrievals.

In summary, the technique developed in this research was successful at achieving the following results: (1) We developed a technique for estimating the friction velocity and direction at the ocean surface using radar scatterometer measurements and physical models. (2) We used this technique to estimate the friction velocity and direction at the ocean surface to within 22 % and 25°, respectively. (3) This scheme provided us with a tool for investigating ocean wave model parameters as well as a tool for estimating the impact of long wave effects on a model for predicting Bragg scattering from the ocean surface.

BIBLIOGRAPHY

Apel, J. R., An Improved Model of the Ocean Surface Wave Vector Spectrum and its Effects on Radar Backscatter, Jour. Geophys. Res. **99**, 16,269-16,291,(1994)

Atlas, R., et al., Surface Wind Velocity Over the Ocean in Atlas of Satellite Observations Related to Global Change, R. J. Gurney et al. eds, Cambridge University Press, New York, (1993)

Arya, S. P., Introduction to Micrometeorology, Academic Press, (1988)

Balanis, C. A., Advanced Engineering Electromagnetics, John Wiley and Sons, New York (1989)

Banner, M. L. and I. R. Young,. Modeling Spectral Dissipation in the Evolution of Wind Waves. Part I: Assessment of Existing Model Performance, Jour. Phys. Oceanog., **24**, 1550-1571, (1994)

Banner, M., I. S. F. Jones and J. C. Trinder, Wavenumber Spectra of Short Gravity Waves, J. Fluid Mech. ,**198**, 321-344, (1989)

Banner, M. and Phillips O. M., On the Incipient Breaking of Small Scale Waves, J. Fluid Mech., **65**, 647 – 656 (1974)

Banner, M., Equilibrium Spectra of Wind Waves, Jour. Phys. Oceanog., **20**, 966-984 (1990)

Barrick, D. E., Rough Surface Scattering Based on the Specular Point Theory, IEEE Trans. Antennas Propag., **AP-16**, 449 – 454 (1968)

Bender, C. M. and S. A. Orszag, Advanced Mathematical Methods for Scientists and Engineers, Mc Graw- Hill, New York (1978)

Benoit, M., Practical Comparative Performance Survey of Methods Used for Estimating Directional Wave Spectra from Heave-Pitch-Roll Data, Coastal Engineering, 62 – 75 (1992)

Bennettt, A. F., Inverse Methods in Physical Oceanography, Cambridge University Press, (1992)

Bracalente, E. et al., The SASS Scattering Coefficient (σ^0) Algorithm, IEEE Jour. of Ocean. Engin., OE-5 , **2**, 145-154, (1980)

Bretherton, F. P., and C. J. R. Garrett, Wavetrains in Inhomogeneous Moving Media, Proc. Roy. Soc. A, **302**, 529, (1969)

Brown, G., Quasi-Specular Scattering From the Air-Sea Interface, Chapter 11 in Surface Waves and Fluxes: Volume II – Remote Sensing, (W. Plant and G. Geernaert, eds.), Kluwer Academic Publishers, Boston (1990)

Busalacchi, A. J. et al., Comparison of Sensor Microwave Imager Vector Wind Stress With Model-Derived and Subjective Products for the Tropical Pacific, Jour. Geophys. Res., 98, C4 6961-6977 (1993)

Cardone, V. J., Specification of the Wind Distribution in the Marine Boundary Layer for Wave Forecasting, Ph. D. Thesis, New York University, (1970)

Caudal, G. and D. Hauser, Directional Spreading Function of the Sea Wave Spectrum at Short Scale, Inferred from Multifrequency Radar Observations, Jour. Geophys. Res., 101, C7 , 16,601 – 16,613 (1996)

Charney, J. G. et al., Numerical Integration of the Barotropic Vorticity Equation, Tellus, 2, 237 – 257, (1950)

Charney, J. G. et al., Use of Incomplete Historical Data to Infer the Present State of the Atmosphere, J. Atmos.Sci., **26**, 1160 – 1163. (1969)

Chen, K.S., A. K. Fung and D. E. Weissman, A Backscattering Model for Ocean Surface, IEEE Trans. on Geosci. and Remote Sens., **30**, no. 4, (1992)

Chen, K.S., A. K. Fung and D. E. Weissman, A Backscattering Model for the Ocean Surface, IEEE Trans. on Geosci. and Remote Sens., **30**, no. 4, (1992)

Chi, C.-Y. and F. K. Li, A Comparative Study of Several Wind Estimation Algorithms for Spaceborne Scatterometers, IEEE Tr. Geosci. and Remote Sens., **26**, 2, 115-121 (1988)

Courtier, P. and O. Talagrand, Variational Assimilation of Meteorological Observations With the Adjoint Vorticity Equation. II: Numerical Results, Quart. Jour. of R. Met. Soc. , 113 1329-1347 (1987)

Cox, C. S., Measurements of Slopes of High-Frequency Wind Waves, J. Marine Res. **16**, 199 – 225 (1958)

Cox, C. S. and W. H. Munk, Statistics of the Sea Surface Derived from Sun Glitter. J. Marine Res. **13**, 198-227, (1954 a)

Cox, C. S. and W. H. Munk, Measurements of the Roughness of the Sea Surface from Photographs of the Sun's Glitter, Jour. Opt. Soc. Am., **44**, 838 – 50, (1954 b)

Daley, J. C., Wind Dependence of Radar Sea Return, Jour. Geophys. Res., 78, 33 7823-7833, (1973)

Daley, R., Atmospheric Data Analysis, Cambridge University Press, (1991)

Debnath, L. and P. Mikusinski, Introduction to Hilbert Spaces With Applications, Academic Press (1990)

Dobson , E., et al., Validation of Geosat Altimeter-Derived Wind Speeds and Significant Wave Heights Using Buoy Data, Jour. Geophys. Res., **92**, no. C10, 10,719-10,731, (1987)

Donelan, M. A., Air-Sea Interaction, in The Sea, 9, Ocean Engineering Science; Wiley, New York, p. 239 – 292, (1990)

Donelan, M. A., The Effect of Swell on the Growth of Wind Waves, Johns Hopkins APL Tech. Digest, 8, 1, (1987)

Donelan, M. A., J. Hamilton and W. H. Hui, Directional Spectra of Wind-Generated Waves, Phil. Trans. R. Soc. Lond. A., 315, 509-562 (1985)

Donelan, M.A. and W.J. Person, Jr. Radar Scattering and Equilibrium Ranges in Wind-Generated Waves With Application to Scatterometry, Jour. Geophys. Res., 92, C5, 4971-5029, (1987)

Donelan, M. A., W. M. Drennan and A. K. Magnusson, Nonstationary Analysis of the Directional Properties of Propagating Waves, Jour. Phys. Oceanog., **26**, No. 9, (1996)

Donelan, M. A., et al., On the Dependence of Sea Surface Roughness on Wave Development, Jour. Phys. Oceanog., **23**, 2143 - 2149 (1993)

Donelan, M. A., and W. H. Hui, Mechanics of Ocean Surface Waves, p.209 – 247, in Geernaert G.L. and W.J. Plant (eds.) Surface Waves and Fluxes, vol. I: Current Theory, Kluwer Academic Publishers (1990)

Durden, S. L. Microwave Scattering From the Ocean Surface, Ph.D. Dissertation Stanford University, (1986)

Durden, S. L. and J. F. Vesecky , A Physical Radar Cross Section Model for a Wind Driven Sea with Swell, IEEE Jour. Ocean Engin. OE-10 (4): 445 – 451, (1985)

Dyer, A, J. A Review of Flux-Profile Relationships, Boundary-Layer Meteorology, **7**, 363 – 372, (1974)

Earle, M. D., Use of Advanced Methods of Estimating Directional Wave Spectra from NDBC Pitch-Roll Buoy Data, National Data Buoy Center Report (1993)

Elfouhaily, T., et al., A Unified Directional Spectrum for Long and Short Wind-Driven Waves, Jour. Geophys. Res. **102**, C7, (1997)

Eliassen, A., Provisional Report on Calculation of Spatial Covariance and Autocorrelation of the Pressure Field, Rept. No. 5, Inst. Weather Climate Res., Academy of Science, Oslo, (1954), reprinted in Bengtsson et al., pp. 319 – 330: Dynamic Meteorology: Data Assimilation Methods, Springer-Verlag, New York, (1981)

Ewing, J. A., Wind Waves: A Review of Research During the Last Twenty-five Years, Geophys. Jour., Roy. Astr. Soc. 74, 313-329 (1983)

Feindt, F. et al., Airborne Measurements of the Ocean Radar Cross Section at 5.3 Ghz as a Function of Wind Speed, Radio Science, 21, 313-329 (1986)

Freilich, M. H. and R. S. Dunbar, A Preliminary C-Band Scatterometer Model Function for the ERS-1 AMI Instrument, Proc. First ERS-1 Symposium, Space at the Service of Our Environment (1993)

Forristall, G. Z., Measurements of a Saturated Range in Ocean Wave Spectra, J. Geophys. Res., 86, 8075 – 8084, (1981)

Fung, A. K. and K. K. Lee. A Semi-Empirical Sea-Spectrum Model for Scattering Coefficient Estimation, IEEE J. Oceanic Eng., **OE-7**, no. 4, 166 – 176, (1982)

Fung, A. K. Microwave Scattering and Emission Models and their Application. Artech House, Boston (1994)

Garrett, C. and J. Smith, On the Interaction Between Long and Short Surface Waves, J. Phys. Oceanog., 6, 925 – 930, (1976)

Geernaert G. L. and W.J. Plant (eds) Surface Waves and Fluxes, vol. I: Current Theory, Kluwer Academic Publishers (1990)

Geernaert G. L. and W.J. Plant (eds) Surface Waves and Fluxes, vol. II: Remote Sensing, Kluwer Academic Publishers (1990)

Geernaert, G., Measurement of the Angle Between the Wind Vector and Wind Stress Vector in the Surface Layer Over the North Sea, Jour. Geophys. Res., **93**, no. C7, 8215 – 8220, (1988)

Geernaert, G., et al., Directional Attributes of the Ocean Surface Wind Stress Vector, Jour. Geophys. Res., **98**, no. C9, 16,571 – 16,582, (1993)

Gelb, et al., Applied Optimal Estimation, MIT Press, Cambridge MA (1974)

Ghil, M. and P. Malanotte-Rizzoli, Data Assimilation in Meteorology and Oceanography, Advances in Geophysics, 33, 141-266, (1987)

Gill, A. E. Atmosphere-Ocean Dynamics, Academic Press, New York (1982)

Gill, P. E., W. Murray and M. H. Wright, Practical Optimization, Academic Press, New York (1981)

Glazman, R. E. et al., Scatterometer Wind Speed Bias Induced by the Large-Scale Component of the Wave field, Jour. Geophys. Res., 93, C2, 1317-1328 (1988)

Graber, H. C., N. Ebuchi and R. Vakkayil. Evaluation of ERS-1 Scatterometer Winds with Wind and Wave Ocean Buoy Observations, Report RSMAS-96-003, (1996)

Gunther, H. et al. The WAM Model Cycle 4, Technical Report No. 4, ISSN 0940-9327, (1992)

Hara, T., E. J. Bock and D. Lyzenga, In Situ Measurements of Capillary-Gravity Wave Spectra Using a Scanning Laser Slope Gauge and Microwave Radars, Jour. Geophys. Res., **99**, 12,593 – 12,602, (1994)

Hasselmann, K. On the Non-linear Energy Transfer in a Gravity Wave Spectrum. Part 1., Jour. Fluid Mech. **12**, 481 - 500. (1962)

Hasselmann, K. On the Non-linear Energy Transfer in a Gravity Wave Spectrum. Parts 2 and 3. Jour. Fluid Mech. **15**, 273 - 381; 385 - 398, (1963)

Hasselmann, K. et al. Measurements of Wind Wave Growth and Swell Decay During the Joint North Sea Wave Project (JONSWAP). Herausgegeben vom Deutch-Hydrograph. Ins., Reihe A, no. 12, (1973)

Hauser, D. et al., RESSAC: A New Airborne FM/CW Radar Ocean Wave Spectrometer, IEEE Trans. Geosci. And Remote Sens., **30**, 981 - 995

Hoffman, R.N. A Preliminary Study of the Impact of ERS-1 C-Band Scatterometer Wind Data on the European Center for Medium Range Forecasts Data Assimilation System, Jour. Geophys. Res., 98, C6, 10,223-10,244, (1993)

Huang, N. E., Wave Spectra, in The Sea, **9**, Ocean Engineering Science; Wiley, New York, p. 197 – 237, (1990)

Hwang, P. A., S. Atakturk, M. A. Sletten and D. B. Trizna, A Study of Wavenumber Spectra of Short Water Waves in the Ocean, J. Phys. Oceanog., **26**, 1266- 1285, (1996)

Hwang, P. A., D. B. Trizna and J. Wu, Spatial Measurements of Short Wind Waves Using a Scanning Slope Sensor, Dyn. Atmos. Oceans, **20**, 1 – 23, (1996)

Jahne, B. and K. S. Riemer, Two-Dimensional Wave Number Spectra of Small-Scale Water Surface Waves, Jour. Geophys. Res., **95**, 11531 – 11546, (1990)

Jansen, R. , Radar Model, NRL Memorandum NRL-93-7234-01, (1993)

Janssen, P. A. E. M. and G. J. Komen, Effect of Atmospheric Stability on the Growth of Surface Gravity Waves, Boundary Layer Meteorology, **32**, 85-96, (1985)

Janssen, P. A. E. M., et al., VIERS-1 Scatterometer Model, Jour. Geophys. Res., **103**, no. C4, 7807 – 7831, (1998)

Jensen, G. A., A Peaked-Wave Model of Microwave Radar Scattering from the Ocean Surface, Ph.D. Dissertation, Stanford University (1997)

Jones, W. L. and L. C. Schroeder. Radar Backscatter from the Ocean: Dependence on Surface Friction Velocity, Boundary-Layer Meteorology, **13**, 133 – 149, (1978)

Juszko, B. – A., R. F. Marsden and S. R. Waddell, Wind Stress from Wave Slopes Using Phillips Equilibrium Theory, Jour. Phys. Oceanog., **25**, 185 – 203, (1995)

Kahma, K. K. A Study of the Growth of the Wave Spectrum With Fetch, J. Phys. Oceanog. **11**, 1503-1515 (1981)

Kawai, S., K. Okuda and Y. Toba, Field Data Support of Three-seconds power low and $gu^*\sigma^{-4}$ Spectral Form for Growing Wind Waves, J. Oceanogr. Soc. Japan, **33**, 137 – 150 (1977)

Keller W. C. et al. Dependence of X Band Microwave Sea Return on Atmospheric Stability and Sea State, Jour. Geophys. Res., 90, C1, 1019-1029, (1985)

Khandekar M. L., Operational Analysis and Prediction of Ocean Wind Waves, v. 33 in Coastal and Estuarine Studies, Springer-Verlag, New York (1989)

Kinsman, B. Wind Waves Their Generation and Propagation on the Ocean Surface, Prentice Hall (1965)

Kitaigorodskii, S. A. On the Theory of the Equilibrium Range in the Spectrum of Wind-Generated Gravity Waves, J. Phys. Oceanogr., 13, 816-827 (1983)

Kitaigorodskii, S. A., V. P. Krasitskii, and M. M. Zaslavskii, On Phillips' Theory of Equilibrium Range in the Spectra of Wind-Generated Gravity Waves, J. Phys. Oceanogr. **5**, 410 - 420.(1975)

Klinke, J. and B. Jahne, 2D Wave Number Spectra of Short Wind Waves – Results from Wind Wave Facilities and Extrapolation to the Ocean, SPIE Proc., 1749, 1-13 (1992)

Kodis, R. D., A Note on the Theory of Scattering from an Irregular Surface, IEEE Trans. Antennas and Propagation, **AP-14**, 77 – 82, (1966)

Komen, G. J., K. Hasselmann and S. Hasselmann, On the Existence of a Fully Developed Wind-Sea Spectrum, J. Phys. Oceanogr., 14, 1271 – 1285, (1984)

Komen et al., Dynamics and Modeling of Ocean Waves, Cambridge University Press, New York (1994)

Kondo, J. Fujinawa, Y. and G. Naito, Wave Induced Wind Fluctuations Over the Sea, J. Fluid Mech., 51, 751 – 771, (1972)

Large, W.G. and S. Pond, Open Ocean Momentum Flux Measurements in Moderate to Strong Winds, Jour. Phys. Oceanog., 11, 324-336 (1981)

Lawson, L. M. and R. B. Long, Multimodal Properties of the Surface Wave Field Observed with Pitch-Roll Buoys During GATE, J. Phys. Oceanog., **13**, 474 – 486, (1983)

LeBlond, P.H. and L.A. Mysak, Waves in the Ocean, Elsevier, Amsterdam (1978)

Lettvin, E. J.F. Vesecky and D.R. Lyzenga, An Investigation of the Effects of Atmospheric Stability on Radar Cross Section Prediction, Presentation IGARSS (1995)

Lettvin, E. J.F. Vesecky, An Ocean Spectral Model for Scatterometer Wind Retrieval, Presentation IGARSS (1997)

Li, F. et al., Ocean Radar Backscatter Relationship with Near-Surface Winds: A Case Study During FASINEX, Jour. Phys. Oceanog., **19**, 342-353 (1989)

Liu, P. C. and D. J. Schwab, A Comparison of Methods for Estimating u* From Given U_z and Air-Sea Temperature Differences, Jour. Geophys. Res., **92**, C6 6488-6494, (1987)

Liu, Y. and W. J. Pierson Jr. Comparisons of Scatterometer Models for the AMI on ERS-1: The Possibility of Systematic Azimuth Angle Biases of Wind Speed and Direction, IEEE Tr. Geosci. and Remote Sens., 32, 3, 626-635 (1994)

Long, D. Identifiability in Wind Estimates from Scatterometer Measurements, IEEE Tr. Geosci. and Remote Sens., **29**, no. 2, 268-276, (1991)

Longuet-Higgins, M. S., D. E. Cartwright and N. D. Smith, Observations of the Directional Spectrum of Sea Waves Using the Motions of a Floating Buoy, Ocean Wave Spectra, Prentice-Hall, New York, p. 111 – 136, (1963)

Ludwig, F.L. et al. Use of Mass Conservation and Critical Dividing Streamline Concepts for Efficient Objective Analysis of Winds in Complex Terrain, Jour. Appl. Meteorol., 30, 11, 1490-1499, (1991)

Lynch, P., Deducing the Wind from Vorticity and Divergence, Mon. Weather Rev., 116, 86-93 (1988)

Lyzenga, D.R. Radar Imaging of Sub-Mesocscale Ocean Phenomena, ERIM Report 225300-8-F, (1993)

Lyzenga, D.R. Interaction of Short Surface and Electromagnetic Waves With Ocean Front, Jour. Geophys. Res., 96, C6, 10,765-10,772 (1991)

Lyzenga, D.R. and J. Bennett. Full-spectrum Modeling of Synthetic Aperture Radar Internal Wave Signatures, J. Geophys. Res., **93**, 12345 – 12354 (1988)

Maat, N., W. Oost and Kraan. The Roughness of Wind Waves, Boundary-Layer Meteorology, **54**, 89-103 (1991)

Menke, W. Geophysical Data Analysis: Discrete Inverse Theory, Academic Press (1989)

Mitzner, K. M., Effect of Small Irregularities on Electromagnetic Scattering from an Interface of Arbitrary Shape, Jour. Math. Physics, **5**, no. 12, 1776 – 1786, (1964)

Monaldo, F., Expected Differences Between Buoy and Radar Altimeter Estimates of Wind Speed and Significant Wave Height and Their Implications on Buoy-Altimeter Comparisons, Jour. Geophys. Res., **93**, no. C3, 2285 – 2302, (1988)

Moore, A.M. Data Assimilation in a Quasi-Geostrophic Open-Ocean Model of the Gulf Stream region Using the Adjoint Method, Jour. Phys. Oceanog. **21**, 398-427 (1991)

Moore, R.K. and W.J. Pierson, Jr. Measuring Sea State and Estimating Surface Winds from a Polar Orbiting Satellite, in 'Electromagnetic Sensing of the Earth from Satellites', (R. Zirkland, ed.), R1-R28 Polytechnic Press, Brooklyn N.Y. (1967)

Nayfeh, A. H., Introduction to Perturbation Techniques, Wiley, New York (1993)

Nelson, C. V., Wave Data Summary Standard Leopard I, Oct. 1990, Report STD – N- 727, The Johns Hopkins University Applied Physics Laboratory, (1990)

Oltman-Shay, J. and R. T. Guza, A Data-Adaptive Ocean Wave Directional-Spectrum Estimator for Pitch-Roll Type Measurements, Jour. Phys. Oceanog., **14**, 1800 – 1810, (1984)

Panofsky, H., Objective Weather Map Analysis, J. Meteorol., **6**, 386 – 392 (1949)

Papoulis, A. Probability, Random Variables, and Stochastic Processes, Mc-Graw Hill, New York, (1984)

Paulson, C. A., The Mathematical Representation of Wind Speed and Temperature Profiles in the Unstable Atmospheric Boundary Layer, J. Appl. Meteor., 9, 857 – 861, (1970)

Perrie, W. and L. Wang. A Coupling Mechanism for Wind and Waves, Jour. Phys. Oceanog. **24**, 615-630 (1995)

Phillips, O. M., The Equilibrium Range in the Spectrum of Wind-Generated Gravity Waves, J. Fluid Mech., **4**, 426 – 434, (1958)

Phillips, O. M., The Dynamics of the Upper Ocean, Cambridge University Press, Cambridge, England (1977)

Phillips, O.M., The Dispersion of Short Wavelets in the Presence of a Dominant Long Wave, Jour. Fluid Mech., **7**, 465 - 485 (1981)

Phillips, O. M., Spectral and Statistical Properties of the Equilibrium Range in Wind-Generated Gravity Waves, Jour. Fluid Mech., **156**, 505 - 531, (1985)

Phillips, O. M. Remote Sensing of the Sea Surface, Ann. Rev. Fluid Mech., **20**, 89 - 198 (1988)

Pierson, W. J., Jr., Dependence of Radar Backscatter on Environmental Parameters, in Geernaert G. L. and W.J. Plant (eds.) Surface Waves and Fluxes, vol. II: Remote Sensing, Kluwer Academic Publishers (1990)

Pierson, W. J., Jr. Measurements of the Synoptic Scale Wind Over the Ocean, Jour. Geophys. Res. 88, C3, 1683 - 1708 (1983)

Pierson, W.J., Jr. Probabilities and Statistics for Backscatter Estimates Obtained by a Scatterometer With Applications to New Scatterometer Design Data, NASA Contractor Report 4228 (1989)

Pierson, W.J., Jr. and L. Moskowitz, A Proposed Spectral Form for Fully Developed Seas Based on the Similarity Theory of S.A. Kitaigorodskii, Jour. Geophys. Res., 69, no. 24, 5181 – 5190, (1964)

Plant, W., Bragg Scattering of Electromagnetic Waves from the Air/Sea Interface, Chapter 11 in Surface Waves and Fluxes: Volume II – Remote Sensing, (W. Plant and G. Geernaert, eds.), Kluwer Academic Publishers, Boston (1990)

Plant, W. J., A Relationship Between Wind Stress and Wave Slope, Jour. Geophys. Res. **87**, C3, 1961 - 1967 (1982)

Plant, W. J., A Two-Scale Model of Short Wind-Generated Waves and Scatterometry, Jour. Geophys. Res. **91**, C9, 10,735 - 10,749 (1986)

Plant, W. J. and J. W. Wright, Growth and Equilibrium of Short Gravity Waves in a Wind-Wave Tank, Jour. Fluid Mech., **82**, 767, (1977)

Reece, A. M., Jr., Modulation of Short Waves by Long Waves, Boundary-Layer Meteorology, **13**, 204-213 (1978)

Reider, K. F., J. A. Smith and R. A. Weller, Observed Directional Characteristics of the Wind, Wind Stress and Surface Waves on the Open Ocean, Jour. Geophys. Res., **99**, no. C11, 22,589 – 22,596, (1994)

Renders, J.-M. et al., A Comparative Study of Optimization Methods for the Retrieval of Quantitative Information from Satellite Data, Commission of the European Communities Joint Research Center Publication, EUR 14851, EN (1992)

Resio, D. and W. Perrie. A Numerical Study of Nonlinear Energy Fluxes due to Wave-Wave Interactions, Jour. Fluid Mech., **223**, 603 - 629 (1991)

Rice, S. O., Reflection of Electromagnetic Waves from Slightly Rough Surfaces, Comm. Pure Appl. Math. **4**, 351 - 378 (1951)

Robinson, I. S., Satellite Oceanography, Ellis Horwood, Chichester, West Sussex, England (1985)

Romeiser, R., W. Alpers, V. Wismann, An Improved Composite Surface Model for the Radar Backscattering Cross Section of the Ocean Surface 1. Theory of the Model and Optimization/Validation by Scatterometer Data, Jour. Geophys. Res., **102**, no. C11, 25,237 – 25,250, (1997)

Rufenach, C. L., J. J. Bates and S. Tosini, ERS-1 Scatterometer Measurements – Part I: The Relationship Between Radar Cross Section and Buoy Wind in Two Oceanic Regions, IEEE Tr. Geosci. And Rem. Sens., **36**, no. 2, (1998)

Sasaki, Y. Some Basic Formalisms in Numerical Variational Analysis, Mon. Weather Review, **98**, 875 - 883 (1970)

Sasaki, Y. An Objective Analysis Based on the Variational Method, J. Meteor. Soc. Japan, **36**, 875 - 883 (1958)

Sashegyi K. D., and R. V. Madala, Initial Conditions and Boundary Conditions, Ch. I in: Mesoscale Modeling of the Atmosphere (eds. Pielke, R.A., and R.P. Pearce), Meteorological Monographs **25**, 47 (1994)

Shemdin, O. H., M. Tran and S. C. Wu, Directional Measurement of Short Ocean Waves With Stereophotography, Jour. Geophys. Res., **93**, 13,891 – 13,901, (1988)

Shumway, R. H., Applied Statistical Time Series Analysis, Prentice Hall, Englewood Cliffs, N. J., (1988)

Smith, S. D., Wind Stress and Heat Flux Over the Ocean in Gale Force Winds, J. Phys. Oceanogr., **10**, 709 – 726, (1980)

Snyder R.L. et al. Array Measurements of Atmospheric Pressure Fluctuations Above Surface Gravity Waves, Jour. Fluid Mech. **102**, 1 - 59 (1981)

Stoffelen, A. and D.L.T. Anderson, ERS-1 Scatterometer Data Characteristics and Wind Retrieval Skill, Proc. First ERS-1 Symposium, Space at the Service of Our Environment, (1993)

Stratton, J. A., Electromagnetic Theory, McGraw Hill, New York, (1941)

Thacker, W. C., Fitting Data to Models by Enforcing Spatial and Temporal Smoothness, J. Geophys. Res., **93**, 10,655 – 10,665, (1988)

Ulaby, F. T., R. K. Moore and A. K. Fung, Microwave Remote Sensing Active and Passive: Volume I. Microwave Remote Sensing Fundamentals and Radiometry, Artech House (1981)

Valenzuela, G. R. Theories for the Interaction of Electromagnetic and Ocean Waves - A Review, Boundary-Layer Meteorology, **13**, 61 - 85 (1978)

Valenzuela, G. R. and M. B. Laing, Non-linear Energy Transfer in Gravity-Capillary Wave Spectra with Applications, Jour. Fluid Mech., **54**, 507 – 520, (1972)

Wang, H. T. and C. B. Friese, Error Analysis of the Directional Wave Spectra Obtained by the NDBC 3-m Pitch-Roll Discus Buoy, IEEE Jour. Ocean Engin, **22**, no. 4, 639 – 648, (1997)

Wentz, F. J., Measurement of the Oceanic Wind Vector Using Satellite Microwave Radiometers, RSS Technical Report 051591, (1991)

Wentz, F. J., and L. A. Mattox, New Algorithms for Microwave Measurements of Ocean Winds: Applications to Seasat and the Special Sensor Microwave Imager, Jour. Geophys. Res., **91**, no. C2, 2289 – 2307, (1986)

Whitham, G. E., Linear and Non-linear Waves, Wiley, New York, (1974)

Wilheit, T. T. and M. G. Fowler, Microwave Radiometric Determination of Wind Speed at the Surface of the Ocean During BESEX, IEEE Trans. Ant. And Prop., 111 – 120, (1977)

Woiceshyn, P. M., et al., The Necessity for a New Parameterization of an Empirical Model for Wind/Ocean Scatterometry, Jour. Geophys. Res., **91**, 2273 – 2288, (1986)

Wright, J. W., A New Model for Sea Clutter, IEEE Trans. Ant. And Prop., AP-16, 217 – 223, (1968)

Wu, J., Wind-Induced Drift Currents, J. Fluid Mech., **68**, Part 1 49 – 70, (1975)

Wu, J., Laboratory Studies of Wind-Wave Interactions, Jour. Fluid Mech., **34**, 91 – 111, (1968)

Wunsch, C., The Ocean Circulation Inverse Problem, Cambridge Univ. Press, New York, (1996)

Yu, L. and J.J. O'Brien, Variational Estimation of the Wind Stress Drag Coefficient and the Oceanic Eddy Viscosity Profile. Jour. Phys. Oceanog., **21**, 709 – 719 (1991)

IMAGE EVALUATION
TEST TARGET (QA-3)

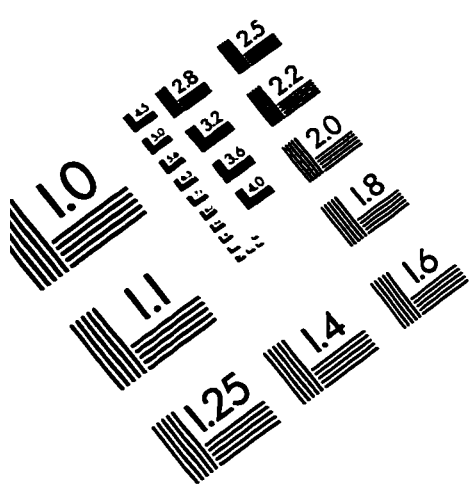

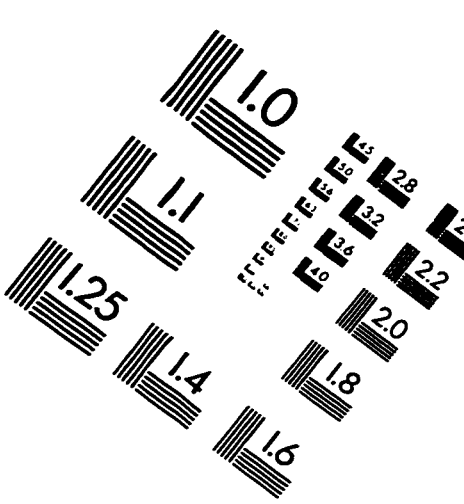

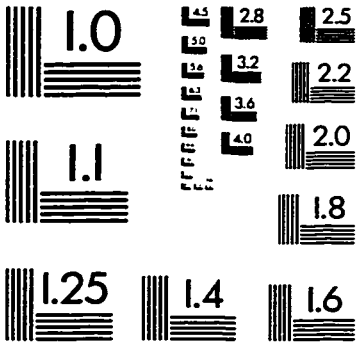

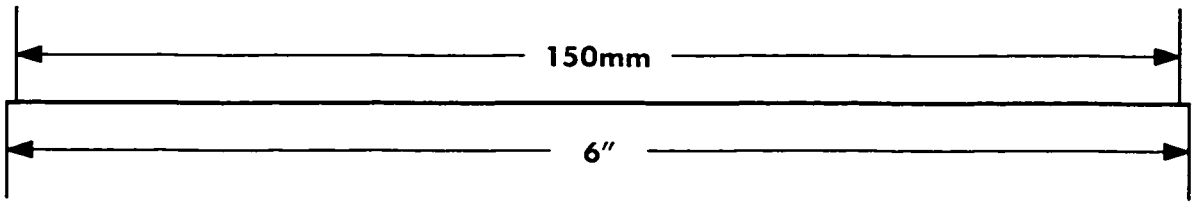

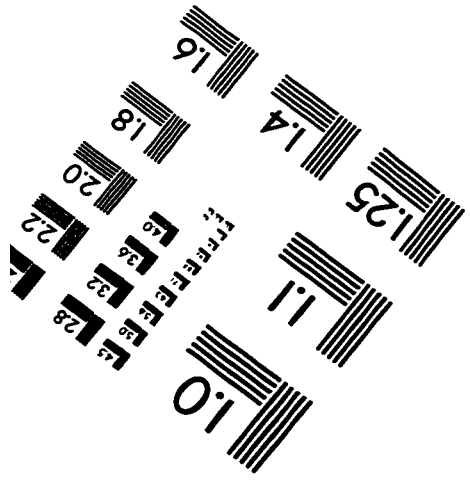

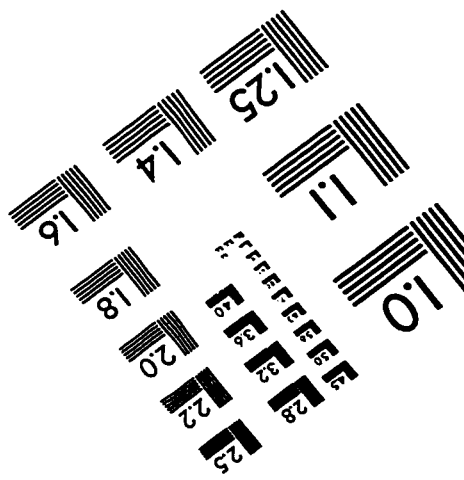

APPLIED IMAGE, Inc
1653 East Main Street
Rochester, NY 14609 USA
Phone: 716/482-0300
Fax: 716/288-5989